

# TOUCH-SPINNING OF NANOFIBERS FOR NERVE REGENERATION

by

DARYA ASHEGHALI

(Under the Direction of Sergiy Minko)

## ABSTRACT

Touchspinning is a simple and scalable method which does not depend on the dielectric properties of polymer solutions and it has shown advantages over the common fiber spinning techniques, such as electrospinning and microfluidic spinning. Touchspinning setup is used for drawing nano- and microfibers from polymer solutions or melts using a rotating rod or a set of rods. In this study, the aligned touchspun polycaprolactone (PCL) nanofibers were fabricated at different spinning rates and the proliferation potential of the neural stem cells (NSCs) was analyzed on these nanofibrous scaffolds. The aligned electrospun PCL nanofibers were fabricated at spinning rates similar to the touchspun nanofibers and they were served as a control group. The Young's modulus values of the touchspun fibers at various spinning rates were much higher than those of electrospun fibers. Also, the structural characteristics of the PCL nanofibers were analyzed by X-ray diffraction (XRD). The degree of crystallinity of the touchspun fibers was greater than that of electrospun fibers at various spinning rates. The NSC cells exhibited an elongated neurite growth along the touchspun PCL nanofibers with varying spinning rates. Whereas, the NSC cells tend to aggregate on the entangled electrospun PCL nanofibers and they did not spread along the fibers. As the spinning rate of the touchspun nanofibers increased, the percentage of TUJ1 positive cells and the percentage of GFAP positive neurons increased. These results have shown the

feasibility of using the touchspinning technique to fabricate fibrous scaffolds for neural tissue engineering applications.

INDEX WORDS: Nerve regeneration, Nanofibers, Neural stem cells, Touchspinning, Electrospinning

TOUCHSPINNING OF NANOFIBERS FOR NERVE REGENERATION

by

DARYA ASHEGHALI

BSc, University of Tehran, Iran, 2010

A Dissertation Submitted to the Graduate Faculty of The University of Georgia in Partial  
Fulfillment of the Requirements for the Degree

DOCTOR OF PHILOSOPHY

ATHENS, GEORGIA

2018

© 2018

Darya Asheghali

All Rights Reserved

TOUCHSPINNING OF NANOFIBERS FOR NERVE REGENERATION

by

DARYA ASHEGHALI

Major Professor:     Sergiy Minko  
Committee:            Tina T. Salguero  
                              Jin Xie

Electronic Version Approved:

Suzanne Barbour  
Dean of the Graduate School  
The University of Georgia  
August 2018

DEDICATION

*To God*

*and*

*To my parents, Mahasti Sepahzad and Hassan Asheghali*

## ACKNOWLEDGEMENTS

I am grateful that God gave me this wonderful opportunity to pursue my graduate studies at the University of Georgia in the United States of America. I am deeply grateful to my parents, brother, uncle, and grandmother for their support and unconditional love. I would also like to express my appreciation to my major advisor, Dr. Sergiy Minko for his mentorship and assistance, and my committee members Dr. Tina T. Salguero and Dr. Jin Xie for their time and valuable feedback on my projects. I also thank American Chemical Society for permission to include Chapter 5 of my dissertation, which was originally published in Journal of American Chemical Society.

This work would not have been possible without the help of my collaborators, Se-Jun Lee and Dr. Lijie G. Grace from the George Washington University, Dr. Ian M. Griffiths from the University of Oxford, Dr. Andreas Furchner and Dr. Karsten Hinrichs from Leibniz-Institut für Analytische Wissenschaften–ISAS–e.V., Dr. Alexander Tokarev and Dr. Nataraja S. Yadavalli and Alexey Gruzd from the Nanostructured Materials Laboratory at The University of Georgia, Steve Larson and Hoang M. Luong and Dr. Tho Nguyen from Department of Physics and Astronomy at the University of Georgia, Bryan Weizhong Zhang from Department of Chemistry at the University of Georgia, Dr. Howard A. Stone from Princeton University, and Tom Fitzsimons and Justin Fitzsimons from Whiff LLC.

I owe a great debt of gratitude to my amazing friends, Kay Faust Tatum and Mary Hamann, for their continued support.

## TABLE OF CONTENTS

	Page
ACKNOWLEDGEMENTS .....	v
LIST OF TABLES .....	ix
LIST OF FIGURES .....	x
CHAPTER	
1 INTRODUCTION AND LITERATURE REVIEW .....	1
2 TOUCH-SPINNING OF NANOFIBERS FOR NERVE REGENERATION.....	22
2.1 Abstract .....	23
2.2 Introduction.....	24
2.3 Experimental Section .....	26
2.4 Results.....	30
2.5 Discussion .....	34
2.6 Conclusion .....	39
2.7 Acknowledgements.....	40
3 ENHANCED ALIGNMENT OF THE NEURAL STEM CELLS ON THE TOUCH- SPUN NANOFIBROUS SCAFFOLDS .....	55
3.1 Abstract .....	56
3.2 Introduction.....	57
3.3 Experimental Section .....	59
3.4 Results.....	63

3.5 Discussion .....	68
3.6 Conclusion .....	71
3.7 Acknowledgements.....	71
4 GRAVITATIONAL DRY-SPINNING OF ULTRALONG MICRO- AND NANOFIBERS .....	87
4.1 Abstract.....	88
4.2 Introduction.....	89
4.3 Experimental Section.....	96
4.4 Results and Discussion .....	98
4.5 Applications of the Gravitational Dry-Spun Ultralong Micro and Nanofibers ...	100
4.6 Conclusion .....	102
4.7 Acknowledgements.....	103
5 CONVERSION OF METALLIC SINGLE-WALLED CARBON NANOTUBE NETWORKS TO SEMICONDUCTING THROUGH ELECTROCHEMICAL ORNAMENTATION .....	124
5.1 Abstract.....	125
5.2 Introduction.....	126
5.3 Experimental Details.....	133
5.4 Results and Discussion .....	136
5.5 Conclusions.....	150
5.6 Acknowledgements.....	151
6 CONCLUSIONS AND FUTURE WORK.....	160
6.1 Conclusions .....	160

6.2 Future Work .....	162
REFERENCES .....	163

## LIST OF TABLES

	Page
Table 2.1: %Crystallinity from XRD spectra of the nanofibers fabricated by touchspinning or electrospinning at 1400 RPM.....	43
Table 2.2: % Crystallinity from DSC spectra of the nanofibers fabricated by touchspinning or electrospinning at varying rotation speeds of the collector .....	44
Table 3.1: Average diameter of nanofibers fabricated by touchspinning or electrospinning with the collector at varying rotation speeds .....	74
Table 3.2: Young’s modulus of the nanofibers fabricated by touchspinning or electrospinning at varying rotation speeds of the collector.....	77
Table 3.3: Percent (%) Crystallinity from XRD spectra of the nanofibers fabricated by touchspinning or electrospinning at varying rotation speeds of the collector .....	78
Table 3.4: Percent (%) Crystallinity from DSC spectra of the nanofibers fabricated by touchspinning or electrospinning at varying rotation speeds of the collector.....	79
Table 4.1: Vapor pressure, viscosity, and surface tension for the solvents used.....	113
Table 4.2: Properties of PEO solution in various solvents at 20 °C.....	118
Table 4.3: Properties of TritonX-100 in PEO solution at 20 °C.....	119

## LIST OF FIGURES

	Page
Figure 1.1: Effects of the Diameter on the Mechanical Properties of the Fibers.....	15
Figure 1.2: Electrospinning.....	16
Figure 1.3: Forcespinning <sup>TM</sup> .....	17
Figure 1.4: Melt-Blowing .....	18
Figure 1.5: Direct Drawing of the Nanofibers using a Micropipette .....	19
Figure 1.6: Touchspinning.....	20
Figure 1.7: f) SEM image of PEO nanofibers. g) SEM image of Teflon nanofibers. h) TEM image of a core-shell PVA-PCL nanofiber.....	21
Figure 2.1: SEM images of aligned PCL nanofibers prepared by (A) electrospinning and by (B) touchspinning .....	41
Figure 2.2: XRD pattern describing the crystallinity of PCL fibers prepared by touchspinning and electrospinning.....	42
Figure 2.3: (A and B) Stress-strain curve of electrospun and touchspun PCL nanofibers, respectively. (C) young's modulus values for PCL nanofibers. Data are mean $\pm$ standard error of the mean. n=4; **p<0.01 when compared to electrospun fibers .....	45
Figure 2.4: Contact angle of PCL film when compared to glass. Data are mean $\pm$ standard error of the mean; N=4.....	46
Figure 2.5: Neural stem cell adhesion on various substrates after 4 hours of culture. Data are mean $\pm$ standard error of the mean; N=9, *p<0.05 when compared to glass. ....	47

Figure 2.6: Enhanced neural stem cell proliferation on glass (**a, f, k**), electrospun fibers (**b, g, l**), electrospun fibers with BSA (**c, h, m**), touchspun fibers (**d, i, n**), touchspun fibers with BSA (**e, j, o**) after 7 days of culture. Data are mean  $\pm$  standard error of the mean, N=9; \* $p < 0.05$  when compared to glass at day 1, \*\*\* $p < 0.001$  when compared to glass at day 7 .....48

Figure 2.7: Immunocytochemical staining of TUJ1 (red) and DAPI (blue) on: (**A: a, f, k**) glass, (**A: b, g, l**) electrospun fibers, (**A: c, h, m**) electrospun fibers with BSA, (**A: d, i, n**) touchspun fibers and (**A: e, j, o**) touchspun fibers with BSA after 4 days. Relative TUJ1 expression levels on: (**B-a**) glass, (**B-b**) electrospun fibers, (**B-c**) electrospun fibers with BSA, (**B-d**) touchspun fibers and (**B-e**) touchspun fibers with BSA after 4 days were determined by ImageJ software. Quantification of percentage of TUJ-1 cells on: (**C-a**) glass, (**C-b**) electrospun fibers, (**C-c**) electrospun fibers with BSA, (**C-d**) touchspun fibers and (**C-e**) touchspun fibers with BSA at day 4. Data are mean  $\pm$  standard error of the mean, N=6; \*\* $p < 0.01$  when compared to glass. Scale bar = 200  $\mu\text{m}$ .....49

Figure 2.8: Immunocytochemical staining of TUJ1 (red) and DAPI (blue) on (**A: a, f, k**) glass, (**A: b, g, l**) electrospun fibers, (**A: c, h, m**) electrospun fibers with BSA, (**A: d, i, n**) touchspun fibers and (**A: e, j, o**) touchspun fibers with BSA after 8 days. Relative TUJ1 expression levels on: (**B-a**) glass, (**B-b**) electrospun fibers, (**B-c**) electrospun fibers with BSA, (**B-d**) touchspun fibers and (**B-e**) touchspun fibers with BSA after 8 days were determined by ImageJ software. Quantification of percentage of TUJ1 cells on: (**C-a**) glass, (**C-b**) electrospun fibers, (**C-c**) electrospun fibers with BSA, (**C-d**) touchspun fibers and (**C-e**) touchspun fibers with BSA at day 8. Data are mean  $\pm$  standard error of the mean, N=6; \* $p < 0.05$ . Scale bar = 200  $\mu\text{m}$ .....51

Figure 2.9: Confocal micrographs of **(A)** NSC growth and spreading on PCL nanofibers. Cells were stained with TUJ1 (red) as shown on **(A-a)** for electrospun fibers and **(A-b)** for touchspun fibers. The associated neurite outgrowth was traced automatically by NeuriteTracer Plug-in as shown on **(A-c)** for electrospun fibers and **(A-d)** for touchspun fibers. The neurite angle distribution on the corresponding electrospun PCL fibers **(B)** and touchspun fibers **(C)**. The angles between electrospun fibers and neurites have been shown on: **(B: a, b, c, d, e)** for angles of  $<5^\circ$ ,  $5^\circ\sim 30^\circ$ ,  $30^\circ\sim 55^\circ$ ,  $55^\circ\sim 80^\circ$ ,  $>80^\circ$ . Also, the angles between touchspun fibers and neurites have been shown on: **(C: a, b, c, d, e)** for angles of  $<5^\circ$ ,  $5^\circ\sim 30^\circ$ ,  $30^\circ\sim 55^\circ$ ,  $55^\circ\sim 80^\circ$ ,  $>80^\circ$ . N=6.....73

Figure 3.1: SEM images of nanofibers fabricated by touchspinning or electrospinning with the collector at varying rotation speeds: **(a)** electrospun fibers at 500 RPM with the diameter of  $547\pm 87$  nm, **(b)** electrospun fibers at 1400 RPM with the diameter of  $481\pm 80$  nm, **(c)** electrospun fibers at 2000 RPM with the diameter of  $441\pm 63$  nm, **(d)** touchspun fibers at 500 RPM with the diameter of  $516\pm 72$  nm, **(e)** touchspun fibers at 1400 RPM with the diameter of  $453\pm 31$  nm, **(f)** touchspun fibers at 2000 RPM with the diameter of  $410\pm 53$  nm.....73

Figure 3.2: Elastic modulus of PCL nanofibers at varying collector speeds: **(a)** electrospun fiber at 500 RPM, **(b)** touchspun fiber at 500 RPM, **(c)** electrospun fiber at 1400 RPM, **(d)** touchspun fiber at 1400 RPM, **(e)** electrospun fiber at 2000 RPM, **(f)** touchspun fiber at 2000 RPM. N=3, \* $p<0.05$  and \*\* $p<0.01$  when compared to the corresponding group...75

Figure 3.3: Elastic stress-strain behavior of both electrospun and touchspun fibers at different collector speeds: **(a)** electrospun fibers at 500 RPM, **(b)** electrospun fibers at 1400 RPM,

(c) electrospun fibers at 2000 RPM, (d) touchspun fibers at 500 RPM, (e) touchspun fibers at 1400 RPM, (f) touchspun fibers at 2000 RPM. ....76

Figure 3.4: immunocytochemical staining of TUJ-1 (red), GFP (green) and DAPI (blue) on: (A: a, e, i and B: a, e, i) glass, (A: b, f, j) electrospun fibers at 500 RPM, (B: b, f, j) touchspun fibers at 500 RPM, (A: c, g, k) electrospun fibers at 1400 RPM, (B: c, g, k) touchspun fibers at 1400 RPM, (A: d, h, l) electrospun fibers at 2000 RPM, (B: d, h, l) touchspun fibers at 2000 RPM on day 7, respectively. Scale bar equal to 200  $\mu$ m.....80

Figure 3.5: immunocytochemical staining of TUJ-1 (green), GFAP (red) and DAPI (blue) on: (A: a, e, i and B: a, e, i) glass, (A: b, f, j) electrospun fibers at 500 RPM, (B: b, f, j) touchspun fibers at 500 RPM, (A: c, g, k) electrospun fibers at 1400 RPM, (B: c, g, k) touchspun fibers at 1400 RPM, (A: d, h, l) electrospun fibers at 2000 RPM, (B: d, h, l) touchspun fibers at 2000 RPM after 1 week of swelling (day 14). (C and D) relative expression level of (C) TUJ-1 and (D) GFAP in various substrates were determined by ImageJ software. E and T stands for electrospun fibers and touchspun fibers, respectively. (E and F) Quantification of changes in expression of TUJ-1/GFAP ratio with changes in RPM in (E) electrospun fibers and (F) touchspun fibers. Data are mean  $\pm$  standard error of the mean, n=6; \*p<0.05 and \*\*p<0.01. Scale bar equals to 200  $\mu$ m. ....82

Figure 3.6: Representative confocal microscopy images of TUJ-1 (green), GFAP (red) and DAPI (blue) of neural stem cells cultured on: (A: a, d, g) electrospun fibers at 500 RPM, (A: b, e, h) electrospun fibers at 1400 RPM, (A: c, f, i) electrospun fibers at 2000 RPM, and (B: a, d, g) touchspun fibers at 500 RPM, (B: b, e, h) touchspun fibers at 1400 RPM, (B: c, f, i) touchspun fibers at 1400 RPM, touchspun fibers with varying RPM after 2 weeks of swelling (day 14), respectively. Scale bar equal to 200  $\mu$ m. ....84

Figure 3.7: Ellipsometric phase-difference spectra of **(A)** touchspun and **(B)** electrospun PCL fibers measured in dry state (green) and in H<sub>2</sub>O (black to blue) over the course of 13 (14) days. The insets **(A-a)** and **(B-a)** show changes in  $\nu(\text{C}=\text{O})$  band shape and amplitude with time for touchspun fibers and electrospun fibers, respectively.....85

Figure 3.8: Swelling behavior of touchspun PCL fibers in water, as qualitatively monitored via the ellipsometric phase-difference at  $1500\text{ cm}^{-1}$ . The red line is to guide the eye. ....86

Figure 4.1: The gravity-spinning set-up. A droplet falls from a syringe at a velocity  $\hat{\omega}_1(\hat{t})$  striking the stage a distance  $\hat{H}$  below .....104

Figure 4.2: The schematic diagram of the gravity-spinning experiment. The droplet falls at speed drawing out a fiber with cross-sectional radius and fluid velocity. The radius of the droplet remains constant as the droplet falls. ....105

Figure 4.3: Comparison of theoretical prediction for the variation of fibre radius  $R$  with distance from the stage (solid curve) with experimental data (crosses) for the parameter values  $\alpha = 0$ ,  $\gamma = 0$ ,  $g = 0.9$ , and  $G = 1$ . (a) Experimental data; (b) Mathematical modeling.....106

Figure 4.4: Variation of dimensionless fiber radius  $R$  (scaled with radius at the droplet) with dimensionless distance from the stage  $1 - z$  (scaled with total stage height) as we vary the evaporation strength  $\alpha = 0, 0.1, 0.2, 0.3, 0.4$ . Other parameters are  $\gamma = 1$ ,  $g = 1$ , and  $G = 1$ . (a) Experimental data; (b) Mathematical modeling.....107

Figure 4.5: (a) Variation of dimensionless fiber radius  $R$  (scaled with radius at the droplet) with dimensionless distance from the stage  $1 - z$  (scaled with total stage height) as we vary the surface tension  $\gamma = 0, 1, 2, 3, 4$ . Other parameters are  $\alpha = 0.1$ ,  $g = 1$ ,  $G = 1$ . (b) Comparison

with experiment showing the same qualitative agreement. (a) Experimental data; (b) Mathematical modeling. (a) Experimental data; (b) Mathematical modeling.....108

Figure 4.6: Variation of dimensionless fiber radius  $R$  (scaled with radius at the droplet) with dimensionless distance from the stage  $1-z$  (scaled with total stage height) as we vary the gravitational force on the fluid  $g = 0, 1, 2, 3, 4$ . Other parameters are  $\alpha = 0.1$ ,  $\gamma = 1$ , and  $G = 1$ .....110

Figure 4.7: Variation of dimensionless fiber radius  $R$  (scaled with radius at the droplet) with dimensionless distance from the stage  $1-z$  (scaled with total stage height) as we vary the force on the droplet  $G = 0, 0.3, 0.6, 0.9, 1.2$ . Other parameters are  $\alpha = 0.1$ ,  $\gamma = 1$ , and  $g = 1$ .....111

Figure 4.8: Variation of dimensionless fiber radius  $R$  (scaled with radius at the droplet) with dimensionless distance from the stage  $1-z$  (scaled with total stage height) determined experimentally for different solvents. Note that both evaporation rate and surface tension vary so we need a master plot to predict the variation.....112

Figure 4.9: Variation of dimensionless fiber radius  $R$  (scaled with radius at the droplet) with dimensionless distance from the stage  $1-z$  (scaled with total stage height) for  $\alpha = 0.1$  and  $\gamma = 10$  (blue);  $\alpha = 0.15$  and  $\gamma = 10$  (red) and  $\alpha = 0.1$  and  $\gamma = 5$  (yellow). The graph illustrates that, by reducing the surface tension we can create a fiber with a larger radius even when the evaporation rate is larger, exactly as is observed experimentally in Figure 8.....114

Figure 4.10: (a) Variation of dimensionless final fiber radius  $R$  (scaled with radius at the droplet) with evaporation rate  $\alpha$  as we vary surface tension  $\gamma = 0.02, 0.5, 2, 8, 30$ , with  $g = G = 1$ . (b) Variation of dimensionless final fiber radius  $R$  (scaled with radius at the droplet) with

surface tension  $\gamma$  as we vary evaporation rate  $\alpha = 0.1, 0.2, 0.3, 0.4, 0.5, 0.6$ , with  $g = G = 1$

. (c) 3D-master plot showing dependence of final radius on  $\alpha$  and  $\gamma$  when  $g = G = 1$   
.....115

Figure 4.11: Variation of dimensionless final fiber radius  $R$  (scaled with radius at the droplet) with viscosity  $\mu$ . Here  $g = G = 1$  and we take  $\gamma = 5/\mu$ ;  $\alpha = 0.3/\mu$  .....116

Figure 4.12: SEM images of a (a) microfiber from the solution of PCL (Mw~80k) 10wt% in chloroform, and (b) nanofiber from the solution of PEO (Mw~8000k) 0.5wt% in water using gravitational dry-spinning technique.....117

Figure 4.13: SEM images of (a) fiber from the solution of Triton 0.05wt% in PEO in water; (b) fiber from the solution of Triton 0.1wt% in PEO in water.....120

Figure 4.14: (a) Twisted and (b) straight fibers using gravitational dry-spinning technique.....121

Figure 4.15: (a) straight fibers: including PCL straight fiber (diameter of 1 to 2  $\mu\text{m}$ ) embedded with silver nanowire (diameter = 90 nm, Length = 30  $\mu\text{m}$ ); (b) twisted fibers: including plain PCL fiber twisted with PCL fiber (diameter of 1 to 2  $\mu\text{m}$ ) embedded with silver nanowire (diameter = 90 nm, Length = 30  $\mu\text{m}$ ).....122

Figure 4.16: z-stack confocal images of the RAW264.7 murine macrophages attached to the gravitational-spun PCL fibers. The layers of PCL fibers were separated by 100- $\mu\text{m}$  thick PGA sutures. The cells infiltrated into the 3D-scaffold.....123

Figure 5.1: Electrochemical samples consisted of (a) Ti/TiO<sub>x</sub>, TiO<sub>x</sub>/silane, or TiO<sub>x</sub>/silane/SWNT samples of equal surface area; (b) representative cyclic voltammograms of the three surfaces showed enhanced reductive currents for the TiO<sub>x</sub>/silane/SWNT surfaces, relative to the TiO<sub>x</sub>/silane samples, indicating that the SWNTs facilitated the reduction of Cu; (c) i vs. t traces obtained at a constant potential of 0.10 V vs. Ag/AgCl, for a total of 16.7 mC

of charge, displayed a sigmoidal shape for the  $\text{TiO}_x/\text{silane}/\text{SWNT}$  samples, indicative of enhanced instantaneous and progressive nucleation processes; (d) Raman microscopy revealed that the Cu species varied with the nanoparticle size. ....152

Figure 5.2: Representative AFM micrograph ( $8 \times 8 \mu\text{m}$ ) showing nanoparticle growth on the  $\text{Ti}/\text{TiO}_x$  surface after deposition at 0.10 V for a charge of 16.7 mC. Each nanoparticle reveals the location of a conductive pinhole (low valence Ti oxide, or conductive grain boundary) through the dielectric  $\text{TiO}_2$  surface .....154

Figure 5.3: Representative AFM image ( $8 \times 8 \mu\text{m}$ ) of the  $\text{TiO}_x/\text{silane}$  samples showing how the addition of a silane monolayer resulted in smaller and more closely clustered nanoparticles than those observed on the  $\text{Ti}/\text{TiO}_x$  surface .....155

Figure 5.4: This representative AFM image ( $8 \times 8 \mu\text{m}$ ) of a  $\text{TiO}_x/\text{silane}/\text{SWNT}$  sample shows that the deposition of a low-density network of SWNTs provided nucleation points for  $\text{Cu}_2\text{O}$  along the conductive sidewalls of the nanotubes, as observed from the greatly increased density of nanoparticles observed. This presents a unique opportunity to decrease the interfacial R at SWNT/metal electrode interfaces .....156

Figure 5.5: (a) The effect of Cu nanoparticle deposition on the two terminal R of aligned (left), and crossbar (right) networks (schematic, not drawn to scale); (b) representative  $i$  vs.  $t$  curves for the two types of networks showed that when the charge allowed to pass was limited to 16.7 mC, the higher current densities for the crossbar networks caused them to achieve that value at significantly shorter times .....157

Figure 5.6: (a) The source/drain electrode pair, and the SWNT network between, served as the working electrode during the electrodeposition of various amounts of  $\text{Cu}_2\text{O}$  nanoparticles at 0.10 V vs.  $\text{Ag}/\text{AgCl}$ . The charge was used to tune the amount of metallization that

occurred; (b) sub-10 nm sized  $\text{Cu}_2\text{O}$  nanoparticles were consistently observed on the SWNTs that bridged the source/drain channel between the Ti/TiO<sub>x</sub> electrodes. ....158

Figure 5.7: Representative log plots showing the dependence of the change in  $I_{\text{on}}/I_{\text{off}}$  on the alignment of SWNTs comprising the network revealed that (a) partially aligned SWNTs allowed for reduced R and greater improvements in  $I_{\text{on}}/I_{\text{off}}$  than (b) orthogonally oriented SWNTs, as the increase in  $I_{\text{on}}/I_{\text{off}}$  observed was 211- and 35-fold, respectively. Insets: two-terminal  $i$  vs,  $V$  curves obtained in the range  $\pm 0.10$  V showed that a greater reduction in R was achieved for “crossbar” networks.....159

## CHAPTER 1

### INTRODUCTION AND LITERATURE REVIEW

#### 1.1 Introduction

When the size of fibers decreases to nanometers, their large surface-to-volume ratio make the nanofibers great candidates to overcome the challenges in biomedical engineering, tissue regeneration, energy storage, textile, sensors, photovoltaic cells, fuel cells, medicine, drug delivery, catalysis, and healthcare products.<sup>1-16</sup> Fibers are also used as the membranes for water treatment since they deal more effectively with chemical and biological threats. Also, fibers can be used to convert the energy sources to electricity more efficiently and this eliminates the need for the crude oil in the future.<sup>17</sup>

The high surface area and controlled porosity enable the micro- and nanofibers to adsorb a tremendous amount of toxins and odors. Therefore, micro- and nanofibers can be used to fabricate the microengineered scaffolds for tissue engineering. These scaffolds can be impregnated with drugs to enhance the wound- and dermal burn healing. The scaffold efficiently releases the antimicrobial and anti-inflammatory compounds which speeds up the healing process and decreases the medical cost and wound care supplies.<sup>18</sup> Nanofibers, also, have attracted broad attention in cancer treatment. Jain et al have exhibited the use of polycaprolactone (PCL)-based nanofibers as a conduit to guide the aggressive glioblastoma tumors from the brain to a cytotoxic hydrogel outside of the skull.<sup>19</sup> The glioblastoma cells probably formed an initial aligned monolayer along the fibers, which serves as a guide for the subsequent tumor cells, therefore, this

process resulted in reducing the tumor load in the brain. This method is quite efficient when it is difficult to treat or completely remove the tumors.<sup>19</sup>

The nanostructured scaffolds have been used tremendously for the biomedical and biological applications mainly because their nanoscale dimension mimics natural extracellular matrix where cells can interact efficiently. The polymeric nanofiber is particularly useful due to its high surface area and porosity which enhance cell adhesion.<sup>20-21</sup> Particularly, aligned fibers have provided better contact guidance effects on the neurite outgrowth of primary cortical neurons and PC-12 cells, which makes them feasible scaffolds for nerve tissue repair arising from the spinal cord injury or peripheral nerve injury.<sup>22-23</sup> The recent discovery of the use of nanofibers to form bones and tissues in combination with stem cells<sup>24-25</sup> has resulted in a significantly increased interest in the development of simple methods for nanofiber fabrication that can be conducted in biological and biomedical laboratories. However, problems of antigenicity and immunogenicity of a donor's biological materials, as well as specific needs in the shapes, dimensions and morphologies of tissue implants call for the fabrication of customized scaffolds<sup>26-27</sup> that can be engineered and fabricated at a health-provider facilities.

Enhancing the mechanical properties of the fibers improves their application in various fields of study. In most of the applications, nanofibers with high strength, modulus, and toughness are required. In some biological materials such as spider silk, high tensile strength and high toughness are achieved simultaneously. However, most of the commercial high-performance fibers reveal strength-toughness trade-off which results in high strength and low toughness, therefore, these fibers are brittle and they break at lower strains. The size of the fibers can affect their mechanical characteristics. As the diameter of the fiber decreases to the nanometer scale, elastic modulus and strength increase due to the improved chain orientation in the ultrafine

nanofibers which leads to simultaneous increase in the strength and toughness of the nanofibers. Papkov et al studied the size effects on the mechanical properties of the polyacrylonitrile (PAN) nanofibers.<sup>28</sup> They reported that as the diameter of the fibers decreased from 2.8  $\mu\text{m}$  to  $\sim 100$  nm, the strength, modulus, and toughness of the nanofibers increased 117 folds, 134 folds, and 2420 folds, respectively. The maximum strength and modulus studied were  $\sim 10$  times greater than those of commercial PAN microfibers (Figure 1.1).<sup>28</sup>

Recently, there has been a huge demand for the fibers with enhanced mechanical properties and an increased number of techniques have been developed to fabricate the fibers with unique features. Most of the fiber spinning techniques have been used to produce the fibers thicker than 2 micrometers, therefore, novel methods need to be investigated to fabricate the nanofibers with superior mechanical properties. Electrospinning<sup>9</sup> is so far the only method with potential for the commercial production of nanofibers, and the major issue yet to be resolved is how to substantially scale-up the production to match the demands from a range of potential markets. Some of the techniques such as melt-blowing<sup>29</sup> are limited to a specific range polymers and also hot air flow needs to be provided to decrease the diameter of the nanofibers. Other techniques such as the phase-separation<sup>30</sup> and self-assembly<sup>31</sup> produce non-uniform fibers and there is no potential for scale-up. Another method known as force-spinning<sup>32</sup>, may overcome some of the limitations since no high voltage or solvent recovery are required, however, there is a risk of thermal degradation when high temperature is applied in the process.<sup>33</sup> The detailed advantages and disadvantages of these techniques are as follows.

## 1.2 Methods for Fabrication of Micro- and Nanofibers

### **1.2.1 Electrospinning**

Electrospinning<sup>9</sup> has been used commercially to synthesize the micro- and nanofibers for various biomedical applications. The process of electrospinning was described by Cooley<sup>34</sup> and Moore<sup>35</sup> in 1902 and the further development was patented by Antonin Formhals<sup>36</sup> in 1934. This technique is extensively applied for the micro- and nanofibers production from a variety of natural and synthetic polymers.<sup>37-38</sup> In electrospinning, an electric field is subjected to a droplet of a polymer solution and the body of the liquid becomes charged. At a critical point, the repulsive electrical forces overcome the surface tension of the droplet and the charged droplet forms a conical shape, known as the “Taylor cone”.<sup>17</sup> At this point, a jet of the solution is erupted from the tip of the Taylor cone and an unstable whipping of the jet occurs in the space between the capillary tip and a grounded collector (plane electrodes or frames). As the solvent evaporates, 2D and 3D fibrous nonwoven structures form on the collector (Figure 1.2).<sup>39</sup> The major challenges encountered in using electrospinning is that it requires high voltages (20-30 kV) and it depends on the dielectric properties of the materials<sup>37</sup>, therefore, the spinning solutions are limited and only experienced operators may be eligible to use the spinning set-up.<sup>40</sup>

Solution electrospinning and melt electrospinning are the two main groups of this technique with the setup similar to the conventional electrospinning. The solution electrospinning process requires volatile solvents. The throughput of the nanofibers in the solution electrospinning has been a serious problem (up to 300 mg/hr). Different attempts have been applied to increase the productivity in solution electrospinning such as increasing the number of jets from single needles or multiple needles. Even, the addition of multiple needles might not increase the productivity since the failure of the central needles can be attributed to the low inter-nozzle distance causing

electric field shielding near the central needles. In contrast to the solution electrospinning, the melt electrospinning eliminates the need for the volatile solvents, but high temperature is needed to melt the polymer. It also, suffers from lack of control on the fabrication of the nanofibers due to the high viscosity of the polymer melts. In both solution and melt electrospinning, the feed rate, the molecular weight of the polymer, and the diameter of the spinneret affect the size of the fibers.<sup>33</sup> In order to enhance the integrity of the fibers, the solvent needs to have suitable vapor pressure, viscosity, and surface tension.<sup>41</sup>

Many polymer materials are difficult to be optimized with electrospinning, due to their poor viscoelastic behavior, lack of the sufficient molecular entanglement, and limited solubility.<sup>42</sup> The concentration of the polymer solution, flow rate, applied potential, and the distance between the needle and the collector are the main parameters that affect the diameter of the fibers. Despite its popular use in tissue engineering applications, several reports have shown detrimental effects of the high voltage on the loaded biomolecules in the electrospun fibers.<sup>43-45</sup> Hence, it is becoming increasingly apparent that there is a need to develop a new technique to produce polymeric nanofiber with enhanced biocompatibilities.

### **1.2.2 Force-Spinning**

The centrifugal spinning was first patented by Hooper in 1924 for producing artificial silk threads using a rotary disc with holes on the side nozzle.<sup>32</sup> Recently, the Forcespinning<sup>TM</sup> method has been commercialized by FibeRio Technology Corporation.<sup>16</sup> It minimizes most of the challenges encountered on the electrospinning technique such as the application of the very high voltages and dielectric solutions.<sup>33</sup> Forcespinning<sup>TM</sup> can be used to spin the fibers from a wide range of conductive and nonconductive materials with higher throughput and lower cost. In addition, no toxic solvents are used to prepare the solutions and therefore, no solvent recovery is

required. This method is efficient for spinning fibers from the solutions, emulsions, and melts. During the process, a high temperature is needed to melt the solid material and a centrifugal force is applied to rotate the heated material at a very high speed to fabricate the fibers. The aerodynamic environment and the inertial force of the rotating spinneret stretch the fiber into the nanoscale (Figure 1.3). The geometry and morphology of the fibers are controlled by the rotational speed of the spinneret, nozzle configurations, rheological properties, and temperature. Besides using high temperature, another limitation of this method is that Forcespinning™ has not been very efficient to spin the fibers from the polymer materials with very low molecular weights ( $M_w$  less than 100,000) and it is mostly due to the lack of inter-chain entanglements.<sup>41</sup>

### **1.2.3 Melt-Spinning**

The melt-blowing method was initially developed by the Naval Research Laboratory under U.S. government sponsorship in the 1950s for the fabrication of the microfilters to trap the radioactive particles in the upper atmosphere.<sup>29</sup> Recently, a number of companies such as Exxon Chemical, 3M, and Kimberly-Clark have extensively used this technique to produce nonwoven microfibers for a wide range of applications such as medical use, filters, and absorbents. In 2004, the nonwovens industry was worth 14\$ billion and this method is continuously attracting more attentions due to its new applications.<sup>46</sup>

In the melt-blowing process, the high-velocity air blows the polymer melt through the orifice of a die and the elongated polymer fibers are collected in the form of a nonwoven web (Figure 1.4). The diameter of the fibers depends on the different parameters such as the polymer type, molecular weight, melt viscosity, geometry of the die tip, the distance from the die tip to the collecting drum, collection speed, throughput, melt temperature, air temperature, and air velocity.

In contrast to electrospinning, this technology is used to fabricate the microfibers with higher production rates and it does not form a huge amount of toxic vapor wastes.<sup>46</sup>

The conventional microfilters exhibited efficiency in removing the micrometer-sized particles. However, the smaller particles can be efficiently collected, if the filters are composed of the nanofibers. Recently, researchers were able to enhance the efficiency of the melt-blown fibers by decreasing the diameter of the fibers by using dies with a small orifice and reducing the viscosity of the polymer melt. In a work by Podgorski et al<sup>47</sup>, the polymer nozzles were surrounded by air nozzles and they produced nanofibers as small as 200 nm in diameter. In another study, Brang et al<sup>48</sup> fabricated nanofibers by melt-blowing using a spinneret die having spin holes formed by grooves. The grooves were smaller than 0.005" wide×0.004" deep and had a length over diameter ratio (L/D) of 20:1 and the polymer feed rate was as low as 0.01 g/hole/min during the melt-blowing. The low throughput with low feed rate was fixed by increasing the density of the spin holes to up to 100 holes per inch. The process resulted in the production of the fibers thinner than 500 nm at a production rate of 1.5 kg/meter/hr.<sup>33</sup>

The melt-blowing method encountered some challenges to produce the nanofibers. Mainly, designing very small orifice in the die is difficult. In addition, using the highly viscous polymer melts and rapid cooling of the fiber as it leaves the die can prevent the production of the nanofibers. This can be compensated by providing the hot air flow in the same direction of the polymer melt flow, but, there is a risk of polymer degradation at the very high temperatures.<sup>33</sup>

#### **1.2.4 Wet/Dry-Spinning**

In dry spinning<sup>49</sup>, a polymer solution is extruded through orifices to create filaments and the fiber is solidified as the solvent evaporates due to exposure to air. Wet spinning<sup>50</sup> is similar to

dry spinning, however, a fluid is required to extract solvent from the filament to fabricate fibers. These methods do not allow for fabrication of sub-micron fibers.

The concentration of the solution, diameter of the orifice, temperature, extrusion rate, and length of the air gap affects the diameter and mechanical properties of the extruded fibers in both dry spinning and wet spinning.<sup>51</sup> A modified dry spinning, called micropipette drawing<sup>52</sup>, is shown in Figure 1.5.

### **1.2.5 Touch-Spinning**

We developed a scalable, inexpensive, and controllable method named touch-spinning<sup>53</sup> which can be used to fabricate micro- and nanofibers from polymer solutions or melts using a rotating rod. In this simple and controllable process, a rotating rod (or a set of rods) is glued to a spinneret whose diameter can be chosen over a wide range of a few centimeters to more than one meter. The polymer solution is pushed through a syringe and the droplet is formed at the tip of a needle. The distance between the polymer droplet and the tip of the rod on the spinneret is adjusted so that the rod contacts the polymer droplet as the spinneret rotates. Following the initial “touch”, the polymer droplet forms a liquid bridge. As the spinneret rotates, the liquid bridge stretches and fiber length increases with the diameter decreasing due to mass conservation. The surface area of the liquid thread increases with its elongation and thus generates a larger surface area for eventual solvent evaporation from the thread. The fibers can easily be collected on the coverslip or any object which is held at the center of the spinneret for further biological studies. The micro- and nanofibers are homogeneous in diameter along the fiber length. The resulting fiber diameter is controlled precisely in the range of 40 nm to 5  $\mu\text{m}$  by adjusting the rotational speed and polymer concentration. This method eliminates the effects of dielectric properties of the polymer solutions associated with electrospinning.

The touch-spinning set-up (Figure 1.6) can be used to wind a single filament into unidirectional, orthogonal or randomly oriented 2D and 3D scaffolds with controlled density, porosity, and thickness.

The touch-spinning method can also be used for drawing fibers from polymer melts. For example, touch-spun polyethylene microfibers can be drawn from polyethylene (PE) melted by a heat gun at 150°C (Figure 1.7f). For a polymer melt, the fiber drawing is followed by cooling of the polymer. Moreover, the touch-spinning method can be used to produce core-shell nanofibers like PVA-PCL using a coaxial needle (Figure 1.7h).

In contrast to electrospinning, the touch-spinning technique does not depend on the dielectric properties of the solvents thus, it can be used to draw fibers from various polymer solutions and melts. For example, Teflon is only soluble in liquids with low dielectric constants, therefore, Teflon nanofibers can be fabricated by electrospinning only if it is blended with another polymer.<sup>54-55</sup> However, the touch-spinning method can be used to fabricate pure Teflon nanofibers from a solution of TAF 1600 (copolymer of 2,2-bis(trifluoromethyl)-4,5-difluoro-1,3-dioxole) in Fluorinert® FC-40 fluid with a very low dielectric constant,  $\epsilon = 1.9$  (Figure 1.7g). Since the touch-spinning method does not depend on the dielectric constant the biocompatibility of the fiber fabrication process enhances considerably. Also, for the preparation of scaffolds, the growth factors and other biomolecules can be incorporated into the polymer solution before spinning the fibers. The fiber diameter decreases with increasing rotational speed and decreasing polymer concentration.

A key advantage of the touch-spinning process is its ability to generate fibers with a uniform diameter. During drawing, the fiber stretches via two distinct mechanisms: 1) axial stretching due to the rotation of the stage, and 2) capillarity forces, which acts to drain fluid from

the fiber back into the source droplet. In addition, the surface tension will act to smooth out any axial variations in radius during the drawing stage (which typically occurs on a millisecond timescale) and hence it is expected to observe uniform thinning for the bulk of the fiber. Due to the uniform nature of the fiber shape during the drawing (stretching) step before fracture, the fiber will also continue to thin uniformly during the evaporation stage. Thus, both the drawing and the evaporation steps ensure that uniform fibers are generated.

In touch-spinning, the density, thickness, porosity, and diameter of the nanofibers can change by adjusting the spinneret rotation speed, flow rate of the solution, concentration of the polymer solution or melt, and the spinning duration. Thinner fibers can be fabricated by decreasing the concentration of the polymer solution or increasing the spinning rate.

The mechanical properties of the touch-spun fibers are also comparable with the mechanical properties of fibers produced by other common methods. For instance, the Young's modulus of the PCL fibers with diameters from 650 to 800 nm was measured to be  $0.26 \pm 0.08$  GPa, using a three-point bending test and an Atomic Force Microscope (AFM).

The touch-spinning technique can simply be scaled up by using a rotating hairbrush composed of hundreds of filaments. The brush rotates very close to the polymer solution underneath it and as the filaments rotate and touch the solution, the fibers are formed. The total length of the fibers produced by the 600-filament brush with a 60-mm wide spinneret at 3000 RPM in 5 minutes is 1700 km, which is a sufficient amount for a typical tissue-engineering experiment.

For the tissue engineering and biomedical application, it is possible to simultaneously spray the cells on the touch-spun mesh which is held by a spool at the center of the spinneret. For this purpose, the spool can be tilted at any angle to wind the fibers onto the frames with complicated geometries. Fibers are wound onto the frame with a controlled density that can be regulated by the

motion of the spool that shuttles back and forward. Simultaneously, the cells can be sprayed onto the frame with winding of the fibers.

The essential difference of the touch-spinning method from other commonly used methods of nanofiber fabrication is in the mechanical control and manipulation of nanofibers that it offers. In contrast to all other methods, in touch-spinning single filament nanofibers are drawn by the mechanical force that determines not only fiber stretching but also guides fibers onto the spool providing better control over fiber alignment. For example, a supporting frame can be held at the center of the spinneret to collect the fibers that are formed. After a specific period of time, the frame can be rotated by 90° and touch-spinning can be continued for another specific period of time which results in creating a mesh for tissue engineering studies. The mesh size and porosity can be controlled by adjusting the time of touch-spinning. Furthermore, touch-spinning offers opportunities beyond 3D-printing due to the controllable fiber diameter and a several orders of magnitude greater speed of scaffold fabrication. This method can be implemented in the laboratory and industrial manufacturing.

### 1.3 Properties of Scaffolds for Tissue Engineering

Minor immunogenic rejection, risk of disease transmission, limited body supply limit the use of autografts and allografts.<sup>56</sup> Multiple approaches have been developed to create scaffolds for tissue engineering applications to avoid organ transplantation. Three-dimensional printing (3D printing) has attracted lots of attention for easy and quick fabrication of scaffolds with designed structures and interconnected porosity using synthetic biodegradable polymers or natural polymers.<sup>57</sup> There are various challenges in preparation of scaffolds using 3D printing. This approach does not allow the fabrication of nanoscaled structures and that can limit cell attachment.

In addition, vascularization is really challenging in the 3D-printed scaffolds. Vascularization improves the performance of the scaffold and survivability of the cells. The cells initially grow at the periphery of scaffolds, and the interconnected pores and vascularization helps for the continuous ingrowth of cells, flow of nutrients and oxygen, and waste removal.<sup>58</sup>

Another approach is the use of fibrous scaffolds for tissue regeneration. In tissue engineering, cells are seeded into constructs similar to fibrous proteins in the structure of native extracellular matrix.<sup>59-60</sup> The polysaccharide chains and fibrous proteins in natural extracellular matrix provide support for cell attachment and the elastic behavior of fibrous structures enhances cell migration through scaffold.<sup>61</sup> Nanofibers dimensions are on the same scale as those of natural extracellular matrix and they mimic the mechanical and functional properties of the natural tissues. Additionally, the high porosity of fibers, their large surface area, nanoscale dimension, and adjustable diameter have made them great candidates as scaffolds for drug delivery and tissue engineering applications.<sup>62-63</sup>

In a fibrous scaffold, several parameters need to be optimized for a proper tissue regeneration. The cell attachment, proliferation, and differentiation are affected by the scaffold geometry and pore size.<sup>64-65</sup> As the diameter of the fibers decreases, the fiber-fiber contact increases and the pore size decreases.<sup>66</sup> Extremely small pore size and high packing density of the fibers limit cell infiltration which results in non-uniform cell distribution and limited vascularization.<sup>59, 67-68</sup> The minimum pore size needs to be in the range of cellular dimension for a proper cell infiltration, therefore, the minimum pore size depends on the cell types. The flow rate and polymer concentration are the main parameters that can be tuned to optimize pore size. Increasing the diameter of the fibers creates larger pores and enhances cell migration, however, the contact area between cells and fibers decreases. As a result, a balance between pore size and

fiber diameter is necessary for optimized cell infiltration and cell attachment.<sup>59</sup> Ju et al fabricated a bilayered scaffold for tissue-engineered blood vessels using nanofibers to enhance cell attachment and microfibers to provide sufficient cellular infiltration.<sup>69</sup>

In a cell-permeable 3D scaffold, the cells grow and create better mechanical properties in the construct for intracellular signaling. The fibrous scaffold needs to support cell attachment, and the interconnected pores should provide sufficient nutrients/oxygen flow and waste removal.<sup>70-71</sup>

The fibrous scaffolds need to be biodegradable and the fiber meshes should have sufficient mechanical properties to support the 3D cell growth. The electrospun scaffolds limitations are poor mechanical properties, insufficient cell infiltration, lack of vascularization, and slow production.<sup>42,</sup><sup>59</sup> Therefore, new fibrous scaffolds with modified properties are required to be fabricated to overcome these challenges.

#### 1.4 Characterization

The structural characteristics of the PCL nanofibers were analyzed by X-ray diffraction (XRD), which indicated that the degree of crystallization is significantly higher for the touch-spun nanofibers.

Scanning electron microscopy (FEI Teneo FE-SEM) was utilized to observe the morphology of the PCL nanofibers fabricated by electrospinning and touch-spinning. The Fiji<sup>72</sup> software was used to measure the diameter of the nanofibers.

Mechanical strength is a very important feature in the nerve tissues. We employed uniaxial mechanical testing system to measure the mechanical properties of the PCL nanofibers.

The contact angle analyzer with a microscope camera (AmScope) was used to evaluate the surface wettability of the PCL fibers and the untreated glass slide. The contact angle slightly

decreased on PCL film substrates 30 and 60 seconds after the droplet fell on the surface. Contact angle of the PCL nanofibers at 60 seconds was  $47.95 \pm 0.1^\circ$  whereas the contact angle on the glass slide remained at  $0^\circ$ , demonstrating its relative hydrophilic property.

A modular compact rheometer (MCR 302, Anton Paar) was used to measure the viscosity of solutions in different solvents.

The Pendent Drop<sup>73</sup> plugin in Fiji<sup>72</sup> was used to calculate the surface tension of different polymer solutions in various solvents. The contact angle analyzer with a microscope camera (AmScope) was used to analyze the pendent droplet.

### 1.5 Summary and Future Directions

There are many applications for the nanofibers and microfibers in the fields of biotechnology, tissue engineering, nanobioelectronics, textile, and drug delivery, therefore fabrication of uniform and aligned fibers has attracted lots of attention. The fibrous mesh creates porous interconnections which is desirable for cell infiltration, cell attachment, and differentiation.

The techniques that have been developed for the fabrication of tissue-engineered scaffolds suffer from lack of vascularization which is an important factor to guarantee the survivability of the cells by removal of waste and flow of nutrients and oxygen. Most of the common fibrous scaffolds are not appropriate for cell loading because of insufficient mechanical properties. Therefore, there is a growing demand for new fiber spinning methods that are capable of producing fibers with high manufacturing productivity and adequate mechanical properties.



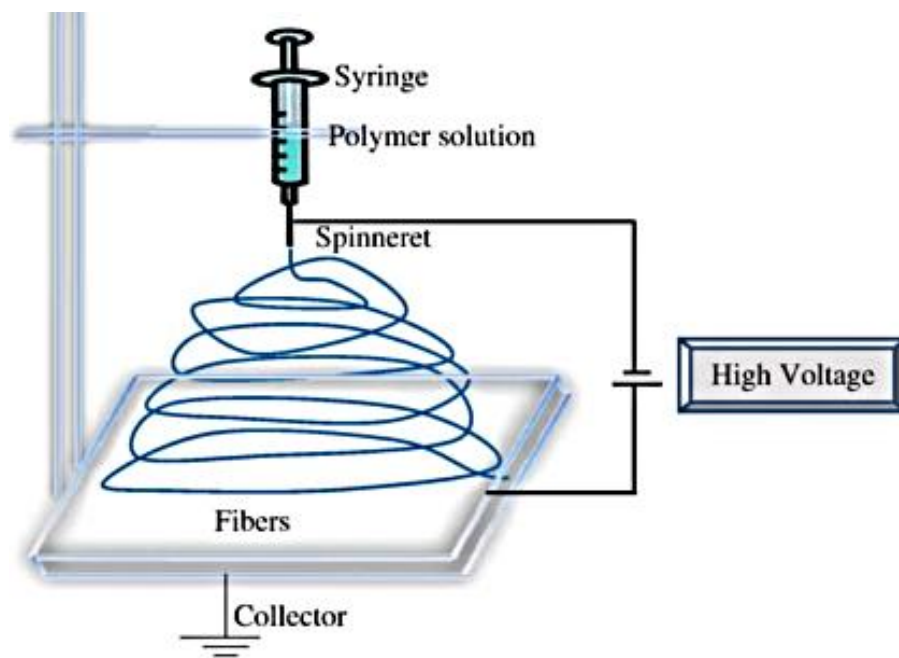


**Figure 1.2.** Electrospinning<sup>17</sup>

(Bhardwaj, N.; Kundu, S. C. *Biotechnology advances* **2010**, 28, 325.)

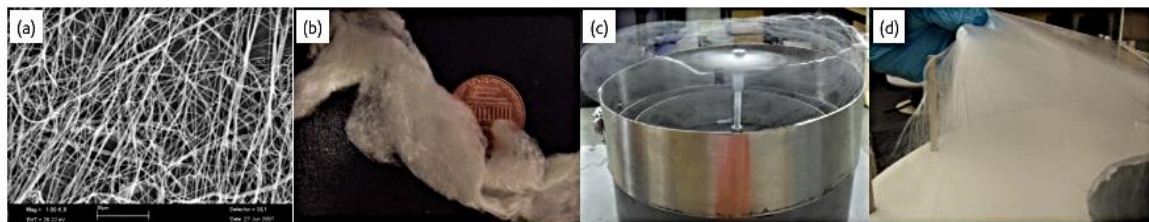
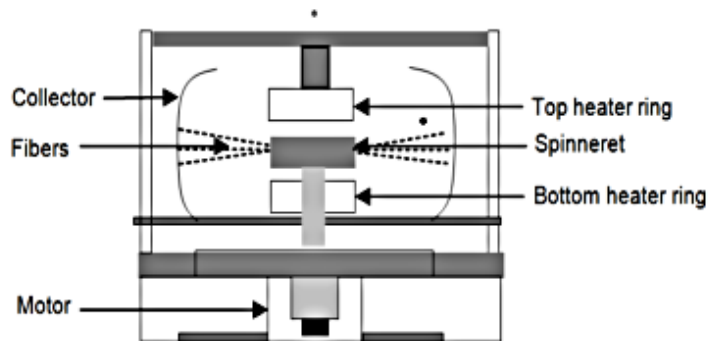
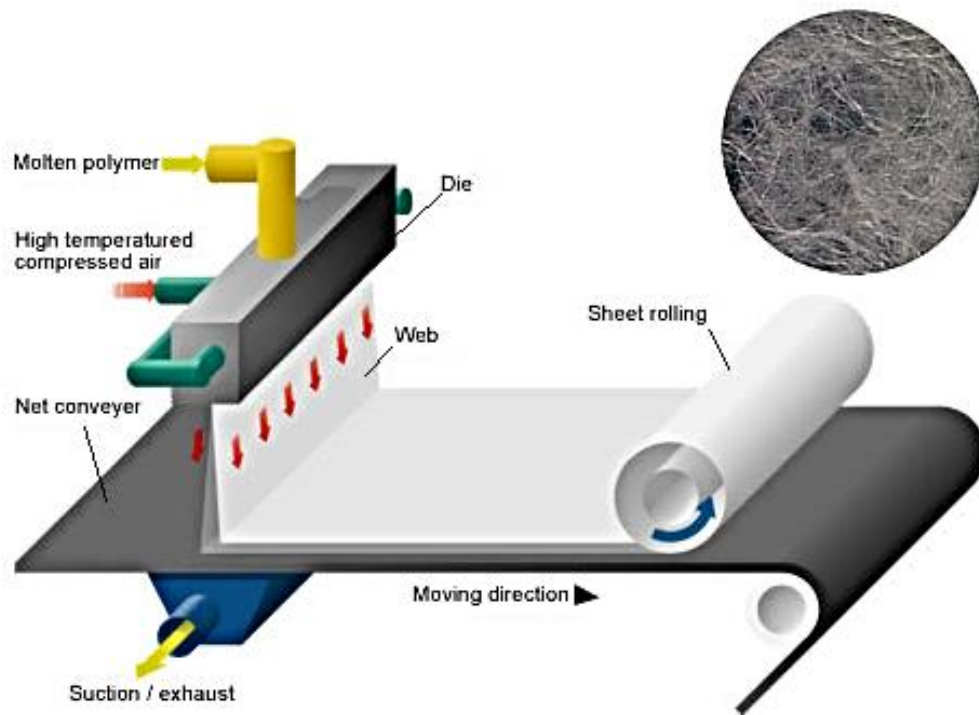


Fig. 2 (a) PEO Nanofibers (Solution) and (b) PS Mat (Melt) produced by the Forcespinning™ Method, (c) nanofiber webs and (d) free standing nonwoven mats also produced by the presented method.

**Figure 1.3.** Forcespinning™<sup>41, 75</sup>

(Raghavan, B.; Soto, H.; Lozano, K. *Journal of Engineered Fibers and Fabrics* **2013**, 8, 52.)

(Sarkar, K.; Gomez, C.; Zambrano, S.; Ramirez, M.; de Hoyos, E.; Vasquez, H.; Lozano, K. *Materials Today* **2010**, 13, 12.)



**Figure 1.4.** Melt-Blowing

(From Shinwa Industrial Co., Ltd. <http://www.shinwa-cc.co.jp/en/products/meltblow.html> )

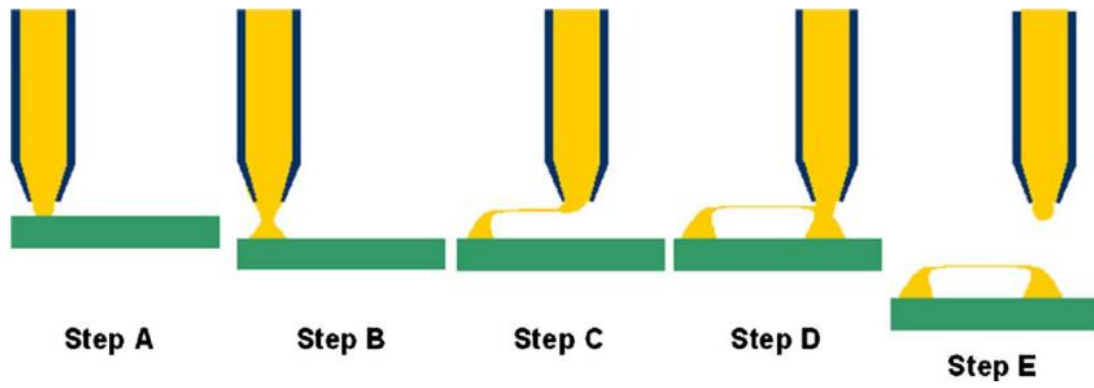


**Figure 1.5.** Direct Drawing of the Nanofibers using a Micropipette<sup>52</sup>

(Nain, A. S.; Wong, J. C.; Amon, C.; Sitti, M. *Applied physics letters* **2006**, *89*, 183105.)

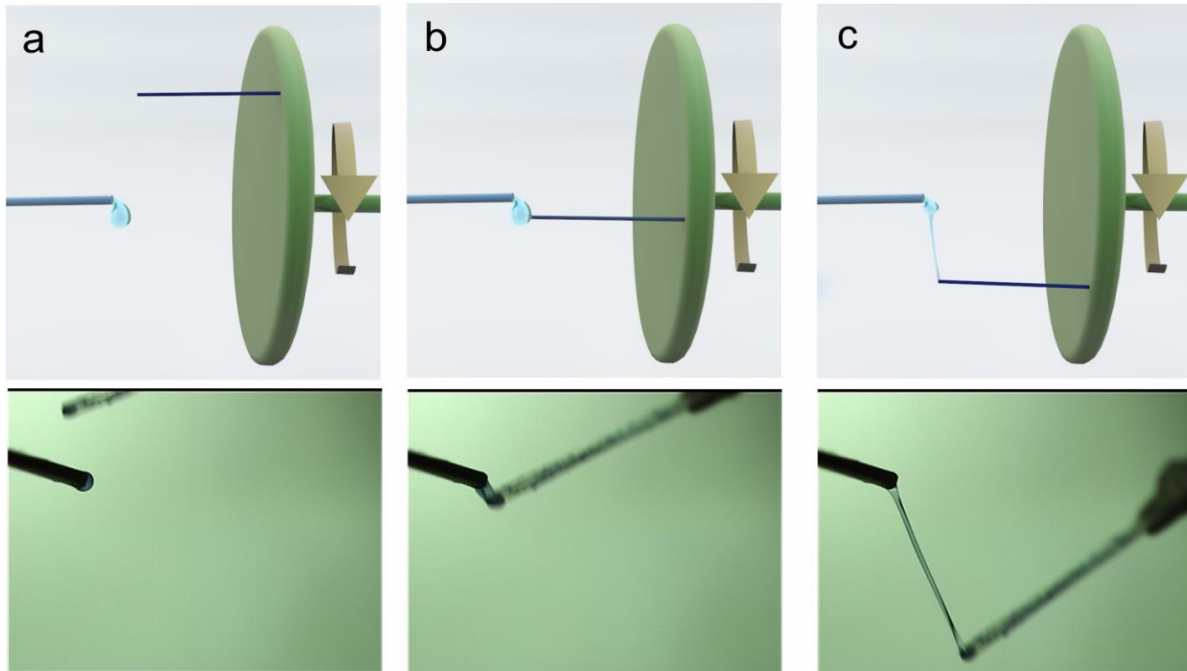


**Figure 1.6.** Touchspinning<sup>53</sup>

(Tokarev, A.; Asheghali, D.; Griffiths, I. M.; Trotsenko, O.; Gruzd, A.; Lin, X.; Stone, H. A.; Minko, S., Touch-and Brush-Spinning of Nanofibers. *Advanced Materials* **2015**, *27* (41), 6526-6532.)

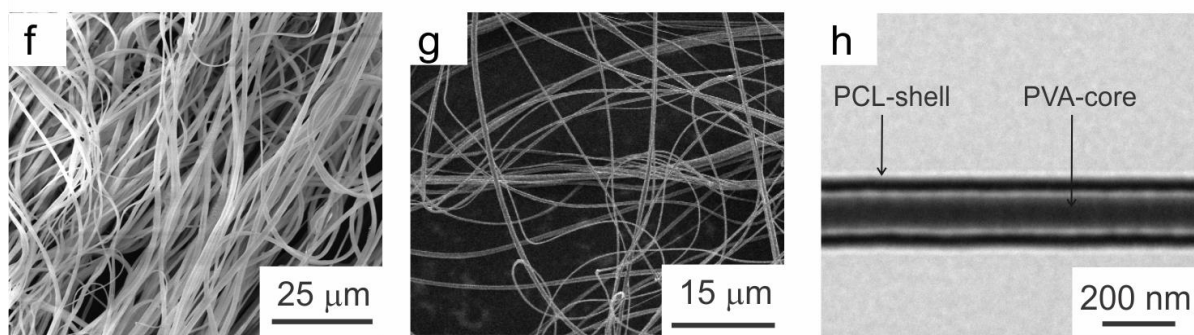


**Figure 1.7.** f) SEM image of PEO nanofibers. g) SEM image of Teflon nanofibers. h) TEM image of a core-shell PVA-PCL nanofiber.

(*Advanced Materials* **2015**, 27 (41), 6526-6532)

## CHAPTER 2

### TOUCH-SPINNING OF NANOFIBERS FOR NERVE REGENERATION<sup>1</sup>

---

<sup>1</sup> S.-J. Lee, D. Asheghali, T. Esworthy, X. Zhou, S. Minko, L. G. Zhang. To be submitted to ACS Applied Materials & Interfaces.

## 2.1 Abstract

Touch-spinning is an inexpensive and scalable method which eliminates the effects of the dielectric properties of polymer solutions associated with electrospinning. A Touch-spinning setup is used for drawing nano- and microfibers from polymer solutions or melts using a rotating rod or a set of rods. In this study, we examined the potential for neural cell proliferation on novel aligned touchspun polycaprolactone (PCL) nanofibers. The aligned electrospun PCL nanofibers with similar diameter and density served as a control group. Neural stem cell (NSC) adhesion and proliferation were similar between touchspun fibers and electrospun fibers over 7 days. The influence of the fiber alignment and bovine serum albumin (BSA) incorporation on NSC differentiation was investigated. Confocal microscopy images showed that NSCs attached and proliferated over all scaffolds up to 8 days. Neurite quantification analysis revealed that the NSCs cultured on the touchspun fibers with incorporated BSA increase the expression of neuron-specific class III  $\beta$ -tubulin after 8 days. More importantly, NSCs grown on the aligned touchspun PCL fibers exhibited a bipolar morphology that oriented along the fiber direction, while NSCs grown on the aligned electrospun PCL fibers had a multipolar morphology. The structural characteristics of the PCL nanofibers were analyzed by X-ray diffraction (XRD), which indicated that the degree of crystallization of the touchspun fiber is significantly higher than that of electrospun fiber. The higher degree of crystallinity of the touchspun fibers resulted in a greater Young's modulus of the touchspun fibers. These findings indicate that the aligned touchspun nanofibers show considerable potential for neural tissue regeneration and tissue engineering applications.

## 2.2 Introduction

Fabrication of nanostructured scaffolds for biological applications has been very promising, as their nanoscale dimension mimics the natural extracellular matrix where cells can interact efficiently.<sup>76-80</sup> The polymeric nanofibers are particularly useful due to their high surface area and porosity, which enhance cell adhesion.<sup>20-21</sup> Additionally, aligned fibers have provided better contact guidance effects on the neurite outgrowth of primary cortical neurons and PC-12 cells, which makes them effective scaffolds for nerve tissue repair for injuries sustained by the spinal cord or peripheral nerves.<sup>23, 81-83</sup> Electrospinning is a conventional method to stretch a droplet of polymer solution and create nanofibers by applying a high-voltage electric field. In addition to a high voltage (~20 kV) electric field, an electrospinning strongly depends on the solvent dielectric properties. Despite its popular use in tissue engineering applications, several reports have shown detrimental effects of the high voltage on the loaded biomolecules in the electrospun fibers, and as such, there have been challenges to retain the bioactivity of loaded drugs and biomolecules, such as bovine serum albumin (BSA) and heparin.<sup>43-45</sup> Hence, it is becoming increasingly apparent that there is a need to develop a new technique to produce polymeric nanofibers with enhanced biocompatibilities.

The touch-spinning technique has been developed recently to create polymer nanofibers without using high-voltage electric fields.<sup>53</sup> In this simple and controllable process, the polymer solution is pushed through a syringe and adhered to a rotating rod or a set of rods on a spinneret in order to draw the fiber from a droplet of polymer solution. The resulting fiber diameter is controlled precisely in the range of 40 nm to 5  $\mu$ m by adjusting the rotational speed and the polymer concentration. The spinning setup can be used to wind unidirectionally, orthogonally, and randomly oriented 2D- and 3D-meshes with controlled density. The fibers can be spun around a

glass coverslip to make scaffolds for further biological studies. Furthermore, touch-spinning offers opportunities beyond 3D-printing due to the controllability of the fiber diameter and a several orders of magnitude greater speed of scaffold fabrication. Thus, due to its ease of use and adjustability, this fabrication method can be implemented in the laboratory and in industrial manufacturing.

Several biomaterials have been investigated for neural tissue engineering. Among these, PCL is a well-known biocompatible polymer on which to grow neural cells. Modifications of PCL by blending with other chemicals or growth factor proteins can closely mimic the physiological microenvironment and can enhance cell growth and differentiation<sup>84-88</sup>. As an example, a study by Taberero et al. demonstrated that albumin can promote neuronal survival by increasing the synthesis and release of glutamate<sup>89</sup>. Here, blended PCL solution with BSA was used to stimulate the cell growth. Specifically, we examined the effects of BSA in both electrospun and touchspun fibers on the neural cell growth and differential potential of neural stem cell. Additionally, the degree of crystallinity is an important factor for polymer materials to interact with cells. Polymers with high crystallinity have higher densities and stiffness's which may influence cell contact guidance. There have been several reports of cellular response to polymers with different crystallinity properties<sup>90-93</sup>, but to the best of our knowledge, the influence of different crystallinity of PCL nanofibers on neural cell behavior has yet to be determined. Some studies have indicated that the electrospun fibers from polymer solutions exhibit lower crystallinity properties than fibers produced from melts.<sup>94-96</sup> In this study, we investigated how touch-spinning affects the degree of crystallinity of PCL nanofibers compared to that of electrospinning.

Mouse neuroepithelial cells (NE-4C) were the preferred cell model for this study as they can display several characteristics of neural stem cells (NSCs) such as nestin and tubulin beta III

immunoreactivity, self-renewal, and differentiation into distinct neural cell types upon appropriate induction.<sup>97-98</sup> In the presence of retinoic acid (RA), NSCs differentiate into neurons and astrocytes in a progressive process, through well-defined stages in which they display specific morphological and cell physiological characteristics.<sup>97</sup> However, to our knowledge, there have been no studies that have demonstrated the alignment of NE-4C cells during the stages of neural differentiation.

This work demonstrated aligned touchspun PCL nanofibers with a high degree of crystallinity to fabricate a first of its kind neural construct and subsequently investigated NSC growth and differentiation therein. The primary objectives of the present study were to (1) evaluate the feasibility of utilizing a touch-spinning setup to create an aligned nanofibrous scaffold, and to (2) examine the proliferative capability and differentiation potential of NSCs in the resultant scaffold *in vitro*.

## 2.3 Experimental Section

### **2.3.1 Polymer Solution Preparation**

PCL ( $M_n = 80,000 \text{ g}\cdot\text{mol}^{-1}$ ) (Aldrich) was dissolved in chloroform (ACS grade, BDH, VWR) for 1 hr at 60 °C to produce a solution with concentration of 8 wt%.

The 0.01% BSA in PCL solution was prepared by dissolving 0.1 mg BSA (Sigma Aldrich, lyophilized powder with MW~66 kDa) in 1 mL of chloroform at room temperature. Then, PCL ( $M_n = 80,000 \text{ g}\cdot\text{mol}^{-1}$ ) (Aldrich) was added to the BSA solution in chloroform to prepare 8 wt% solution.

### **2.3.2 Touchspun and Electrospun Nanofiber Preparation**

For the touchspun samples, the rotation speed of the spinneret was set at 1400 RPM. The setup included two bars that were glued onto the spinneret that simply “touched” the polymer

droplet which was ejected from the tip of a syringe needle (i.d.=0.9 mm) and drew out the fibers as the spinneret rotated and the solvent evaporated. The polymer solution was pushed by an automated pump (Razel Scientific Instruments, variable speed syringe pump, model R99-E) through the syringe (Hamilton™ 1000 series gastight™ syringe, 1 mL) at a flow rate of 10  $\mu\text{L}\cdot\text{min}^{-1}$ . The fibers were spun at room temperature and were collected around a 12-mm glass circular coverslip (Fisher Scientific).

The electrospun samples were prepared utilizing an electrospinning setup (Spraybase®) with a rotating drum collector (Profector Life Sciences Ltd.) with the rotation speed of 1400 RPM. The 8 wt%-PCL solution was pushed through a syringe (Hamilton™ 1000 series gastight™ syringe, 1 mL) at the flow rate of 10  $\mu\text{L}\cdot\text{min}^{-1}$ . The needle (i.d.=0.9 mm) was connected to the voltage of 20 kV and the working distance was adjusted to 110 mm. The fibers were spun at room temperature and they were collected on the 12-mm glass circular coverslip (Fisher Scientific).

### **2.3.3 Fiber Characterization**

A FEI Teneo Scanning electron microscope (SEM) was employed to assess morphology and channel size of prepared touchspun and electrospun fibers. All samples were sputter coated with iridium for 30 s at a coating rate of 0.1 nm/s prior to the imaging.

The crystal structures of the samples were characterized by an x-ray diffractometer (XRD) (PANalytical X'Pert PRO MRD). The XRD scans were recorded with a Cu  $K\alpha_1$  radiation ( $\lambda = 1.541 \text{ \AA}$ ) in the  $2\theta$  range from  $15^\circ$ – $35^\circ$  with a step size of  $0.03^\circ$ .

In addition, Differential Scanning Calorimeter (DSC), TA Instrument DSC SW 9.01, was used to determine the %crystallinity of the touchspun and electrospun fibers. Samples were heated from  $-70^\circ\text{C}$  to  $120^\circ\text{C}$  at a scanning rate of  $10^\circ\text{C}/\text{min}$  under a nitrogen atmosphere.

The contact angle analyzer with a microscope camera (AmScope) was used to evaluate the surface wettability of the PCL fibers and the untreated glass slide.

### **2.3.4 Mechanical Testing**

The fiber samples from both touch-spinning and electrospinning techniques were collected on rectangular frames of the size of 10 mm × 30 mm for the mechanical tests. An electromechanical universal test system (MTS Criterion® Model 42) conducted tensile mechanical testing of the PCL nanofibers under a constant crosshead rate of 2 mm.min<sup>-1</sup>. All prepared scaffolds were further trimmed into 10 mm × 18 mm rectangular sheets and were clasped on each end by the mechanical grips. Five electrospun and five touchspun samples were prepared to find the average Young's modulus values for each spinning method. Young's modulus was calculated by dividing the force on the fiber by the effective cross-sectional area of the fiber, A. The effective cross-sectional area, A, was determined using

$$A = \frac{W}{(L \times PD)}$$

where W represents weight of the fiber, L, the length of the fiber, and PD, the density of PCL (1.145 g.mL<sup>-1</sup>).

### **2.3.5 Culture of NE-4C Neural the Cells on Scaffolds**

NSCs (NE-4C, ATCC) were utilized to evaluate cell responses on various printed nerve scaffolds. NSCs were cultured in Eagle's Minimum Essential Medium (ATCC), 5% fetal bovine serum (FBS, ATCC) and 1% L-glutamine (Sigma-Aldrich). Cells were cultured in the 150 cm<sup>2</sup>-flask under a humidified atmosphere with 5% CO<sub>2</sub> at 37 °C. The culture medium was changed every two days. Prepared scaffolds were punched into small circle samples with a 10-mm diameter. The samples were then sterilized by 70% ethanol for 30 minutes, rinsed and immersed in phosphate buffered saline (PBS) overnight, and pre-wetted in poly-l-lysine at 37 °C before cell seeding. NSCs

were seeded at a density of 30,000 cells per scaffold for a 4-hour cell attachment and 1-, 4- and 7-day proliferation studies. After each prescribed time interval, scaffolds were transferred to new well-plates. A Cell Counting Kit-8 (CCK-8, Dojindo Molecular Technologies, Inc.) was used to assess the NSC viability after a 2-hour incubation at 37 °C. The absorbance was analyzed using a Thermo Scientific Multiskan GO Microplate Spectrophotometer at the wavelength of 450 nm. The adhesion and proliferation studies were repeated three times with three replicates per group, totaling 9 samples per group.

### **2.3.6 Immunocytochemistry of NSCs on the Scaffolds**

For differentiation studies, NSCs were cultured in the respective standard medium with  $10^{-6}$  M RA on the electrospun fibers and touchspun fibers for 8 days. All PCL fibers were prewetted with control media overnight to enhance the cellular attachment. After each culture period, samples were rinsed with PBS and fixed with 10% formalin for 12 minutes at room temperature for the specified time. The cells were further permeabilized with 0.2% Triton X-100 in PBS for 5 minutes. Diluted primary antibody, mouse anti-TUJ1 (1: 1,000; Covance) was gently added in scaffolds and incubated at 4 °C in a moist environment overnight. This was followed by the secondary antibody incubation with Alexa Fluor 594 goat anti-mouse (Life technologies) at room temperature. The cell nuclei were stained by  $10 \mu\text{g.mL}^{-1}$  4'-6-diamidino-2-phenylindole dihydrochloride (DAPI) (Life technologies). Laser scanning confocal microscopy (LSCM 710, Zeiss) was employed to visualize and monitor the fluorescent images of the 3D neural cell growth and neurite extension of the cells.

### **2.3.7 Quantification of Neurite Angle and Length**

Angle measurements were constrained between 0° and 90°. ImageJ<sup>99</sup> (ImageJ; National Institutes of Health, Bethesda, MD) and the NeuriteTracer<sup>100</sup> plugin were used to calculate the

angle between the fibers or channels of the scaffold and the neurite extension. Neuronal cells and neurite expression level were also quantified with the ImageJ software. Image processing for linear color level adjustments in Zeiss Zen were applied identically to all conditions. At least four areas were randomly selected for analysis on each sample (4 samples/group) using a 10x objective. A total of 37 to 441 cells/group were observed with nuclear staining (DAPI) and the portion of neuronal cells, that is, TUJ-1 positive cells, were calculated.

### **2.3.8 Statistical Analysis**

All quantitative data are expressed as average  $\pm$  standard error of the mean. Numerical data were analyzed via student's t-test to determine differences among the groups. Statistical significance was considered at  $p < 0.05$ .

## 2.4 Results

### **2.4.1 Characterization of the Prepared PCL Nanofibers**

FEI Teneo FE-SEM was utilized to observe the morphology of the PCL nanofibers fabricated by electrospinning and touch-spinning. Figures 2.1A and 2.1B represent the aligned PCL nanofibers prepared by electrospinning and touch-spinning methods, respectively. The aligned PCL fibers were successfully fabricated from the 8-wt% PCL solution. Fiji<sup>72</sup> software was used to measure the diameter of the nanofibers. The average diameter of 50 electrospun and touchspun nanofibers were  $481 \pm 80$  nm and  $431 \pm 30$  nm, respectively.

The crystal structures of the PCL nanofibers prepared by two separate spinning techniques were confirmed by XRD analysis and the data has been plotted in Figure 2.2. The peak positions for both electrospun and touchspun PCL fibers were essentially identical; showing two strong peaks at  $2\theta = 21.5^\circ$  and  $23.9^\circ$ , respectively, suggesting no change in crystal structure by fabrication

techniques. However, touchspun PCL fibers exhibited much higher percentage of crystallinity, 71% compared to 51% from the electrospun PCL fibers according to XRD results (Table 2.1). In Table 2.2, the degrees of crystallinity of the fibers have been shown using the first two cycles of DSC spectra. The %decrease of crystallinity from cycle 1 to cycle 2 is much higher in touchspun fibers which may prove the cold-drawing effect in the touchspinning process.

Some studies indicated that electrospun fibers from polymer solutions have a lower crystallinity than fibers produced from melts.<sup>101</sup> In touchspinning, the drawn fiber solidifies when it is pulled by the needle in the direct contact with the fiber. In contrast to electrospinning, the applied force in touchspinning is sufficiently large to stretch the nanofibers at the stage of polymer vitrification. This is equivalent to cold-drawing which improves chain alignment and crystallinity.<sup>102</sup>

Cellular and extracellular matrix alignment is a common feature of biological tissue such as the tracts of aligned cells present within the nervous system<sup>103</sup>. Development of an aligned ECM architecture of native nerve tissue with appropriate restoration of mechanical properties is crucial in clinical repair<sup>103-104</sup>. In this regard, both electrospinning and touchspinning are suitable fabrication techniques as they can produce well aligned fibrous scaffold, which is important for applications involving mechanically anisotropic soft tissues. Specifically, we employed a uniaxial mechanical testing system to measure the mechanical properties of the PCL nanofibers. Elastic stress-strain behavior of both electrospun (Figure 2.3A) and touchspun (Figure 2.3B) fibers showed a non-linear mechanical response reminiscent of soft tissues. It should be noted that the Young's modulus of the touchspun fibers was significantly higher than that of the electrospun fibers, which is in agreement with the %crystallinity values (Figure 2.3C). Specifically, the Young's modulus of PCL touchspun fibers was increased by 6-fold over the electrospun fibers. It

is assumed that the greater toughness of the fibers was primarily due to the greater crystallinity within the fibers. As discussed earlier, the touchspinning technique produced PCL fibers with higher molecular alignment compared to the electrospun fibers.

The static contact angles of a water droplet (5.0  $\mu\text{L}$ ) on the untreated glass slide and the PCL fibers were  $0^\circ$  and  $52.5\pm 0.6^\circ$ , respectively. Contact angle slightly decreased on PCL film substrates 30 and 60 seconds after the droplet fell on the surface. The contact angle of the PCL nanofibers at 60 seconds was  $47.95\pm 0.1^\circ$  whereas the contact angle on the glass slide remained at  $0^\circ$ , demonstrating its relative hydrophilic property (Figure 2.4).

#### **2.4.2 Biocompatibility Analysis of the PCL Nanofibers**

The 4-hour attachment study showed that the NSC adhesion increased by 50% on both electrospun and touchspun fibers compared to the glass substrate (Figure 2.5), however, there was no statistical difference between the electrospun and the touchspun fibers. For the subsequent studies, we incorporated BSA into each PCL fiber to investigate its effect on NSC growth and differentiation. A CCK-8 assay was carried out to evaluate the viability of NSC on the electrospun and touchspun PCL fibers. The CCK-8 assay involves a reduction reaction that reduces the CCK-8 reagent to formazan when incubated with viable cells, providing information about cell growth and metabolic activity of the cells. Figure 2.6 shows the 7-day proliferation of the NSCs on the resultant scaffolds. The NSCs cultured on both electrospun and touchspun PCL fibers have increased by 58% and 71%, respectively, compared to the glass control group at day 7. However, there was no statistical difference between electrospun fibers and touchspun fibers at day 7. Furthermore, the incorporation of BSA did not affect NSC proliferation between electrospun fibers and touchspun fibers throughout the 7 days of cell culture.

### 2.4.3 Early Differentiation of NSCs on the PCL Nanofibers

Confocal microscopy images showed early stages of the neural differentiation stained by TUJ-1 (Figure 2.7A). The NSCs cultured on the glass substrate maintained spherical cluster whereas NSCs cultured on the aligned fibers elongated along the fibers. After 4 days of RA induction, small amounts of TUJ-1 immunostaining appeared on all constructs. Figure 2.7A shows the early neural differentiation of NE-4C cells on various PCL nanofibers. Confocal micrographs show NSCs spreading and morphology on the surface of the aligned PCL fibers as well as on the surface of the glass slide. However, by Day 4, it was difficult to see the orientation of NSCs along the fibers. Figure 2.7B represents TUJ-1 relative expression on the PCL fibers versus the glass slide. As shown on Figure 2.7A, higher TUJ-1 expression levels were more evident on the PCL fibers than on the glass slide. NSCs cultured on the glass slide had about 1.6 TUJ-1 levels compared to ~15 on the PCL fibers. There was a significant difference among the various PCL fibers. The ratio of TUJ-1 and DAPI was also consistent with the relative expression levels of TUJ-1 (Figure 2.7C). The percentage of TUJ-1 positive cells was greatly increased on all PCL nanofibers compared to that of the glass slide (Figure 2.7C). However, it should be noted that incorporation of BSA in touchspun fibers did not appear to change the TUJ-1 expression levels by day 4.

By the 8<sup>th</sup> day of neural differentiation, the clusters of TUJ-1 positive cells were apparent throughout the substrate (Figure 2.8A). TUJ-1 positive cells on the glass slide tended to form a large aggregate and remained within the boundary of DAPI positive cells. TUJ-1 positive cells on the PCL fibers tended to form a smaller aggregate along the fiber. More importantly, longer neurite extension was more noticeable on the PCL fibers connecting between the aggregates. When comparing the TUJ-1 relative values, NSCs cultured on the touchspun fibers with BSA had a

significantly higher value compared to any other groups (Figure 2.8B). Consistently, the value of TUJ-1 expression per DAPI within cells on the touchspun fibers with or without BSA significantly increased compared to glass and electrospun fibers by day 8 (Figure 2.8C).

We also observed enhanced neural alignment on the touchspun PCL nanofibers. Figure 2.9A shows that the touchspun fibers provide a significant degree of neurite alignment on the fibers, with 14% of the neurite segment angles directly matching the direction of fibers and 41% within five degrees of the fiber direction (Figure 2.9C). Neurite angling towards 0 degree along the fiber indicates that the neurites have a strong tendency to orient in the direction of the fiber alignment. Electrospun fibrous scaffolds also supported some level of neurite alignment. Approximately 10% of all neurites were distributed within 5 degrees of the aligned fibers. However, about 52% of all neurites were differentiated at greater than 20 degrees of aligned fibers.

## 2.5 Discussion

### **2.5.1 Touch-Spinning is a Viable Alternative to Electrospinning for Creating Neural Scaffolds**

In this study, we generated PCL nanofibers from two different fabrication methods including the conventional electrospinning method and a novel touch-spinning<sup>53</sup> technique. The touch-spinning set up utilized an automated pump which dispensed the polymer through a syringe at 10  $\mu\text{L}\cdot\text{min}^{-1}$ . Affixed to the syringe was a needle which was placed within close proximity to the spinneret. Two bars were attached opposite each other on the spinneret. The spinneret rotated at 1400 RPM and collected the droplet as it came in contact with the bars. In the center of the spinneret there was a rotating glass coverslip which collected the newly formed fibers. In this simple and scalable technique, the density, thickness, porosity, and diameter of the nanofibers can

be changed by adjusting the spinneret rotation speed, solution flow rate, concentration of the polymer solution or melt, and the spinning duration. This novel fabrication method works independently of the dielectric properties of the polymer solution, which in turn enhances the biocompatibility of the fiber fabrication process. For the preparation of scaffolds, growth factors and other biomolecules can be incorporated directly into the solution before spinning the fibers. One of the most noticeable advantages of touchspinning over other current spinning methods is in its ability to use a two-droplet touch-spinning technique when the polymer formation is diffusion-limited as in ultrafast ion exchange or click chemistry reactions. In this case, two polymer solutions can be pushed through two syringes and the tips of the two needles are positioned in a way that the two droplets are held very close to each other, but not in contact. As the spinneret rotates and the bar on the spinneret touches the droplets from two needles simultaneously, the polymer solutions are drawn fast enough before the crosslinking takes place. For example, alginate nano- and microfibers, which can be used as biodegradable scaffolds for various biomedical applications, can be fabricated through crosslinking with  $\text{Ca}^{2+}$  ions using the two-droplet touch-spinning technique. Other techniques such as co-axial spinning and microfluidic spinning have presented low productivity rates due to the long contact time between the two reactive solutions.<sup>53</sup>

An ideal nerve conduit should have a Young's modulus approaching that of nerve tissues to withstand manual manipulation and *in vivo* physiological loading during nerve regeneration, as well as to retain its structure after implantation.<sup>105</sup> A recent study from Liu et al. showed that the Young's modulus of a human sciatic nerve in the longitudinal direction is in the range of  $40.96 \pm 2.59$  MPa.<sup>106</sup> Both touchspun fibers and electrospun fibers showed a Young's modulus of  $12 \pm 0.9$  MPa and  $79 \pm 11$  MPa respectively, indicating the favorable tensile properties of touchspun fibers.

The higher degree of crystallinity of the touchspun fibers is mainly due to the torsional force being applied to the drawn fiber uniformly and continuously. The needles on the spinneret are in mechanical contact with the polymer droplet and the force is applied to the polymer droplet during the fiber formation process. The hypothesis is that the force is applied to the entire length of the fiber after solidification which is similar to the cold-drawing process. Therefore, there is a possible polymer chain stretching and alignment which enhances the crystallinity degree and elasticity of the touchspun nanofibers. In contrast, the force is applied locally to the polymer droplet in electrospinning and the force is not uniformly applied to the entire length of the fiber, since the electrical force depends on the distance from the needle. This results in lower %crystallinity due to the instability during fiber formation.

### **2.5.2 BSA Incorporated Touchspun Enhanced Early Differentiation of NSCs**

Serum albumin is the most abundant protein component of blood plasma and has been shown to play a crucial role in tissue development.<sup>107-108</sup> BSA has been widely used in cell culture experiments and has been found to be present during the early stages of brain development. It has been suggested that albumin could play an important role in the neural stem differentiation.<sup>89, 109</sup> Furthermore, it is known that BSA can regulate the spread of calcium waves and the rate of astrocyte proliferation. Taberero et al. showed that BSA can strongly increase the flux of glucose and lactate through the pyruvate dehydrogenase catalyzed reaction in the primary cultured astrocytes.<sup>89</sup> In the present study, 0.01% w/v BSA was blended into PCL solution and the fibers were fabricated by electrospinning and touch-spinning methods. We examined how incorporated BSA affects early neuronal differentiation of NSCs by observing  $\beta$ -tubulin class III expression level on the resultant fibers.

When observing NSCs on the touchspun PCL nanofibers with incorporated BSA, it was discovered that  $\beta$ -tubulin class III expression level per nuclei was enhanced compared to those on the electrospun PCL nanofibers after 8 days of culture (Figure 2.8C). When looking at  $\beta$ -tubulin class III expression levels alone, NSCs cultured on the touchspun nanofibers with BSA had significantly higher expression values than any other group. This is indicative that NSCs cultured on the touchspun fibers with BSA were more likely to be differentiated into neuronal lineages as compared to those cultured on the electrospun fibers with or without BSA. There are several possible mechanisms to explain why BSA incorporated in the touchspun fibers greatly promoted early neuronal differentiation compared to the electrospun fibers. An increase in early differentiation of NSCs on the touchspun fibers with BSA may be partly due to the conformational stability of protein.

Protein function is determined by the explicit conformation of the polypeptide chain. The misfolding of proteins results in loss of enzymatic activity and in many cases amyloid fibril formation.<sup>110</sup> Some studies have shown that small electric field compared to the protein intermolecular forces induce changes in BSA conformation.<sup>110-111</sup> Electrospinning involves a high voltage to stretch out polymer fibers, which may diminish the bioactivity of incorporated growth factors by affecting conformational stability as well as enzyme activity.<sup>112</sup> A study by Ji et al. showed that after electrospinning, their electrospun samples showed a significant decrease in enzyme activity of alkaline phosphatase (ALP) compared to freshly dissolved ALP. Secondary structure analysis further confirmed that incorporated proteins of electrospun fiber underwent conformational changes, suggesting that high voltage may be harmful to the loaded biomolecules.<sup>113</sup> In contrast to conventional electrospinning, our novel touchspinning method does

not involve high voltage to produce highly aligned polymeric nanofibers, which may be helpful in preserving the activity and conformation of loaded growth factors.

### **2.5.3 Directed Neurite Outgrowth of NSCs on the Touchspun Fibers**

Figure 2.9A shows the confocal micrograph and neurite traced image of TUJ-1 expression of NSCs cultured on the highly aligned PCL touchspun and electrospun nanofibers. The result exhibits a higher order of alignment of NSCs on the touchspun fibers compared to NSCs on the electrospun fibers. Furthermore, most of the differentiated NSCs exhibited bipolar morphology with two extended neurites on the touchspun fibers, whereas NSCs cultured on the aligned electrospun fibers expressed multipolar processes. These results suggest that the aligned neurite outgrowth of NE-4C cells might be mainly guided by the chemical or physical cues of PCL touchspun nanofibers since there was no obvious oriented neural growth provided by the aligned electrospun fibers.

As we discussed previously, the touchspinning method changed the chemical and mechanical properties of the resultant PCL nanofibers compared to the electrospun fibers. Among those altered features, high crystallinity properties of the touchspun fibers may play an important role in governing neural stem cell growth, spreading, and alignment during the early stage of the neural differentiation.<sup>92</sup> The mechanism of this cell response to crystallization-induced surface is still unclear. But it is well documented that polymers with higher crystallinity result in a stiffer substrate which influence cytoskeletal organization and subsequent cell phenotype.<sup>91, 114-116</sup> Some studies found that highly crystalline or stiffer substrates were found to better support focal adhesion, spreading, proliferation, and differentiation of several stem cells.<sup>91-92</sup> Cui et al. showed that while chemical composition, hydrophobicity, and surface roughness of PCL/PGA polymers were held constant, crystallinity and rigidity of the polymers played major roles in determining

cell response.<sup>92</sup> In that study, highly crystalline and rigid PCL and PGA substrates significantly increased fibroblast growth compared to the amorphous polymer surface. However, it should be noted that other types of cells such as osteoblasts, were found to favor less crystalline substrate for growth and spreading.<sup>92</sup>

To our knowledge, no previous studies have successfully demonstrated the influence of the polymer crystallinity on the alignment of NE-4C NSCs. NE-4C cells tends to form aggregates to induce neural differentiation, which is not particularly conducive for the induction of neural alignment. The present study has demonstrated for the first time that high crystalline PCL touchspun nanofibers can enhance neural alignment of the NE-4C cells.

## 2.6 Conclusion

We report the fabrication of touchspun PCL nanofibers that exhibited a higher degree of crystallinity over the fibers yielded by conventional electrospinning. We demonstrate the enhanced physical, chemical, and mechanical properties of these aligned nanofibers prepared by the touchspinning technique. Specifically, the crystallinity of the touchspun PCL nanofiber was much higher than that of electrospun fibers. Incorporated BSA within the touchspun fibers increased the expression of neuron-specific class III  $\beta$ -tubulin compared to other scaffolds by day 8. More importantly, the aligned PCL touchspun nanofibers promoted aligned neurite outgrowth of NSCs, suggesting its potential utility in treating conditions ranging from spinal cord injury to peripheral nerve lesions.

## 2.7 Acknowledgement

S.-J.L. and L.G.Z. thank the financial support from March of Dimes Foundation's Gene Discovery and Translational Research Grant. D.A. thanks Dr. Nataraja Sekhar Yadavalli for assistance with calculations of crystallinity degree from the DSC and XRD spectra, and Steve Larson from Dr. Yiping Zhao's lab at the University of Georgia for collection of the XRD spectra.

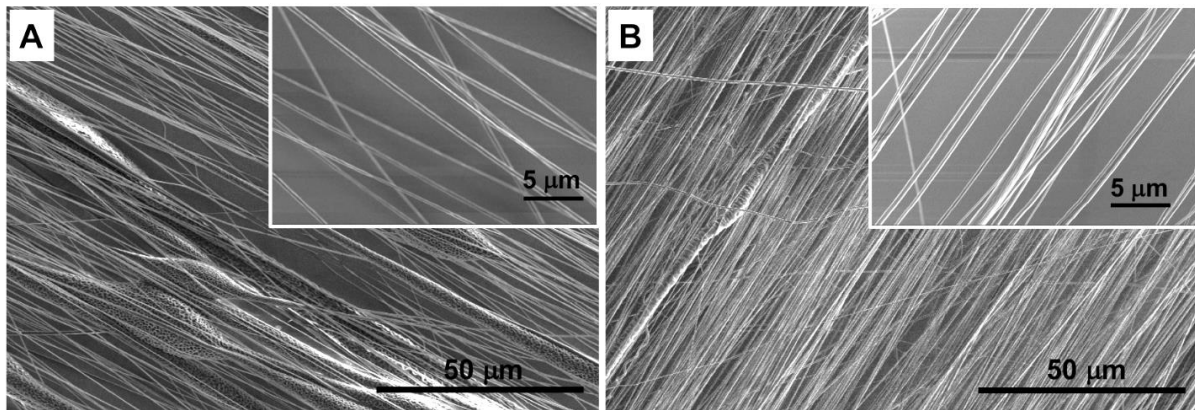


**Figure 2.1.** SEM images of aligned PCL nanofibers prepared by (A) electrospinning and by (B) touchspinning

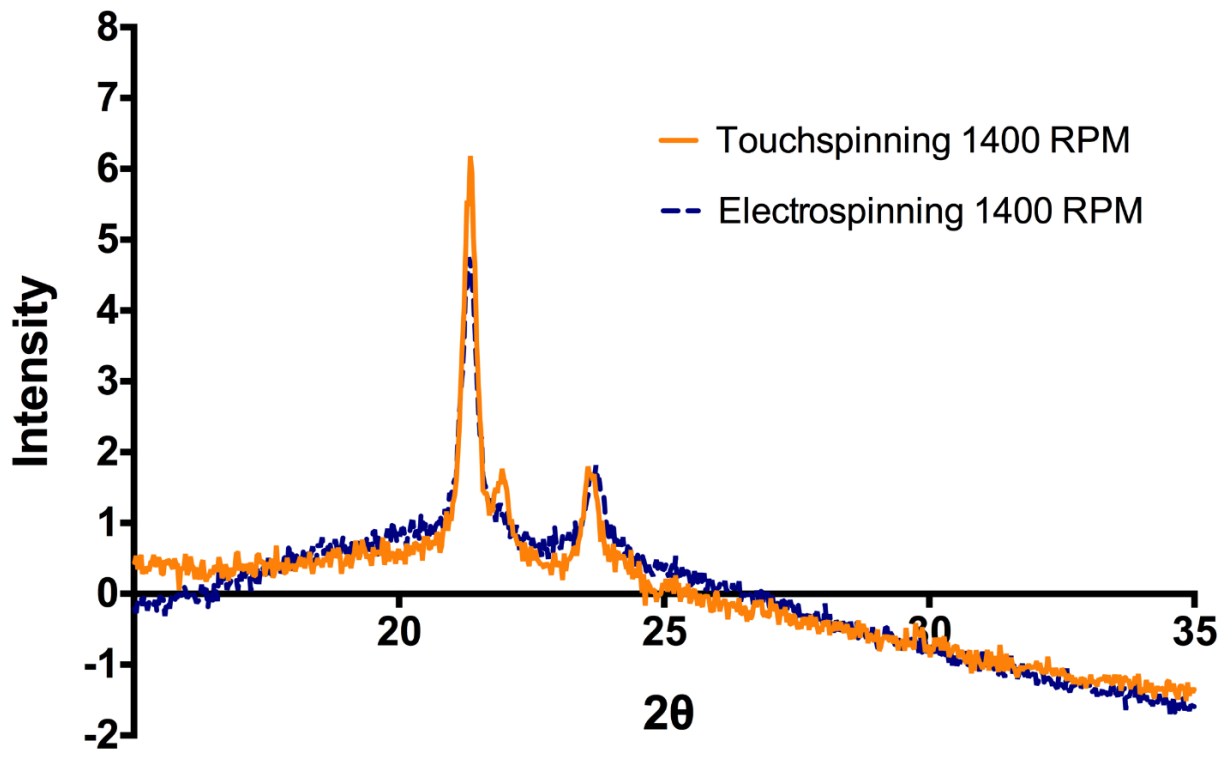


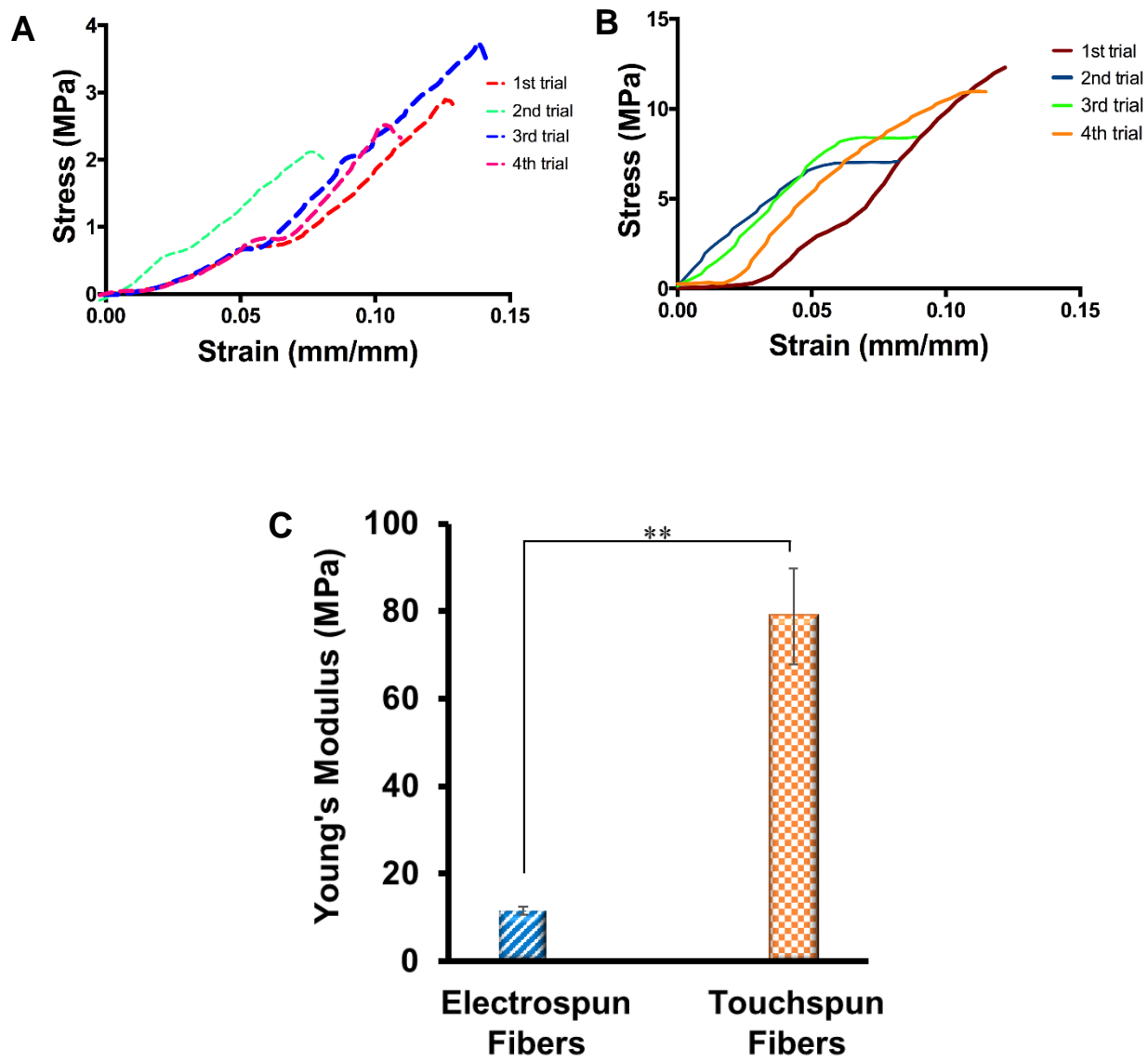
**Figure 2.2.** XRD pattern describing the crystallinity of PCL fibers prepared by touchspinning and electrospinning

**Table 2.1.** % Crystallinity from XRD spectra of the nanofibers fabricated by touchspinning or electrospinning at 1400 RPM.

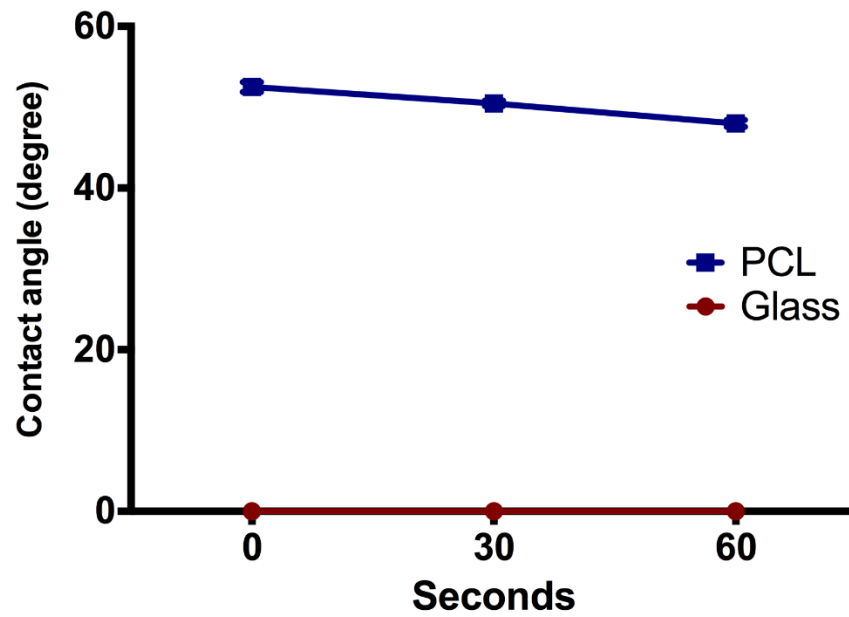
Collector Rotation Speed (RPM)	Touchspun Fibers	Electrospun Fibers
	%Crystallinity	%Crystallinity
1400	71	51

**Table 2.2.** % Crystallinity from DSC spectra of the nanofibers fabricated by touchspinning or electrospinning at varying rotation speeds of the collector.

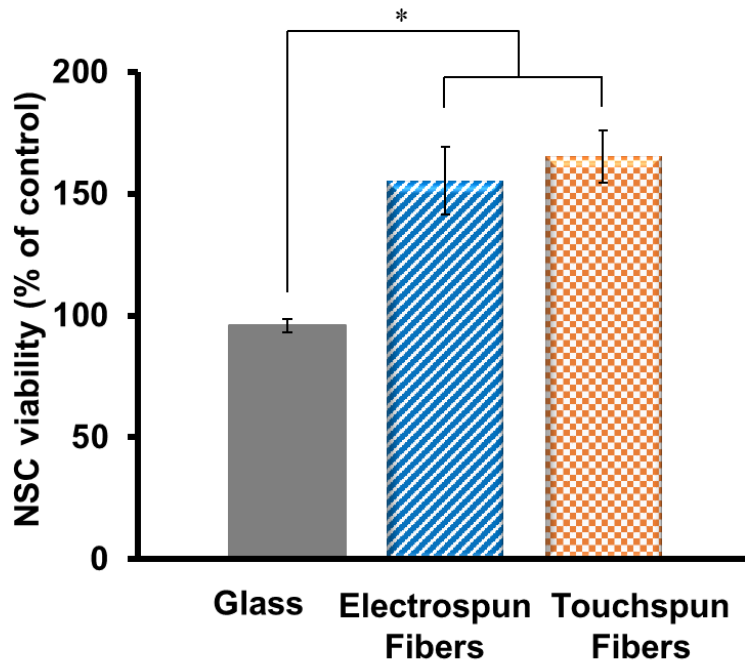
Collector Rotation Speed (RPM)	Touchspun Fibers			Electrospun Fibers		
	%Crystallinity 1 <sup>st</sup> Cycle	%Crystallinity 2 <sup>nd</sup> Cycle	%Change	%Crystallinity 1 <sup>st</sup> Cycle	%Crystallinity 2 <sup>nd</sup> Cycle	%Change
1400	57	47	18	45	42	7



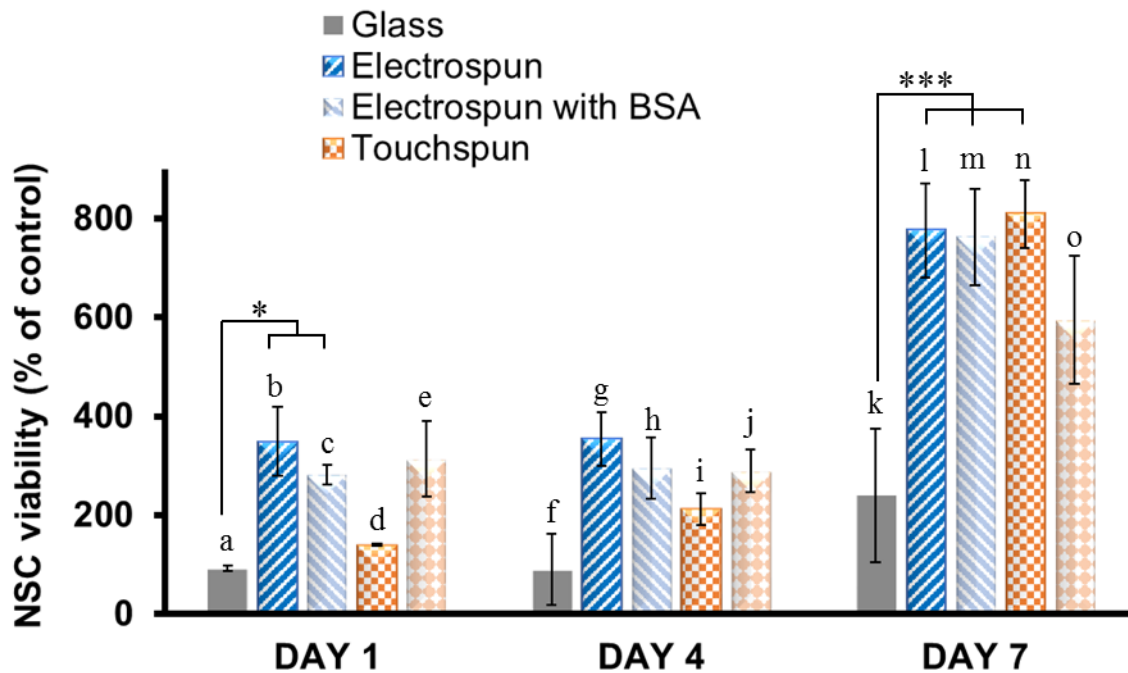
**Figure 2.3.** (A and B) Stress-strain curve of electrospun and touchspun PCL nanofibers, respectively. (C) Young's modulus values for PCL nanofibers. Data are mean  $\pm$  standard error of the mean. n=4; \*\*p<0.01 when compared to electrospun fiber.



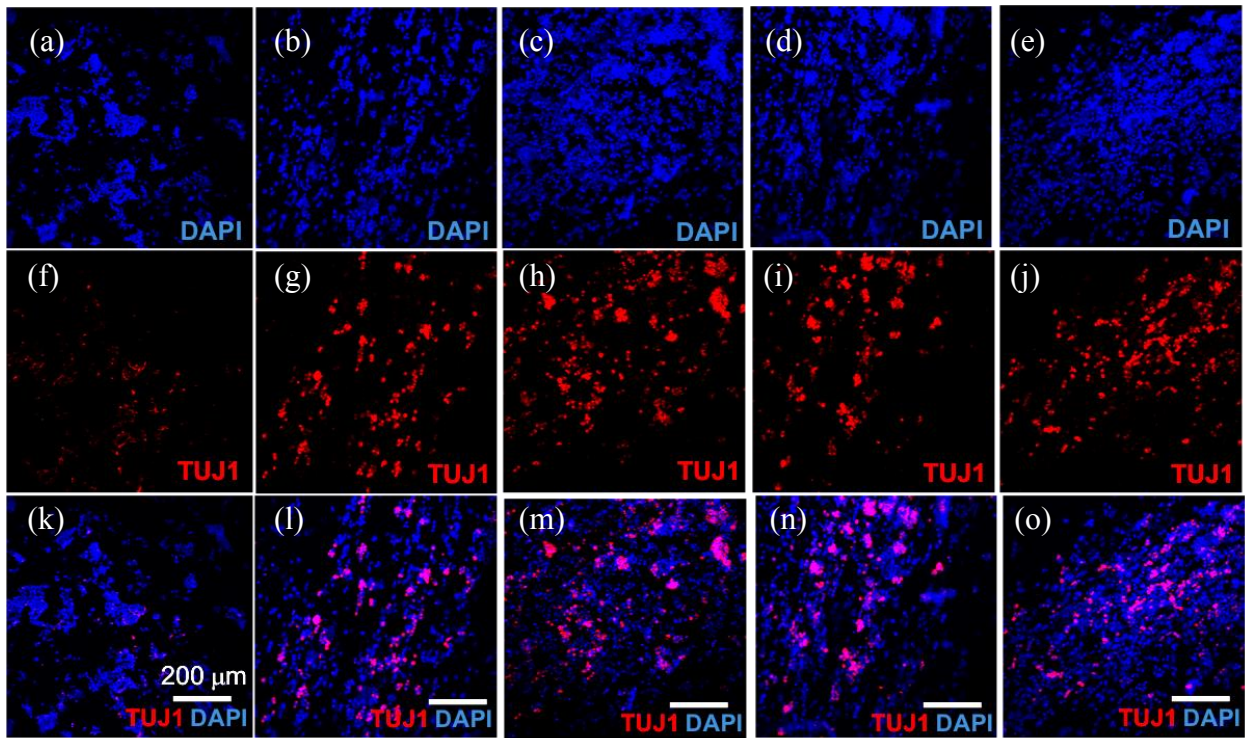
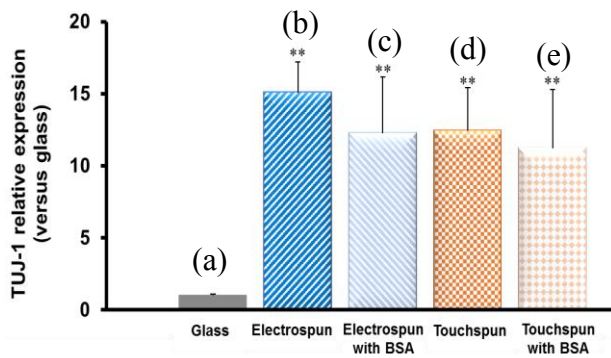
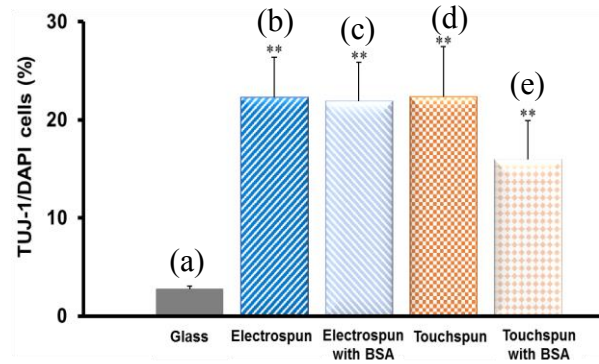
**Figure 2.4.** Contact angle of PCL film when compared to glass. Data are mean  $\pm$  standard error of the mean; N=4.



**Figure 2.5.** Neural stem cell adhesion on various substrates after 4 hours of culture. Data are mean  $\pm$  standard error of the mean; N=9, \*p<0.05 when compared to glass.



**Figure 2.6.** Enhanced neural stem cell proliferation on glass (**a, f, k**), electrospun fibers (**b, g, l**), electrospun fibers with BSA (**c, h, m**), touchspun fibers (**d, i, n**), touchspun fibers with BSA (**e, j, o**) after 7 days of culture. Data are mean  $\pm$  standard error of the mean, N=9; \*p<0.05 when compared to glass at day 1, \*\*\*p<0.001 when compared to glass at day 7.

**A****B****C**

**Figure 2.7.** Immunocytochemical staining of TUJ1 (red) and DAPI (blue) on: (A: a, f, k) glass, (A: b, g, l) electrospun fibers, (A: c, h, m) electrospun fibers with BSA, (A: d, i, n) touchspun fibers and (A: e, j, o) touchspun fibers with BSA after 4 days. Relative TUJ1 expression levels on: (B-a) glass, (B-b) electrospun fibers, (B-c) electrospun fibers with BSA, (B-d) touchspun fibers

and **(B-e)** touchspun fibers with BSA after 4 days were determined by ImageJ software. Quantification of percentage of TUJ-1 cells on: **(C-a)** glass, **(C-b)** electrospun fibers, **(C-c)** electrospun fibers with BSA, **(C-d)** touchspun fibers and **(C-e)** touchspun fibers with BSA at day 4. Data are mean  $\pm$  standard error of the mean, N=6; \*\*p<0.01 when compared to glass. Scale bar = 200  $\mu$ m.

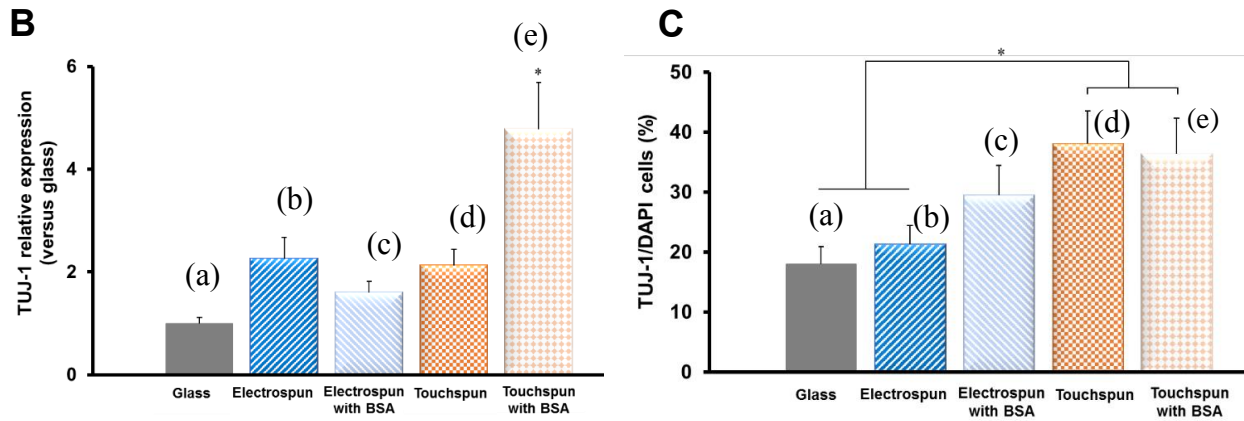
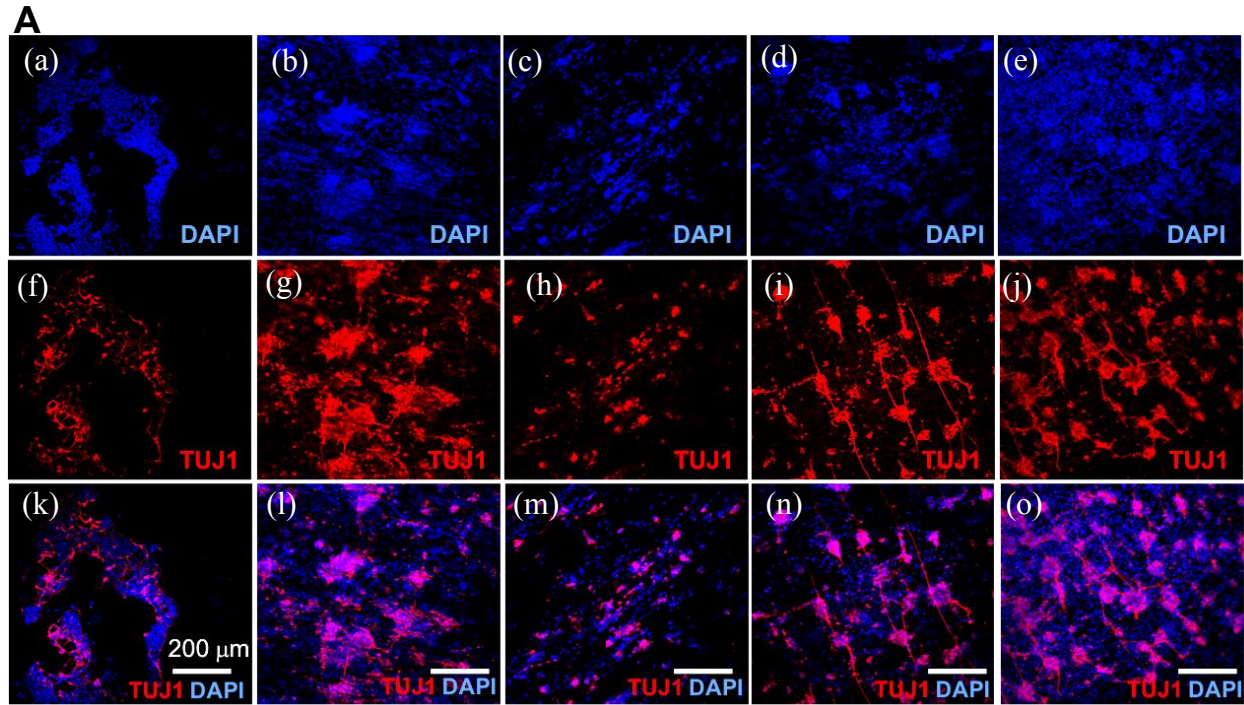


**Figure 2.8.** Immunocytochemical staining of TUJ1 (red) and DAPI (blue) on (A: a, f, k) glass, (A: b, g, l) electrospun fibers, (A: c, h, m) electrospun fibers with BSA, (A: d, i, n) touchspun fibers and (A: e, j, o) touchspun fibers with BSA after 8 days. Relative TUJ1 expression levels on: (B-a) glass, (B-b) electrospun fibers, (B-c) electrospun fibers with BSA, (B-d) touchspun fibers and (B-e) touchspun fibers with BSA after 8 days were determined by ImageJ software. Quantification of percentage of TUJ1 cells on: (C-a) glass, (C-b) electrospun fibers, (C-c)

electrospun fibers with BSA, **(C-d)** touchspun fibers and **(C-e)** touchspun fibers with BSA at day

8. Data are mean  $\pm$  standard error of the mean, N=6; \*p<0.05. Scale bar = 200  $\mu$ m.

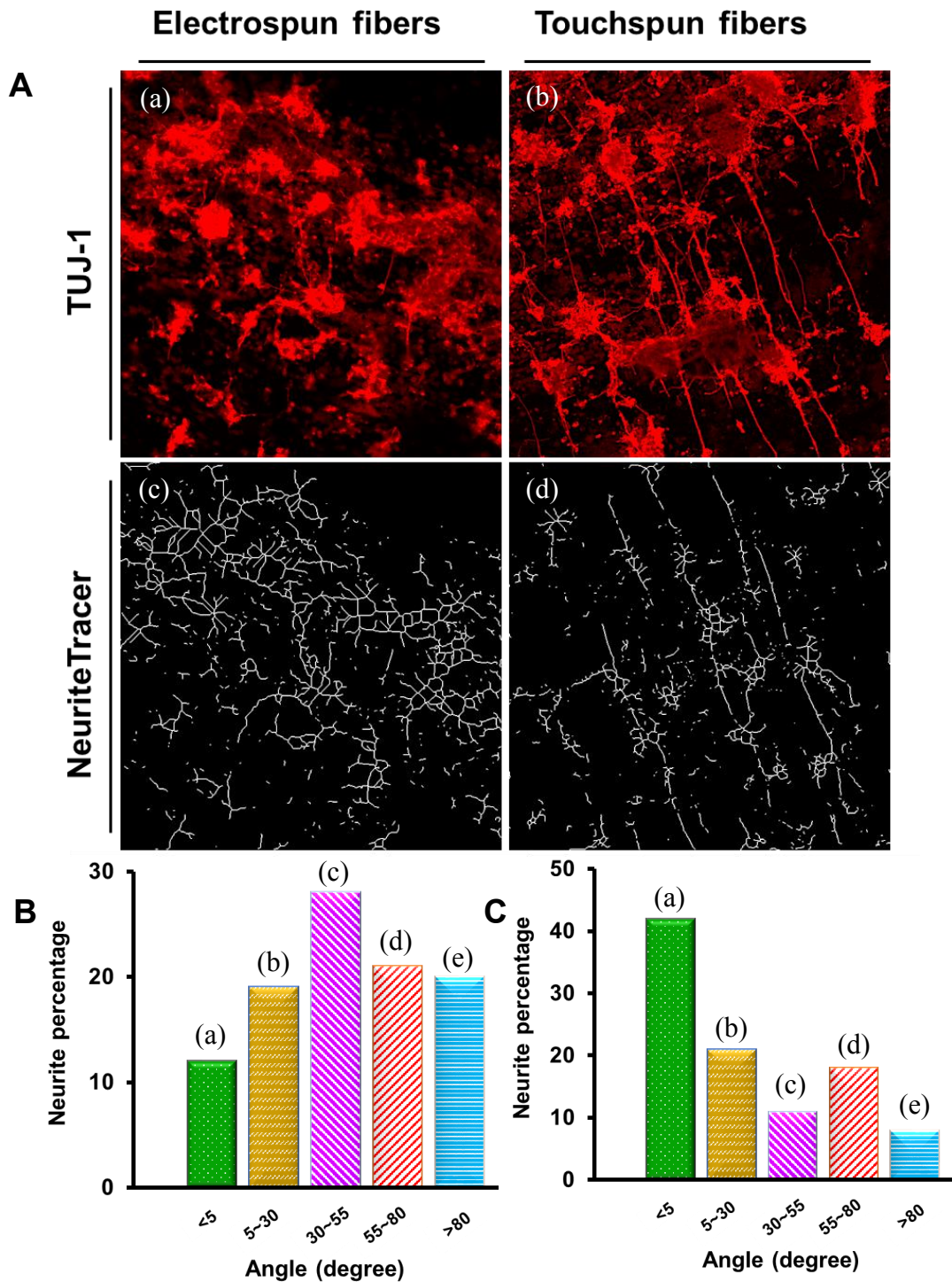


**Figure 2.9.** Confocal micrographs of (A) NSC growth and spreading on PCL nanofibers. Cells were stained with TUJ1 (red) as shown on (A-a) for electrospun fibers and (A-b) for touchspun

fibers. The associated neurite outgrowth was traced automatically by NeuriteTracer Plug-in as shown on (A-c) for electrospun fibers and (A-d) for touchspun fibers. The neurite angle distribution on the corresponding electrospun PCL fibers (B) and touchspun fibers (C). The angles between electrospun fibers and neurites have been shown on: (B: a, b, c, d, e) for angles of  $<5^\circ$ ,  $5^\circ\sim 30^\circ$ ,  $30^\circ\sim 55^\circ$ ,  $55^\circ\sim 80^\circ$ ,  $>80^\circ$ . Also, the angles between touchspun fibers and neurites have been shown on: (C: a, b, c, d, e) for angles of  $<5^\circ$ ,  $5^\circ\sim 30^\circ$ ,  $30^\circ\sim 55^\circ$ ,  $55^\circ\sim 80^\circ$ ,  $>80^\circ$ . N=6.

## CHAPTER 3

# ENHANCED ALIGNMENT OF THE NEURAL STEM CELLS ON THE TOUCH-SPUN NANOFIBROUS SCAFFOLDS <sup>2</sup>

---

<sup>2</sup> D. Asheghali, S.-J. Lee, A. Furchner, S. Larson, A. Tokarev, A. Gruzd, S. Stake, K. Hinrichs, L. G. Zhang, S. Minko.  
To be submitted to ACS Nano.

### 3.1 Abstract

Touchspinning is a simple and scalable method for the fabrication of nano- and microfibers from polymer solutions or melts. This technique does not depend on the dielectric properties of polymer solutions and has shown advantages over the common fiber spinning techniques, such as electrospinning and microfluidic spinning. The touchspinning setup consists of a spinneret, a motor, and a syringe pump. A set of rods is perpendicularly attached to the spinneret. As the spinneret rotates, the rods touch the polymer droplet and the fiber is formed when the rod is pulled away. In this study, the aligned touchspun polycaprolactone (PCL) nanofibers were fabricated at different spinning rates, and the proliferation potential of the neural stem cells (NSCs) was analyzed on these nanofibrous scaffolds. The aligned electrospun PCL nanofibers were fabricated at spinning rates similar to the touchspun nanofibers and they were served as a control group. The structural characteristics of the PCL nanofibers were analyzed by X-ray diffraction (XRD). The degree of crystallinity of the touchspun fibers was greater than that of electrospun fibers at various spinning rates. Also, the Young's modulus values of the touchspun fibers at various spinning rates were much higher (>600%) than those of electrospun fibers. NSCs exhibited an elongated neurite growth along the touchspun PCL nanofibers at varying spinning rates, whereas, NSCs tended to aggregate on the entangled electrospun PCL nanofibers. As the spinning rate of the touchspun nanofibers increased, the percentage of neuronal cells generated from NSCs increased. These results have shown the feasibility of using the touchspinning technique to fabricate fibrous scaffolds for neural tissue engineering applications.

### 3.2 Introduction

Fibers and nanofibers are playing a growing role in various applications ranging from the design of new composite materials to the fabrication of tissue engineering scaffolds for artificial bones and organs. There are many challenges for the nerve gap reconstruction using autografts and allografts. These challenges include loss of function at the donor site, limited body supply, and formation of neuromas.<sup>56</sup> Due to their high porosity, large surface area, nanoscale dimension and adjustable fiber diameter, nanofibrous scaffolds have attracted considerable attention for tissue engineering applications, including nerve damage repair.<sup>62</sup> Additionally, the comparable morphology of nanofibers to the natural extracellular matrix helps make these nanostructures suitable for tissue engineering and drug delivery applications.

The technique of electrospinning has been used extensively to create 2D and 3D scaffolds for biomedical applications.<sup>117-118</sup> In electrospinning, the polymer solution is pushed through a syringe and the pendent polymer droplet is charged via exposure to a high voltage (~20 kV) so the droplet becomes charged. The droplet stretches once the electrostatic repulsion counteracts the surface tension of the polymer droplet. When the electrostatic repulsion overcomes the surface tension, the polymer droplet ejects from the tip of the needle. As the droplet stretches and the solvent evaporates, the diameter of the fiber decreases. This technique is very well studied; however, it is extremely dependent on the dielectric properties of the polymer solution. Moreover, several reports have shown that the applied high-voltage in electrospinning has negative effects on the loaded biomolecules, such as bovine serum albumin (BSA) and heparin.<sup>43-45</sup> Touchspinning is a new technique that is absolutely independent of the dielectric properties of the polymer solution.<sup>53</sup> In this simple and controllable process, a rotating rod (or a set of rods) is glued to a spinneret. The polymer solution is pushed through a syringe forming a droplet at the tip of a needle.

The distance between the polymer droplet and the tip of the rod on the spinneret is adjusted so that the rod contacts the polymer droplet as the spinneret rotates. Following the initial “touch”, the polymer droplet forms a liquid bridge. As the spinneret rotates, the liquid bridge stretches and the fiber length increases with the diameter decreasing due to mass conservation. The surface area of the liquid thread increases with its elongation and thus generates a larger surface area for eventual solvent evaporation from the thread. The fibers can easily be collected on the coverslip or any object held at the center of the spinneret for further biological studies.<sup>53</sup> A key advantage of the touch-spinning process is its ability to generate fibers with a uniform diameter. During drawing, the fiber stretches via two distinct mechanisms: 1) axial stretching due to the rotation of the stage, and 2) capillary forces, which acts to drain fluid from the fiber back into the source droplet. In addition, the surface tension will act to smooth out any axial variations in radius during the drawing stage (which typically occurs on a millisecond timescale). Hence, uniform thinning is expected for the bulk of the fiber. Due to the uniform nature of the fiber shape during the drawing (stretching) step before fracture, the fiber will also continue to thin uniformly during the evaporation stage. Thus, both the drawing and the evaporation steps ensure that uniform fibers are generated.<sup>53</sup>

In touchspinning, spinning rate, flow rate of the polymer solution, and concentration of the solution can control the diameter of the fiber. The fibers can be collected unidirectionally, orthogonally, and randomly oriented with density controlled 2D- and 3D-meshes. These fibers can be spun around a glass coverslip for further biological studies. Touchspinning offers opportunities beyond 3D-printing due to the controllable fiber diameter and a several orders of magnitude greater speed of scaffold fabrication.

Stem cells, with their great potency properties, offer promising therapies to treat neurodegenerative diseases and traumatic injuries.<sup>119</sup> Neural stem cells respond to both

biochemical and biophysical cues while maintaining their functional tissue architecture and intercellular network. For example, the development of complex neural circuitry requires appropriate induction of growth factors such as retinoic acid. Biophysical cues such as substrate elasticity and alignment play key roles in regulating neurocellular functions in a series of intracellular mechanotransductive processes.<sup>119-122</sup> For instance, aligned nanofibers are supposed to guide the extension of the regenerated neurites from the proximal stump to the distal stump through biophysical cues. Additionally, it is well documented that softer substrates enhance neuronal differentiation. In this study, the proliferative capability and differentiation potential of neural stem cells was investigated on the touchspun scaffolds fabricated at different spinning rates *in vitro*. More importantly, we will investigate how varying fabrication speed can affect mechanical and chemical properties of touchspun fibers, which can consequently govern the fate of neural stem cells.

### 3.3 Experimental Section

#### **3.3.1 Polymer Solution Preparation**

PCL ( $M_n = 80,000 \text{ g.mol}^{-1}$ ) (Aldrich) was dissolved in chloroform (ACS grade, BDH, VWR) for 1 h at  $60^\circ \text{ C}$  to produce solutions with concentration of 8 wt%.

#### **3.3.2 Touchspun and Electrospun Nanofiber Preparation**

The touchspun samples were prepared at 500 RPM, 1400 RPM, and 2000 RPM. The polymer solution was pushed by an automated pump (Razel Scientific Instruments, variable speed syringe pump, model R99-E) through a syringe (Hamilton<sup>TM</sup> 1000 series gastight<sup>TM</sup> syringe, 1 mL) at a flow rate of  $10 \mu\text{L.min}^{-1}$ . The fibers were spun at room temperature.

The electrospun samples were prepared utilizing an electrospinning setup (Spraybase®) with a rotating drum collector (Profector Life Sciences Ltd.) with the rotation speed of 500 RPM, 1400 RPM, and 2000 RPM. The polymer solution was pushed through a syringe (Hamilton™ 1000 series gastight™ syringe, 1 mL) at a flow rate of 10  $\mu\text{L}\cdot\text{min}^{-1}$ . The needle (i.d.=0.9 mm) was connected to the voltage of 20 kV and the working distance was 110 mm. The fibers were spun at room temperature.

The fiber samples were prepared for the mechanical tests on the rectangular frames with the size of 10 cm  $\times$  30 cm. Five electrospun and five touchspun samples were prepared to find the average Young's modulus values for each spinning method.

### **3.3.3 Fiber Characterization**

A FEI Teneo Scanning electron microscope (SEM) was employed to assess morphology and channel size of prepared touchspun and electrospun fibers with varying RPM. All samples were sputter coated with iridium for 30 seconds at a coating rate of 0.1 nm/s prior to the imaging. The crystal structures of the samples were characterized by X-ray diffraction (XRD) instrument (PANalytical X'Pert PRO MRD). The XRD scans were recorded with a Cu  $K\alpha_1$  radiation ( $\lambda = 1.541 \text{ \AA}$ ) in the  $2\theta$  range from  $15^\circ$ – $35^\circ$  with a step size of  $0.03^\circ$ .

In addition, Differential Scanning Calorimeter (DSC), TA Instrument DSC SW 9.01, was used to determine the %crystallinity of the touchspun and electrospun fibers. Samples were heated from  $-70^\circ\text{C}$  to  $120^\circ\text{C}$  at a scanning rate of  $10^\circ\text{C}/\text{min}$  under a nitrogen atmosphere.

Swelling investigations were performed with infrared-spectroscopic ellipsometry (IR-SE) on the touchspun and electrospun fibers with a diameter of 180 nm, as well as on a thin PCL film that served as a control sample. All samples were prepared on IR-transparent silicon wedges. The PCL film was spin-coated from a solution of 0.4% PCL in chloroform. Employing a specially

designed flow cell in a custom-built IR ellipsometer<sup>123</sup>, *in situ* IR-SE was used to monitor the PCL films and fibers in ultrapure water (Millipore Direct-Q® 3 UV) at room temperature under no-flow conditions every other day over a period of 14 days. All measurements were referenced to spectra of a clean substrate obtained under the same experimental conditions.

### 3.3.4 Evaluation of the Mechanical Behavior

An electromechanical universal test system (MTS Criterion® Model 42) conducted tensile mechanical testing of various PCL nanofibers under a constant crosshead rate of 2 mm.min<sup>-1</sup>. All scaffolds were trimmed into 14 mm × 18 mm rectangular sheets and they were clasped on each end by mechanical grips. Young's modulus was calculated by dividing the force on the fiber by the effective cross-sectional area of the fiber, A. The effective cross-sectional area, A, was determined using

$$A = \frac{W}{(L \times PD)}$$

where W represents weight of the fiber, L, the length of the fiber, and PD, the density of PCL (1.145 g.mL<sup>-1</sup>).

### 3.3.5 Culture of NE-4C Neural the Cells on Scaffolds

NSCs (NE-4C, ATCC) were utilized to evaluate cell responses on various printed nerve scaffolds. NSCs were cultured in Eagle's Minimum Essential Medium (ATCC), 5% fetal bovine serum (FBS) (ATCC) and 1% L-glutamine (Sigma-Aldrich). Cells were cultured in a 150-cm<sup>2</sup> flask under a humidified atmosphere with 5% CO<sub>2</sub> at 37 °C. The culture medium was changed every two days. The prepared scaffolds were punched into small circle samples with a diameter of 10 mm. The samples were then sterilized by 70% ethanol for 30 minutes, rinsed and immersed in phosphate buffered saline (PBS) overnight. Before seeding the cells, the scaffolds were pre-wetted in control media at 37 °C before seeding cells. NSCs were seeded at a density of 50,000 per

scaffold for a week followed by a two-week neural differentiation. After each prescribed time interval, scaffolds were transferred to new well-plates and prepared for immunocytochemistry.

### **3.3.6 Immunocytochemistry of NSCs on the Scaffolds**

For differentiation studies, NSCs were cultured in the respective standard medium with  $10^{-6}$  M *all trans* retinoic acid (RA) on the electrospun fibers and touchspun fibers for up to 14 days. After each culture period, samples were rinsed with PBS and fixed with 10% formalin for 12 minutes at room temperature for the specified time. The cells were further parabolized with 0.2% Triton X-100 in PBS for 5 minutes. Diluted primary antibodies, mouse anti-TuJ1 (1:1,000; Covance) and rabbit anti-GFAP (1:1000; Abcam) were gently added in scaffolds and incubated at 4 °C in a moist environment overnight. This was followed by the secondary antibodies incubation with Alexa Fluor 594 goat anti-mouse (Life technologies) and Alexa Fluor 647-conjugated donkey anti-rabbit IgG (Life technologies) at room temperature. The cell nuclei were stained by  $10 \mu\text{g.mL}^{-1}$  4'-6-diamidino-2-phenylindole dihydrochloride (DAPI) (Life technologies). Laser scanning confocal microscopy (LSCM 710, Zeiss) was employed to visualize and monitor the fluorescent images of 3D neural cell growth and neurite extension of cells. Neuronal cells (TUJ-1 positive) and astrocytes (GFAP-positive) expression level were quantified with the ImageJ software. Image processing for linear color level adjustments in Zeiss Zen were applied identically to all conditions.

### **3.3.7 Statistical Analysis**

All quantitative data are expressed as average  $\pm$  standard error of the mean. Numerical data were analyzed via student's t-test to determine differences among the groups. Statistical significance was considered at  $p < 0.05$ .

## 3.4 Results

### **3.4.1 Characterization of the Prepared PCL Nanofibers**

The morphologies of the touchspun and electrospun PCL nanofibers were analyzed by FEI Teneo FE-SEM. Figure 3.1 represents the aligned PCL nanofibers prepared by electrospinning (Figure 3.1:a, b, c) and touchspinning (Figure 3.1:d, e, f) methods. Both aligned PCL fibers were successfully fabricated from the 8-wt% PCL solution. The Fiji<sup>72</sup> software was used to measure the diameter of the nanofibers. The average diameter of 50 electrospun and touchspun nanofibers at different RPM values were measured and the results have been shown in Table 3.1.

MTS criterion model 42 was used to measure the elastic modulus of the PCL nanofibers with varying RPM, showing a range of 8MPa to 200MPa. Figure 3.2 and Figure 3.3 show that as RPM increases, tensile strength increases in both touchspun and electrospun fibers. Furthermore, the elastic modulus of the touchspun fibers was significantly greater than that of the electrospun fibers at 500 RPM, 1400 RPM, and 2000 RPM. For example, the elastic modulus of the touchspun fibers at 500 RPM was about 8.7-fold higher than that of electrospun fibers at 500 rpm. When the rotation speed of the collector was increased to 2000 RPM, the elastic modulus of the touchspun fibers was ~200 MPa (~7.9) fold higher than that of electrospun fibers. The Young's modulus values of the electrospun and the touchspun fibers are shown in Table 3.2. It is assumed that the greater toughness of the touchspun fibers was primarily due to the greater crystallinity within the fibers.

The crystal structures of the PCL nanofibers prepared by two separate spinning techniques, touchspinning and electrospinning, were confirmed by XRD analysis (Table 3.3) and DSC (Table 3.4). The peak positions for both electrospun and touchspun PCL fibers were essentially identical; showing two strong peaks at  $2\theta=21.5^\circ$  and  $23.9^\circ$ , respectively. This suggested no change in crystal

structure by fabrication techniques. However, the touchspun PCL fibers exhibited a much higher percentage of crystallinity compared to the electrospun PCL fibers. According to Table 3.3 and 3.4, the %crystallinity of touchspun fibers is higher than that of electrospun fibers as varying rotation speeds of the collector. The %crystallinity of both types of fibers increases as the spinning rate increases and that is due to the greater stretching of the fibers at higher rotation speeds. In Table 3.4, the degrees of crystallinity of the fibers have been shown using the first two cycles of DSC spectra. The %decrease of crystallinity from cycle 1 to cycle 2 is much higher in touchspun fibers which may prove the cold-drawing effect in the touchspinning process.

### **3.4.2 Enhanced NSC Differentiation**

Figure 3.4A and 3.4B show the early stage of the neural differentiation of NE-4C cells on the touchspun and electrospun PCL nanofibers after 7 days of culture. To trace NE-4C cells attached on different substrates, we used subclones constitutively expressing green fluorescent protein. GFP+NE-4C neural stem cells differentiated into immature neurons on all substrates, developing a dense network of neuronal processes expressing TUJ1 in response to treatment with RA. Additionally, the typical morphology of the attached NSCs were recognized. NSCs cultured on glass substrates were tightly packed and spread with limited interstitial space at the boundary of the aggregate. In contrast, cells in the PCL nanofibers with varying RPM aggregated loosely and exhibited an elongated neurite growth along the fiber. Third rows in each Figure 3.4A and 3.4B represent merged confocal microscopy images of GFP, TUJ-1 and DAPI staining.

At the beginning of the second week post-induction, morphologically mature neurons were formed (Figure 3.5). Non-neuronal glial cells (e.g. astrocytes) such as astrocytes stained by GFAP were also present on all substrate. The ImageJ software was used to determine the quantification of TUJ-1 and GFAP expression. The percentage of TUJ-1 positive cells on day 14 remained similar

across all electrospun fibers, approximately 4%, with no statistically significant variation as a function of varying RPM. In contrast, the percentage of TUJ-1 positive cells increased on touchspun fibers as RPM increased. For example, the percentage of TUJ-1 positive cells increased by 3 folds from 500 rpm to 2000 rpm on touchspun fibers. Similar percentages of GFAP positive neurons were observed across all touchspun fibers with varying RPM. However, varying RPM affects the percentage of GFAP positive cells on electrospun fibers. Specifically, the percentage of GFAP positive cells decreased by 1.6 folds from 500 RPM to 2000 RPM on electrospun fibers. Additionally, the ratio of TUJ-1 positive to GFAP positive cells was determined across all substrates. Figure 3.5E and 3.5F shows that higher RPM significantly increased the ratio of TUJ-1 to GFAP positive cells on both electrospun and touchspun fibers, respectively. However, at each RPM, the ratio of TUJ-1 positive to GFAP positive cells was not statistically different between touchspun and electrospun fibers.

### **3.4.3 Late Stage of Neural Differentiation after Two Weeks of Swelling**

As discussed, both electrospun fibers and touchspun fibers were fabricated in high alignment at different RPMs. To figure out how swollen PCL nanofibers affect the cell behavior, we allowed all fibers to be immersed in culture medium for 2 weeks before starting the cell experiment. During the two weeks of swelling, several electrospun fibers were misaligned and entangled. However, all touchspun fibers maintained their aligned morphology even after 2 weeks of swelling. Figure 3.6A shows how the entanglement of electrospun fibers can disturb neural cell growth. White dashed boxes show the disrupted neural cell growth due to the fibers entanglement. In contrast, the touchspun fibers (Figure 3.6B) at all different RPMs exhibited fine neural cell growth and spreading without any major entanglement at all RPMS.

### 3.4.4 Surface Chemistry Characterization

We used the *in situ* IR-SE<sup>123-124</sup> to assess differences in swelling of PCL fibers in the absence of cells. By means of polarized IR light, IR-SE provides access to the fibers' molecular vibrations and therefore to fiber hydration and molecular interactions, allowing one to probe properties like swelling and fiber–solvent interactions.

Figure 3.7A and 3.7B show measured *in situ* ellipsometric  $\Delta$  spectra of touchspun and electrospun PCL fibers, first in contact with air and then with purified water monitored over a two-week period. Observed PCL bands are associated with carbonyl-stretching,  $\nu(\text{C}=\text{O})$ , around  $1730\text{ cm}^{-1}$  and with various fingerprint modes below  $1500\text{ cm}^{-1}$ . Both upward- or downward-pointing PCL bands occur due to anisotropy of the samples. Spectra obtained in water are overlapped by the downward-pointing  $\text{H}_2\text{O}$ -bending vibrational band around  $1650\text{ cm}^{-1}$ .

Touchspun and electrospun fibers differ in their spectral behavior, both in dry state and in water. For the touchspun fibers, some bands exhibit minor shifts ( $< 1\text{--}2\text{ cm}^{-1}$ ) in  $\text{H}_2\text{O}$  compared to the dry state, which is expected because of the different chemical environments. Except for  $\nu(\text{C}=\text{O})$ , however, none of the touchspun PCL bands show any marked changes during the two-week exposure to water, suggesting that the fiber structure remains unaltered. The complex carbonyl-stretching band (Figure 3.7A (a)) seems to contain at least three major components at  $1739\text{ cm}^{-1}$ ,  $1730\text{ cm}^{-1}$ , and  $1724\text{ cm}^{-1}$ . The first two could be related to the amorphous and the crystalline PCL phase, respectively. The measured changes in  $\nu(\text{C}=\text{O})$  composition could thus indicate variations in fiber crystallinity.<sup>125</sup> However, this explanation is rather unlikely because similar band changes were also observed for the thin, closed PCL film. A more probable explanation is hydrogen bonding between surface-exposed  $\text{C}=\text{O}$  groups and water. Hydrogen-bond interactions would lead to a decrease of the  $1739\text{ cm}^{-1}$  component, in accordance with the

measurements. The observed changes, however, are small and only hint at weak interactions with water.

Changes in the baseline of  $\Delta$ , and in the amplitudes of fiber and water bands, are related to changes in fiber swelling.<sup>126</sup> In Figure 3.8,  $\Delta$  differences between the touchspun fibers in wet and dry state are evaluated at  $1500\text{ cm}^{-1}$ , yielding a semiquantitative marker for swelling of films that undergo moderate hydration. Almost immediately after exposure to water, the touchspun fiber sample begins to swell slightly. Optical calculations<sup>126</sup> suggest that the measured baseline shifts amount to swelling of only a few percent after 13 days.

The situation is quite different for the electrospun fibers. Figure 3.7B shows stronger variations in fiber and water band amplitudes, but also in the baseline of  $\Delta$ . These changes, especially the decrease in band amplitudes, are most pronounced during the first few hours of exposure to water, suggesting a stronger swelling of electrospun fibers compared to touchspun ones. Furthermore, the carbonyl-stretching band of electrospun fibers (Figure 3.7B (a)) shows a markedly different band composition, hinting at differences in chain alignment and crystallinity. When the dry fibers are exposed to water, the  $\nu(\text{C}=\text{O})$  band undergoes much stronger redshifts compared to the touchspun fibers, as can be explained by the presence of more hydrogen-bond interactions between fiber  $\text{C}=\text{O}$  groups and water. Those stronger interactions with water are also evidenced by shifts of several PCL fingerprint bands.

Interestingly, from the IR-SE data of electrospun fibers, it is not possible to find a similarly meaningful marker for film swelling as for the touchspun samples in Figure 3.8. The reason for this is that the spectra are not as "well-behaved" as those of the touchspun fibers. That is, there are apparently more changes in the electrospun film that cause overlapping spectral effects like baseline shifts and band alterations. It is therefore an indirect sign that, besides film swelling and

fiber–solvent interactions, there seem to be other differences within the electrospun fibers, particularly over longer exposure to water, including potential changes in fiber structure, alignment, and integrity.

Overall, IR-SE revealed small swelling effects of the touchspun PCL fiber sample. There was no evidence of changes in chain alignment and anisotropy. Small changes in the  $\nu(\text{C}=\text{O})$  band composition were found, presumably due to interactions with water. Electrospun PCL fibers were found to undergo more pronounced swelling and interactions with water. However, the measured IR-SE could not be explained by these two effects alone, suggesting additional effects such as structural changes.

### 3.5 Discussion

#### **3.5.1 A New Fiber Spinning Method for Enhanced Nerve Regeneration**

The touchspinning method used in this study has shown a great feasibility to create a highly aligned neural scaffold. For this purpose, we used an automated pump that dispensed the polymer through a syringe at  $10 \mu\text{L}\cdot\text{min}^{-1}$ . Affixed to the syringe was a needle that was placed within close proximity to the spinneret. Two rods were attached opposite to each other on the spinneret. The spinning speed of the collector was set at 500 RPM, 1400 RPM, and 2000 RPM and the collected PCL nanofibers were used to examine the alignment of the neural stem cells. The results were compared to the electrospun nanofibers which were fabricated under the exact same conditions as the touchspun nanofibers.

The physical nature of the components in the PCL nanofibers was examined using XRD. The XRD data revealed that the degree of crystallinity of the touchspun nanofibers at different RPM values was much higher than that of electrospun nanofibers. In touchspinning, the rods on

the spinneret are in contact with the pendent polymer droplet once the rods touch the droplet. The drawn fiber solidifies when the rod pulls it. The force is applied to the entire length of the fiber during the fiber formation stage and the force is sufficient to stretch the nanofibers similar to cold-drawing.<sup>102</sup> This results in greater chain alignment and crystallinity. In electrospinning, the electrical force is applied locally to the polymer droplet. This force is not uniformly applied to the entire length of the fiber because the electrical force at every point of the fiber depends on the distance of that point from the charged needle. This results in lower %crystallinity due to the instability during fiber formation.

A recent study from Liu et al. showed that Young's modulus of a human sciatic nerve in the longitudinal direction is in the range of  $41 \pm 3$  MPa.<sup>106</sup> The Young's modulus values of the touchspun fibers were  $78 \pm 18$  MPa,  $84 \pm 11$  MPa, and  $230 \pm 4$  at 500 RPM, 1400 RPM, and 2000 RPM, respectively. The Young's modulus values of the electrospun fibers were  $8 \pm 2$  MPa,  $12 \pm 2$  MPa, and  $23 \pm 11$  at 500 RPM, 1400 RPM, and 2000 RPM, respectively. According to these results, the touchspun nanofibers exhibited enhanced tensile properties compared to the electrospun nanofibers. The elasticity of the scaffold influences the cell adhesion, morphology, and intracellular signalling.<sup>127</sup>

### **3.5.2 Enhanced Alignment of the Neural Stem Cells along the Touchspun Nanofibers**

Electrospinning has been commonly used in various tissue engineering application due to its capacity to produce aligned micro- to nano-sized polymeric fibers. Many studies demonstrated a great potential in polymeric electrospun nanofibers for treating various nerve injuries.<sup>128-135</sup> However, electrospun fibers have many challenges including entanglement forming, which leads to poor cell growth and spreading. For example, Dalton et al. have obtained a result on the coiled electrospun fibers using fibroblast cells.<sup>133</sup> The study found out that the cells grow well inside and

outside of the coil-like fibers whereas the cells could not attach properly to the randomly oriented entangled fibers. This behavior can be attributed to the amorphous and hydrophobic nature of the highly entangled long-chain polymeric fibers. In this study, the effect of the swollen PCL fibers on neural stem cell behavior is being investigated. We expected that the touchspun fibers with high crystalline properties would allow for enhanced neural cell attachment and alignment compared to the electrospun fibers with lower crystallinity. The two-week swelling results (Figure 3.5A) clearly shows random clusters of TUJ1 and GFAP positive cells within the entangled electrospun fiber. In contrast, all touchspun fibers maintained a highly aligned morphology after two weeks of swelling, on which both TUJ1 and GFAP positive cells grew and spread efficiently along the direction of fiber alignment (Figure 3.5B). The high crystallinity properties of the touchspun fibers may play an important role in governing neural stem growth, spreading, and alignment during the early stage of the neural differentiation.<sup>92</sup> It is well documented that polymers with higher crystallinity result in a stiffer substrate, influencing the cytoskeletal organization and consequently cell phenotype.<sup>91, 114-116</sup> Some studies found that high crystalline or stiffer substrates were found to better support focal adhesion, spreading, proliferation, and differentiation of several stem cells.<sup>91-92</sup> Cui et al. showed that while chemical composition, hydrophobicity, and surface roughness of PCL/PGA polymers were held constant, crystallinity and rigidity of the polymer played major roles in determining the cell response.<sup>92</sup> In this study, highly crystalline and rigid PCL and PGA substrates significantly increased fibroblast growth compared to the amorphous polymer surface. Historically, crystallinity degree of the substrate is relatively poorly understood signal input for neural stem cells. Therefore, with increasing emphasis on biophysical regulation on stem cell behavior, our study has significant contribution in the field of nerve scaffold design.

The majority of NSCs differentiate into astrocytes instead of neurons in damaged lesions. This limits the use of NSCs as potential therapeutic agents for nerve injury. Our study has revealed that the touchspun fibers fabricated at higher RPM enhance the differentiation of NSCs to neurons, demonstrating possible therapeutic potential of touchspun fibrous scaffolds in neural tissue engineering applications.

### 3.6 Conclusion

In this study, we reviewed the structure and high crystallinity of touchspun PCL nanofibers. In fiber formation, the electrical force depends on the distance from the charged needle to the pendent droplet. We hypothesized that the touchspinning process resembles the cold-drawing method resulting in higher degree of crystallinity. In touchspinning, the rods on the spinneret apply a mechanical force to the pendent droplet and the force is uniformly and continuously applied to the entire length of the fiber during the fiber fabrication stage. In contrast, in electrospinning, the electrical force is being applied to a local point on the pendent droplet and the force is not uniformly applied to the points along the fiber since the electrical force depends on the distance from the charged needle. The high degree of crystallinity and high Young's modulus make the touchspun nanofibrous scaffolds a promising candidate for the nerve regeneration applications compared to the electrospun scaffolds.

### 3.7 Acknowledgements

S.-J.L. and L.G.Z. thank the financial support from March of Dimes Foundation's Gene Discovery and Translational Research Grant. D.A. thanks Dr. Yiping Zhao for access to XRD

instrument and Dr. Nataraja Sekhar Yadavalli for his helpful discussions for XRD and DSC analysis.

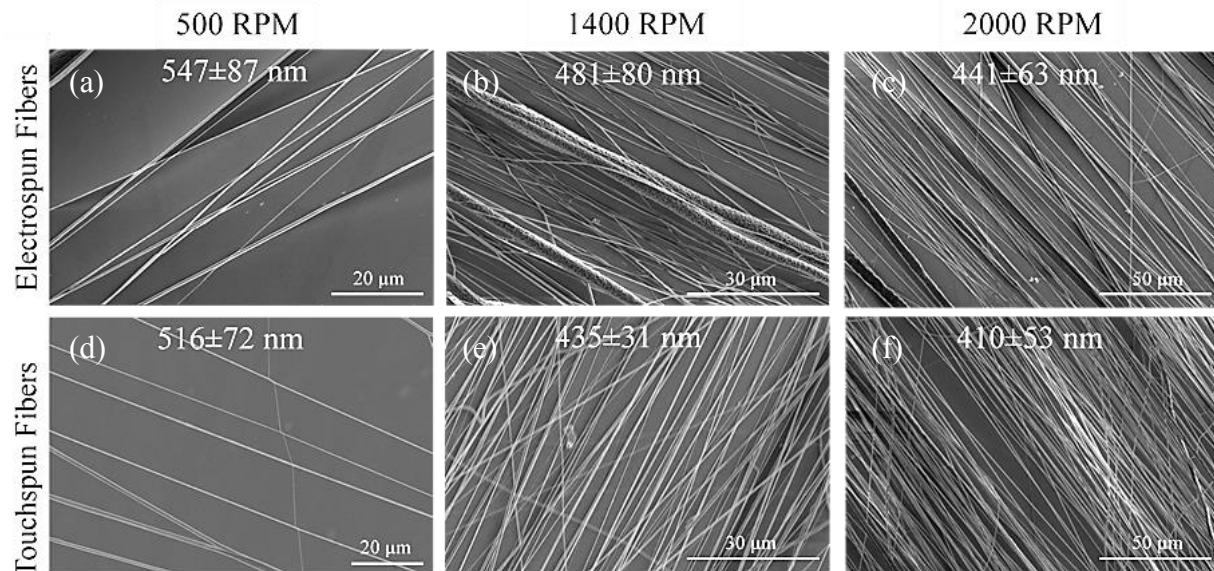


**Figure 3.1.** SEM images of nanofibers fabricated by touchspinning or electrospinning with the collector at varying rotation speeds: (a) electrospun fibers at 500 RPM with the diameter of  $547 \pm 87$  nm, (b) electrospun fibers at 1400 RPM with the diameter of  $481 \pm 80$  nm, (c) electrospun fibers at 2000 RPM with the diameter of  $441 \pm 63$  nm, (d) touchspun fibers at 500 RPM with the diameter of  $516 \pm 72$  nm, (e) touchspun fibers at 1400 RPM with the diameter of  $453 \pm 31$  nm, (f) touchspun fibers at 2000 RPM with the diameter of  $410 \pm 53$  nm.

**Table 3.1.** Average diameter of nanofibers fabricated by touchspinning or electrospinning with the collector at varying rotation speeds.

Collector Rotation Speed (RPM)	Touchspun Fibers	Electrospun Fibers
	Diameter (nm)	Diameter (nm)
500	516±72	547±87
1400	435±31	481±80
2000	410±53	441±63

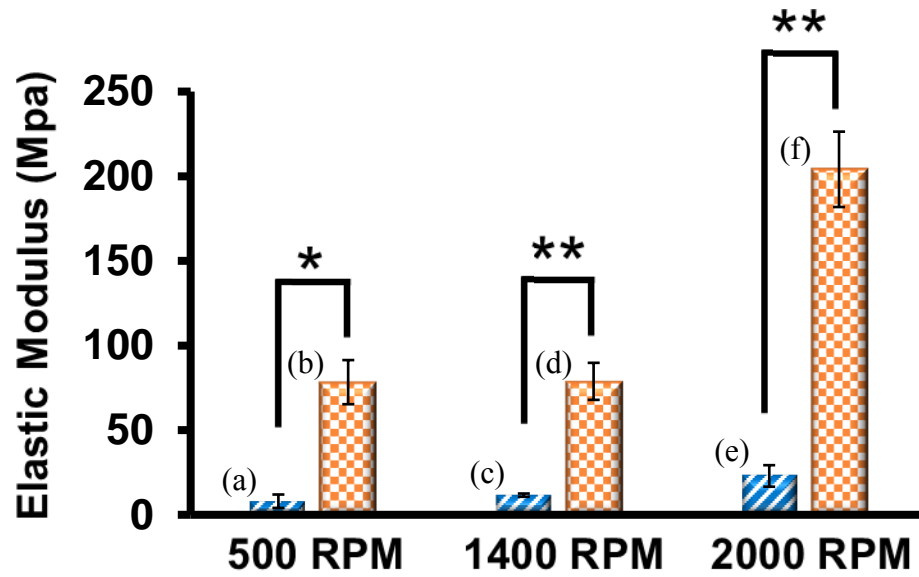


**Figure 3.2.** Elastic modulus of PCL nanofibers at varying collector speeds: **(a)** electrospun fiber at 500 RPM, **(b)** touchspun fiber at 500 RPM, **(c)** electrospun fiber at 1400 RPM, **(d)** touchspun fiber at 1400 RPM, **(e)** electrospun fiber at 2000 RPM, **(f)** touchspun fiber at 2000 RPM. N=3, \* $p < 0.05$  and \*\* $p < 0.01$  when compared to the corresponding group.

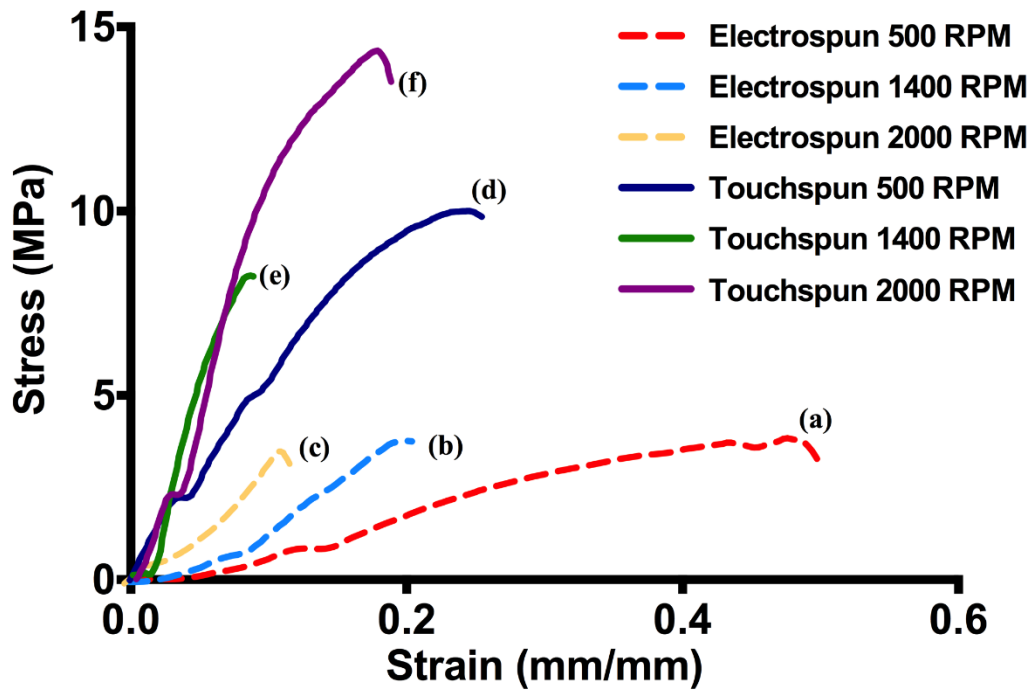


**Figure 3.3.** Elastic stress-strain behavior of both electrospun and touchspun fibers at different collector speeds: **(a)** electrospun fibers at 500 RPM, **(b)** electrospun fibers at 1400 RPM, **(c)** electrospun fibers at 2000 RPM, **(d)** touchspun fibers at 500 RPM, **(e)** touchspun fibers at 1400 RPM, **(f)** touchspun fibers at 2000 RPM.

**Table 3.2.** Young's modulus of the nanofibers fabricated by touchspinning or electrospinning at varying rotation speeds of the collector.

Collector Rotation Speed (RPM)	Touchspun Fibers	Electrospun Fibers
	Young's Modulus (MPa)	Young's Modulus (MPa)
500	78±18	8±2
1400	84±11	12±2
2000	226±4	23±11

**Table 3.3.** Percent (%) Crystallinity from XRD spectra of the nanofibers fabricated by touchspinning or electrospinning at varying rotation speeds of the collector.

Collector Rotation Speed (RPM)	Touchspun Fibers	Electrospun Fibers
	Crystallinity (%)	Crystallinity (%)
500	67	33
1400	71	51
2000	89	80

**Table 3.4.** Percent (%) Crystallinity from DSC spectra of the nanofibers fabricated by touchspinning or electrospinning at varying rotation speeds of the collector.

Collector Rotation Speed (RPM)	Touchspun Fibers			Electrospun Fibers		
	Crystallinity 1 <sup>st</sup> Cycle (%)	Crystallinity 2 <sup>nd</sup> Cycle (%)	Change of Crystallinity (%)	Crystallinity 1 <sup>st</sup> Cycle (%)	Crystallinity 2 <sup>nd</sup> Cycle (%)	Change of Crystallinity (%)
500	54	41	24	26	24	8
1400	57	47	18	45	42	7
2000	64	55	14	56	51	9

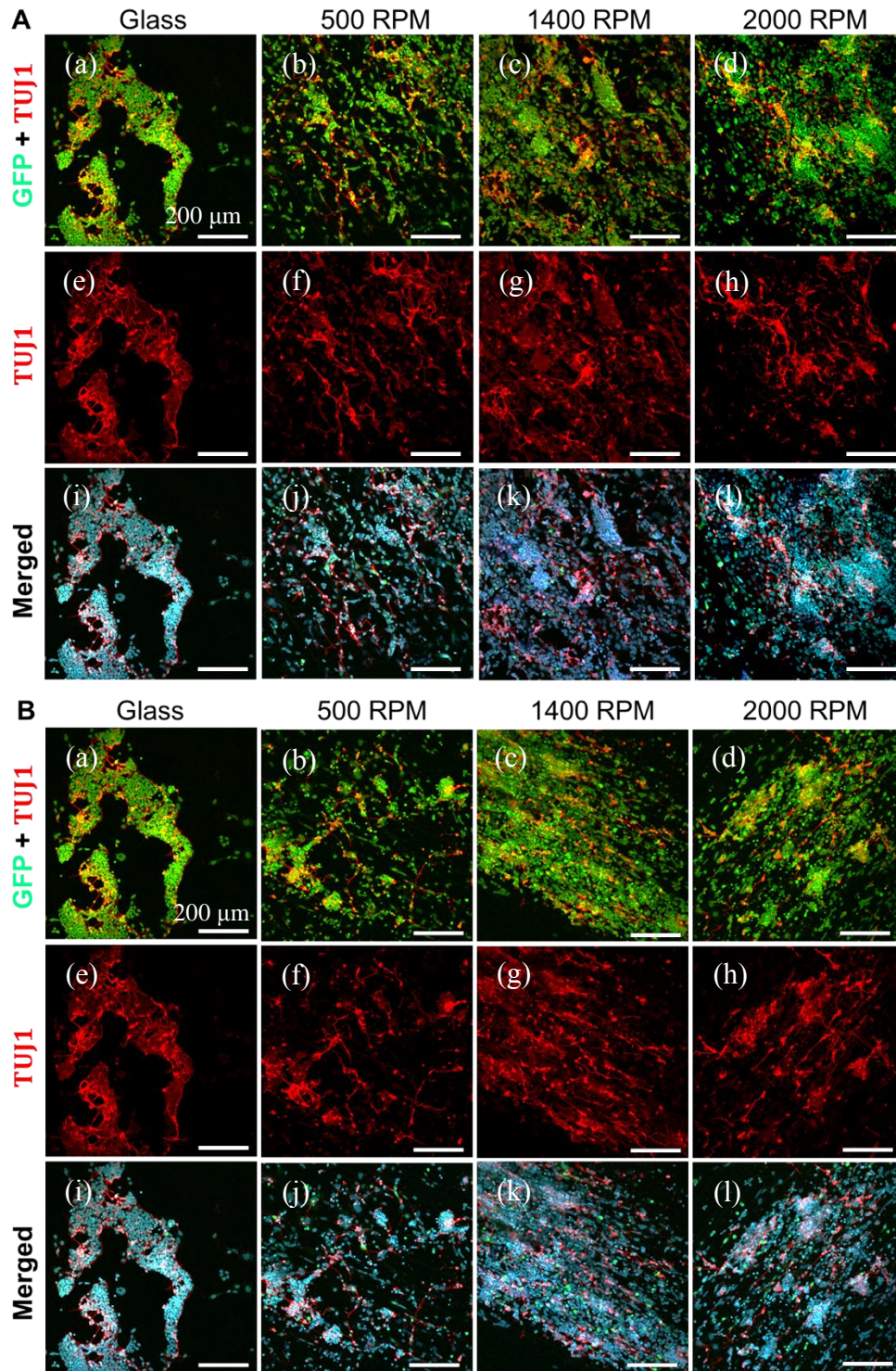


**Figure 3.4.** immunocytochemical staining of TUJ-1 (red), GFP (green) and DAPI (blue) on: (**A:** a, e, i and **B:** a, e, i) glass, (**A:** b, f, j) electrospun fibers at 500 RPM, (**B:** b, f, j) touchspun fibers

at 500 RPM, (**A: c, g, k**) electrospun fibers at 1400 RPM, (**B: c, g, k**) touchspun fibers at 1400 RPM, (**A: d, h, l**) electrospun fibers at 2000 RPM, (**B: d, h, l**) touchspun fibers at 2000 RPM on day 7, respectively. Scale bar equal to 200  $\mu\text{m}$ .

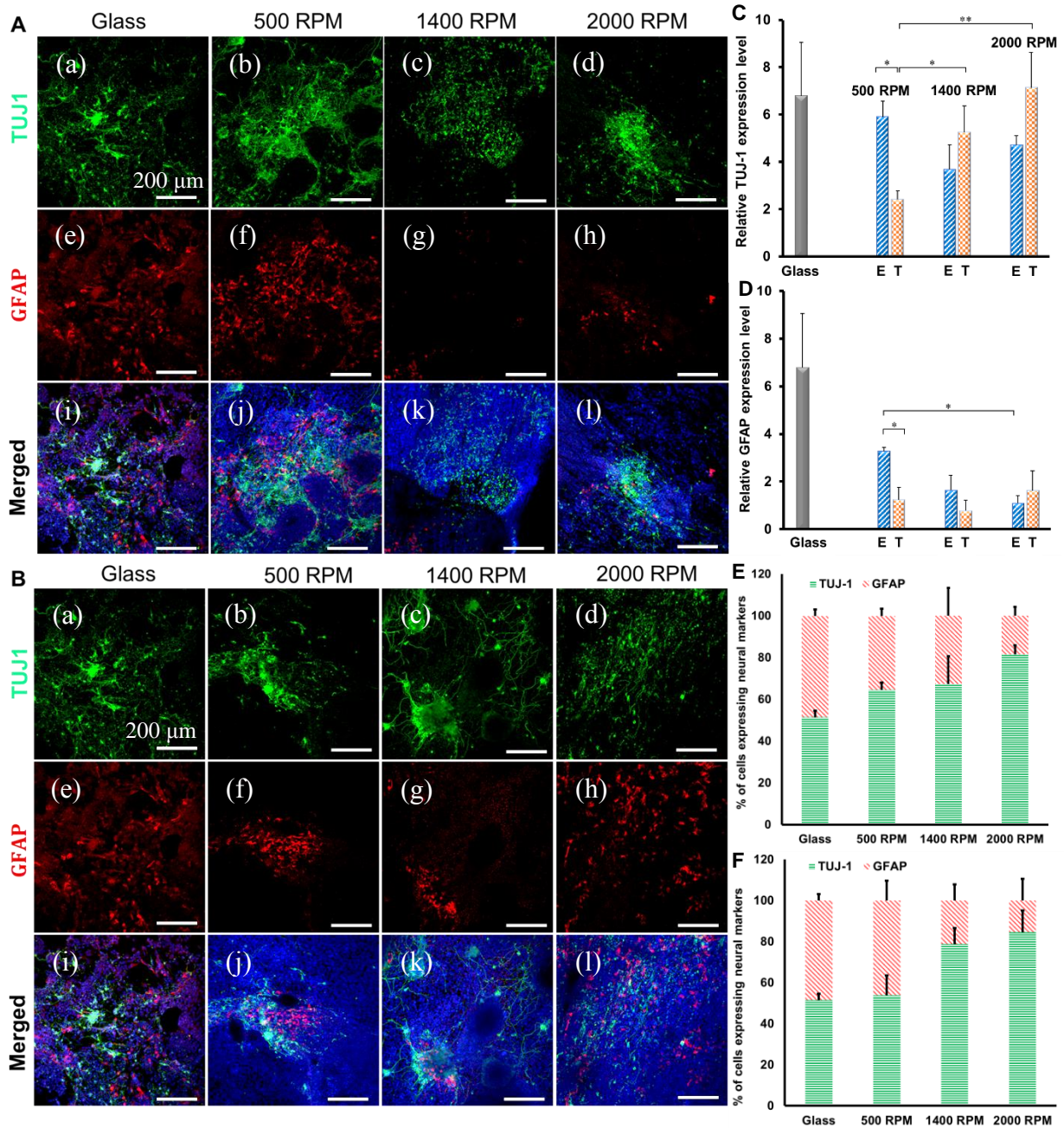


**Figure 3.5.** immunocytochemical staining of TUJ-1 (green), GFAP (red) and DAPI (blue) on: (**A: a, e, i** and **B: a, e, i**) glass, (**A: b, f, j**) electrospun fibers at 500 RPM, (**B: b, f, j**) touchspun fibers at 500 RPM, (**A: c, g, k**) electrospun fibers at 1400 RPM, (**B: c, g, k**) touchspun fibers at 1400

RPM, (**A: d, h, l**) electrospun fibers at 2000 RPM, (**B: d, h, l**) touchspun fibers at 2000 RPM after 1 week of swelling (day 14). (**C and D**) relative expression level of (**C**) TUJ-1 and (**D**) GFAP in various substrates were determined by ImageJ software. E and T stands for electrospun fibers and touchspun fibers, respectively. (**E and F**) Quantification of changes in expression of TUJ-1/GFAP ratio with changes in RPM in (**E**) electrospun fibers and (**F**) touchspun fibers. Data are mean  $\pm$  standard error of the mean, n=6; \*p<0.05 and \*\*p<0.01. Scale bar equals to 200  $\mu$ m.

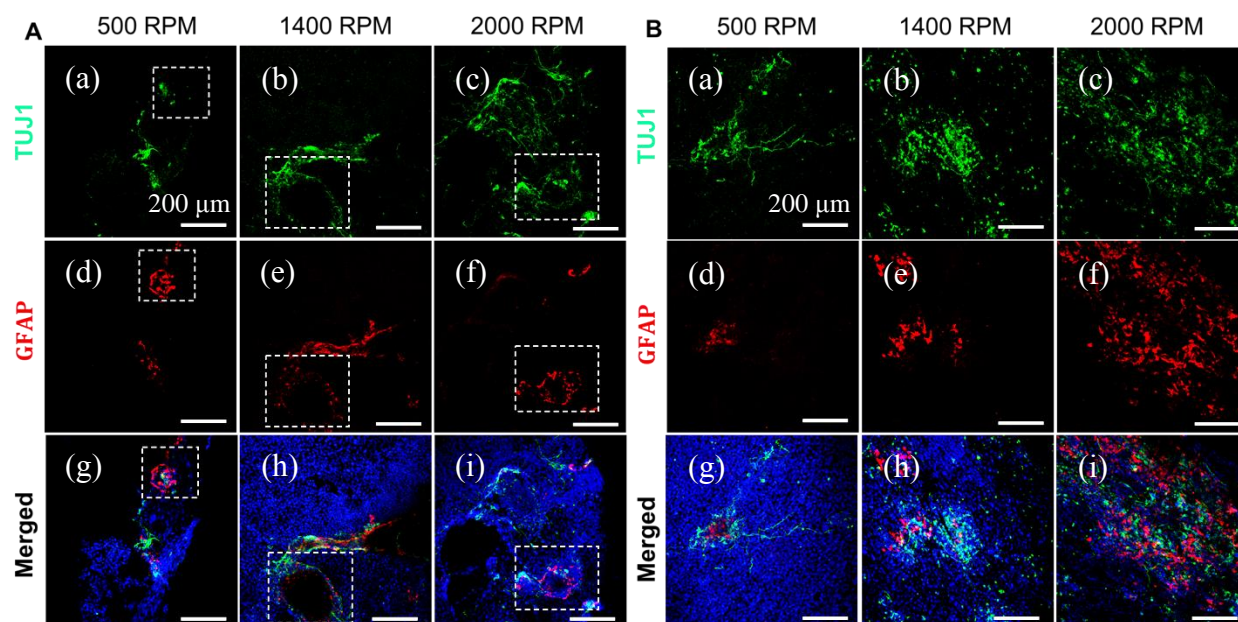


**Figure 3.6.** Representative confocal microscopy images of TUJ-1 (green), GFAP (red) and DAPI (blue) of neural stem cells cultured on: (**A: a, d, g**) electrospun fibers at 500 RPM, (**A: b, e, h**) electrospun fibers at 1400 RPM, (**A: c, f, i**) electrospun fibers at 2000 RPM, and (**B: a, d, g**) touchspun fibers at 500 RPM, (**B: b, e, h**) touchspun fibers at 1400 RPM, (**B: c, f, i**) touchspun fibers at 1400 RPM, touchspun fibers with varying RPM after 2 weeks of swelling (day 14), respectively. Scale bar equal to 200 μm.

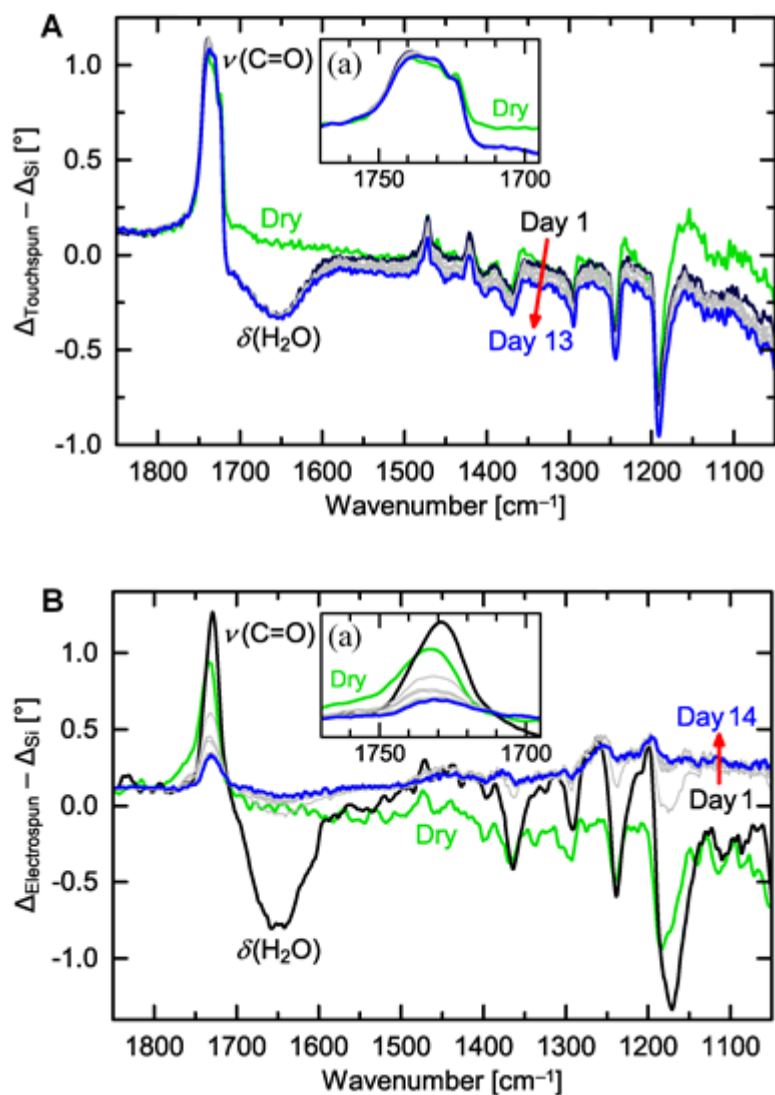


**Figure 3.7.** Ellipsometric phase-difference spectra of (A) touchspun and (B) electrospun PCL fibers measured in dry state (green) and in  $\text{H}_2\text{O}$  (black to blue) over the course of 13 (14) days. The insets (A-a) and (B-a) show changes in  $\nu(\text{C}=\text{O})$  band shape and amplitude with time for touchspun fibers and electrospun fibers, respectively.

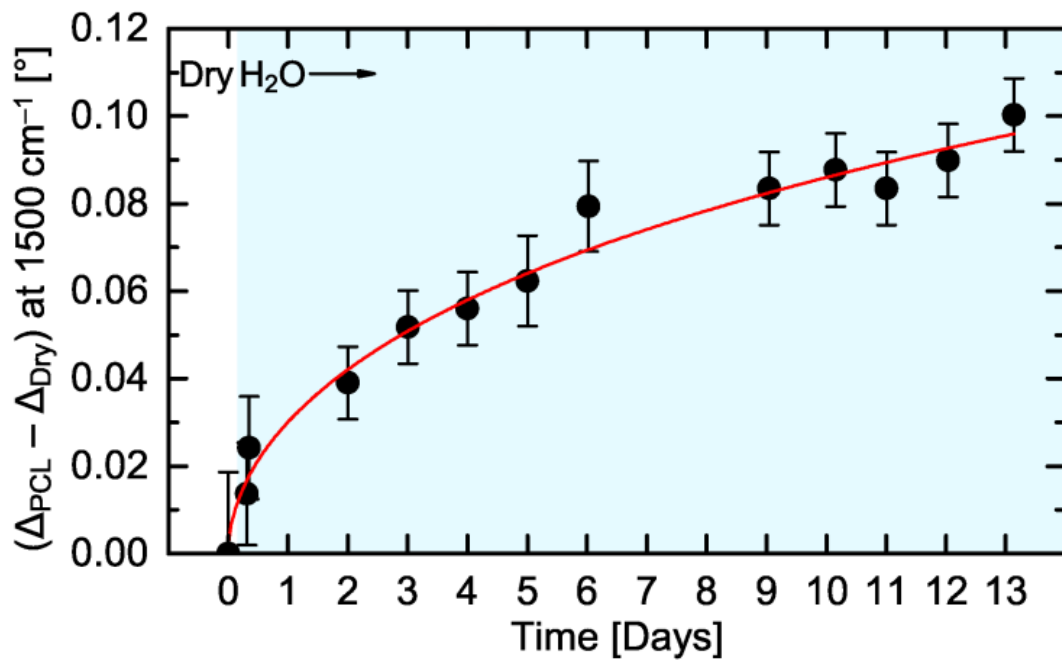


**Figure 3.8.** Swelling behavior of touchspun PCL fibers in water, as qualitatively monitored via the ellipsometric phase-difference at  $1500 \text{ cm}^{-1}$ . The red line is to guide the eye.

## CHAPTER 4

### GRAVITATIONAL DRY-SPINNING OF ULTRALONG MICRO- AND NANOFIBERS<sup>3</sup>

---

<sup>3</sup> D. Asheghali, I. M. Griffiths, A. Tokarev, , H. M. Luong, N. S. Yadavalli, W. Zhang, H. A. Stone, T. Nguyen, S. Minko. To be submitted to Advanced Materials.

## 4.1 Abstract

The long single nanofibers have attracted lots of attentions in the fields of photonics, tissue-engineering, microfluidics, and flexible electronics. However, very limited approaches have been studied for the fabrication of one-by-one single micro- and nanofibers with efficient manufacturing productivity. Our novel gravitational-spinning is a simple modification of dry-spinning technique and it is capable of producing ultralong nanofibers (fibers longer than 3 meters in the size of 50 nm per droplet of the polymer solution). The fibers can precisely be located on the substrates for various applications such as flexible electronics and tissue regeneration. In this work, the effect of surface tension, viscosity, and evaporation rate of polymer solutions on the diameter of the fibers will be studied. Furthermore, some of the applications of the gravitational-spun fibers will be discussed.

## 4.2 Introduction

There are many applications for the long free-standing single fibers in microfluidics, flexible electronics, biotechnology, and tissue engineering.<sup>2, 136-139</sup> Ultralong fibers are efficient for large-sized flexible electronics.<sup>140</sup> Embedded carbon nanotubes (CNTs) in single fibers show an enhanced conductivity of the network as the diameter of the fibers decreases and this is due to better orientation of CNTs in thinner fibers and lower contact resistance.<sup>140</sup> New fiber spinning techniques with great manufacturing productivity are required for controlled fabrication of uniform, long, and free standing single micro- and nanofibers, and precise position control of the single fibers on the substrate. Furthermore, the new techniques need to be capable of creating 2D- and 3D- fibrous constructs using unlimited material choices.

Very limited approaches have been demonstrated for the fabrication of one-by-one single fibers in the micron or nano scale.<sup>141-143</sup> Pulling or extruding are common methods to produce fibers with thickness above microns, therefore, the solutions used in these methods are required to be viscoelastic to undergo deformations and also cohesive to endure the stress during pulling. For sub-micron single fibers, usually mass production is applied followed by separation techniques like dissolving in solvents. The productivity is very low in these methods, separation of single micro- or nanofibers is very challenging, and the produced fibers show a wide range of diameter distribution after the separation step.<sup>144</sup>

Ondarcuhu and Joachim demonstrated fabrication of single nanofibers over microns using a procedure similar to dry spinning.<sup>144</sup> According to their method, a dispersion of colloidal gold particles was used instead of long polymer chains to avoid entanglements and reduce the size of the pulled fibers. This can decrease the mechanical strength of the pulled fibers. A micropipette was withdrawn from the liquid during solvent evaporation, at the solidification threshold, and

moved away at the approximate speed of  $100 \mu\text{m}\cdot\text{s}^{-1}$  to draw a single nanofiber. In the pulled single nanofibers were in the range of 2 nm to 100 nm over the length of 10  $\mu\text{m}$  to 1 mm.<sup>144</sup> Furthermore, the optimal drawing conditions depend on the evaporation rate and solidification of the solution. The droplet of the source material can be used repeatedly for drawing fibers, however, as the solvent evaporates over time, the viscosity increases, and it may not be suitable for drawing nanofibers anymore. At the beginning of the evaporation, the solution at the edge of the droplet is still fluid and the liquid bridge breaks by capillary Rayleigh instability. Once evaporation starts and the solution tend to solidify, pulling fibers becomes possible. In the last stage of the droplet evaporation, the viscosity of the solution is too high to undergo large deformations, therefore, fibers break immediately after pulling the solution. In addition, the drawing speed of  $100 \mu\text{m}\cdot\text{s}^{-1}$  is too low to satisfy the need for large scale manufacturing and there are limited choices of “ink” materials.<sup>144</sup>

In another work, Suryavanshi et al demonstrated a simultaneous growth and winding process for fabrication of long micro- and nanofibers.<sup>139</sup> In this study, a glass micropipette filled with ionic solution was held close to the substrate so a liquid meniscus was formed between the micropipette tip and substrate. Then, the pipette pulled away the solution at the speed of  $5 \mu\text{m}\cdot\text{s}^{-1}$  to  $1 \text{mm}\cdot\text{s}^{-1}$  and due to the evaporation of solvent, the fiber was grown along with the nucleation and precipitation of solute material inside the meniscus. In this technique, the diameter of the nanofiber is limited to the size of the tip of the micropipette ( $\sim 200 \text{nm}$ ), however, the drawing speed ( $1 \text{mm}\cdot\text{s}^{-1}$ ) is too low to satisfy the need for large scale manufacturing.<sup>139</sup>

Huang et al reported a simple hand-writing process to align carbon nanotubes inside a half-meter long polyethylene oxide (PEO) fiber with the diameter distribution of 300 nm to several micrometers for flexible electronic devices.<sup>140</sup> Generally, the PEO solution was used as the ink,

and single fibers were stretched from the pen tip. The fibers could be precisely located on the surface after drying. The diameter of the fiber could be tuned by concentration of the polymer solution and drawing speed. However, the drawing speed was  $10 \text{ cm}\cdot\text{s}^{-1}$  which is not efficient for scale-up production.<sup>140</sup>

There are many challenges in preparation of single free-standing nanofibers. The previous studies have demonstrated the generation of randomly packed micro- and nanofibers. In one of those studies, Zhang et al produced nonwoven fibers in the range of 200 nm to 5  $\mu\text{m}$  through solution (air-) blowing similar to the conventional melt (air-) blowing fibers.<sup>145</sup> According to their method, a solution of polyvinylpyrrolidone (PVP) was extruded from the orifices of a die assembly to form filament strands. The compressed air flow at room temperature was streaming from the top and bottom of the die nose-piece to attenuate the solution jets, evaporate solvent, and draw the filaments into thinner fibers. A collector was placed in the bottom of the drying chamber to collect the produced fibers. The fibers were highly entangled due to the turbulence in the air flow, and fibers were randomly packed in different sizes on the collector. Only the solution of PVP 12 wt% in ethanol/water (50:50, wt/wt) was efficient for this study. Solutions at a lower viscosity resulted in droplets instead of fibers and solutions at a higher viscosity solidified partially before drawing fibers. The optimal conditions were using polymer solution of 12 wt%, air processing pressure of 15 psi, and solution pressure of 70 psi. Any parameters out of these ranges resulted in random larger fiber (15–50  $\mu\text{m}$ ) or beads, and the productivity was reduced significantly since some of the fibers flew out of the drying chamber because of the turbulent air flow. In addition, free-standing single fibers could not be formed due to the turbulence.<sup>145</sup>

In order to overcome the challenges mentioned above, we proposed a simple and scalable method for forming micro- and nanofibers which is called “Gravitational Dry-Spinning”. As it is

shown in Figure 4.1, a droplet of fluid falls from a syringe located at a height  $\hat{H}$  above the ground level and as the droplet falls it draws out a thin fluid stream behind. When the droplet strikes the ground, the solvent evaporates, and the fluid solidifies to form fibers.

The following mathematical modeling is done by Prof. Ian M. Griffiths from University of Oxford, UK, regarding the experimental data collected by Darya Asheghali, University of Georgia, US:

We exploit the slenderness of the fiber as it is drawn out to obtain a reduced model in the spirit of the Trouton<sup>146</sup> equations, where we also take into account evaporation, surface tension, and gravitational effects,

$$\frac{\partial \hat{R}^2}{\partial \hat{t}} + \frac{\partial}{\partial \hat{z}} (\hat{R}^2 \hat{\omega}) = -\hat{\alpha} \hat{R}, \quad \frac{\partial}{\partial \hat{z}} (3\hat{\mu} \hat{R}^2 \frac{d\hat{\omega}}{d\hat{z}}) + \hat{\gamma} \frac{\partial \hat{R}}{\partial \hat{z}} + \hat{\rho} \hat{g} \hat{R}^2 = 0 \quad (1 \text{ a, b})$$

Here  $\hat{\omega}$  and  $\hat{R}$  are the axial velocity and cross-sectional radius of the fiber as a function of axial position  $\hat{z}$  and time  $\hat{t}$ , as illustrated in Figure 4.2. The fluid has a surface tension  $\hat{\gamma}$ , density  $\hat{\rho}$ , and viscosity  $\hat{\mu}$  (which we assume to be constant in the analysis presented below but could in principle change with, for example, cross-sectional radius  $\hat{R}$ );  $\hat{g}$  is the acceleration due to gravity and the parameter  $\hat{\alpha}$  denotes the volumetric evaporation rate per unit area of fluid surface (with units  $m.s^{-1}$ ), which we have assumed here to be dependent on the cross-sectional area exposed to the air.

To solve this system, we must apply two initial conditions,  $\hat{R}(\hat{z}, 0)$  and  $\hat{\omega}(\hat{z}, 0)$ , and three boundary conditions. We assume that no further fluid is pumped out of the syringe once a droplet is formed, while the fluid moves with the falling droplet at the other end. We also assume that the

droplet motion is unaffected by the fiber that is drawn out behind so that it undergoes freefall due to gravity, at a speed  $\hat{g}\hat{t}$ . Experimental observations indicate that the final radius of the fiber at the droplet end is unaffected by the height from which the droplet falls. Thus, we assume that the radius of the fiber at the falling droplet end remains constant throughout the process. Mathematically, these assumptions translate to the following boundary conditions:

$$\hat{\omega}(0,t) = 0, \quad \hat{R}(z_1(t),t) = \hat{R}_1, \quad \hat{\omega}(\hat{z}_1(\hat{t}),\hat{t}) = \hat{\omega}_1(\hat{t}) = \hat{g}\hat{t} \quad (2 \text{ a-c})$$

where  $\hat{R}_1$  is a constant and  $\hat{z}_1(\hat{t}) = \hat{z}_1(0) + \hat{g}\hat{t}^2/2$  denotes the position of the droplet at time  $\hat{t}$ .

To summarize, we consider a set-up described by the equations for the stretching of a viscous fiber experiencing surface-tension, gravitational and evaporative effects, as one end is drawn out at speed  $\hat{\omega}_1$  while the other end is held at a fixed position. We illustrate this schematically in Figure 4.2.

#### 4.2.1 Non-Dimensionalization

To facilitate analysis of the system we non-dimensionalize by employing the following scaling:

$$\hat{z} = \hat{H}z, \quad \hat{z}_1 = \hat{H}z_1, \quad \hat{\omega} = \hat{W}\omega, \quad \hat{R} = \hat{R}_1R, \quad \hat{t} = \frac{\hat{H}}{\hat{W}}t \quad (3)$$

where  $\hat{W}$  is a typical fluid velocity. The resulting dimensionless system is then

$$\frac{\partial}{\partial t}(R^2) + \frac{\partial}{\partial z}(R^2\omega) = -\alpha R, \quad \frac{\partial}{\partial z}(3R^2 \frac{\partial \omega}{\partial z}) + \gamma \frac{\partial R}{\partial z} + gR^2 = 0 \quad (4 \text{ a, b})$$

Subject to

$$\omega(z_1(t),t) = 0, \quad R(z_1(t),t) = 1, \quad \omega(z_1(t),t) = \omega_1(t) = Gt \quad (5 \text{ a-c})$$

where

$$\alpha = \frac{\hat{\alpha}\hat{H}}{\hat{W}}, \quad \gamma = \frac{\hat{\gamma}\hat{H}}{\hat{\mu}\hat{R}_1\hat{W}}, \quad g = \frac{\hat{\rho}\hat{g}\hat{H}^2}{\hat{\mu}\hat{W}}, \quad G = \frac{\hat{g}\hat{H}}{\hat{W}^2} \quad (6)$$

are dimensionless measures of the evaporation rate, surface tension, gravitational effects within the fiber, and drawing force. We analyze the effect of each of these parameters in turn in the following section and compare the predictions with experimental data.

#### 4.2.2 Time-Dependent Solutions

The solution to system (4) subject to (5) is found by solving (4b) at each time step to determine  $\omega$  while updating the cross-sectional radius  $R$  via an upwinding scheme for (4a). We obtain a remarkable fit to the data when we include only the effect of gravity and ignore evaporative and surface-tension effects (Figure 4.3b). Increasing the evaporative effects reduces the fiber radius as we might expect, and in a relatively uniform manner across the fiber (Figure 4.4b).

Increasing the surface tension acts to make the fiber radius more uniform across its profile (Figure 4.5b). The prediction is corroborated by experimental observations (Figure 4.5a). Increasing the gravitational force experienced by the fibre causes the fiber radius to increase nearer to the end due to the slumping of fluid towards the droplet tip and reduces the uniformity of the fiber (Figure 4.6). Increasing the acceleration of the droplet reduces the fiber radius near the syringe (Figure 4.7). Thus, to produce the most uniform fibers we would hope to minimize the rate at which the fibers are drawn, and the gravitational force experienced by the fiber, while maximizing the surface tension.

#### 4.2.3 Obtaining a Master Curve

From the results we have seen from our theoretical model that increasing the solvent evaporation rate (i.e., increasing the vapor pressure) reduces the fiber radius (Figure 4.4b) while

increasing the surface tension decreases the fiber radius when the drop height is smaller and increases the fiber radius when the drop height is larger (Figure 4.5b). Experiments in which surfactant is added to vary the surface tension while maintaining the same evaporation rate show good qualitative agreement with the theory (Figure 4.5a). However, it is difficult to vary the evaporation rate experimentally while holding the surface tension constant, with both typically varying from solvent to solvent (see Figure 4.8 and Table 4.1). The full impact of the impractical nature of isolating evaporation rate and surface tension is seen in Figure 4.8 where an increase in evaporation rate (through increasing vapor pressure) does not necessarily lead to a decrease in radius. For instance, the evaporation rate of methanol is much greater than that of water (see Table 4.1), but using methanol as solvent leads to larger radius fibers than when water is used. In this section, we examine the result of varying both evaporation rate and surface tension, in an effort to understand these features, and offer a way of presenting the fiber radius variations predicted by the theory.

In Figure 4.9, we demonstrate that, even if we increase the evaporation rate, a fiber with a larger radius can result if there is a corresponding decrease in the solvent surface tension. This is exactly the effect observed in experiments (Figure 4.8) since the surface tension of methanol is much smaller than that of water (Table 4.1). As a result, it is clear that we need to establish a method of presentation that allows us to understand how the fiber radius varies with both evaporation rate and surface tension.

We recall that three key parameters characterize the system behavior:

$$\alpha = \frac{\hat{\alpha}\hat{L}}{\hat{\omega}_0}, \quad \gamma = \frac{\hat{\gamma}\hat{L}}{\hat{\mu}\hat{R}_0\hat{\omega}_0}, \quad g = \frac{\hat{\rho}\hat{g}L^2}{\hat{\mu}\hat{\omega}_0} \quad (7)$$

which are dimensionless measures of the evaporation rate, surface tension, and gravity. From this, we see that changes in the evaporation rate are captured by variations in  $\alpha$  and changes in surface

tension are captured by variations in  $\gamma$ . Experimental observations indicate that the viscosity does not vary significantly so to begin with we seek a parametric landscape for just evaporation and surface tension. We observe a linear dependence of fiber radius on evaporation rate, while the gradient and intercept are dictated by the surface tension in the parameter landscape as shown in Figure 4.10a,b.

While viscosity variations are generally smaller, for completeness we illustrate the effect that this has by adjusting the viscosity. To capture changes in viscosity we must vary both  $\gamma$  and  $g$  appropriately. The results are shown in Figure 4.11.

## 4.3 Experimental Section

### **4.3.1 Polymer Solution Preparation**

Polycaprolactone (PCL) ( $M_n = 80,000 \text{ g}\cdot\text{mol}^{-1}$ , Aldrich) was dissolved in chloroform (ACS grade, BDH, VWR) for 1 h at 60 °C to produce solutions with concentration of 10 wt%, 13 wt%, and 16 wt%.

The polymer solutions were labeled with latex beads (Sigma, fluorescent yellow, green, and red). 50  $\mu\text{L}$  of the dye was added to 5 mL of the polymer solution.

To study the effect of surface tension, polyethylene oxide (PEO) ( $M_n = 5,000,000 \text{ g}\cdot\text{mol}^{-1}$ , Aldrich) was dissolved in deionized water for 12 hours at 60 °C to produce a solution with concentration of 2 wt%. Triton X-100 (non-ionic detergent octylphenoxypoly ethoxyethanol, Bio-Rad) was mixed with PEO solution to prepare solutions with concentration of 0.05 wt%, 0.1 wt%, and 0.5 wt% of Triton X-100.

To study the effect of evaporation rate, PEO was dissolved in anisole (ReagentPlus®, 99%, Sigma-Aldrich), deionized water, 1,4-dioxane (Certified ACS, Fisher Chemical), acetonitrile

(anhydrous, 99.8%, Alfa Aesar), and methanol (>99.8% ACS, VWR) to prepare solutions with concentration of 2 wt%.

#### **4.3.2 Polymer Solution Characterization**

A modular compact rheometer (MCR 302, Anton Paar) was used to measure the viscosity of solutions in different solvents.

The Pendent Drop<sup>73</sup> plugin in Fiji<sup>72</sup> was used to calculate the surface tension of different polymer solutions in various solvents. The contact angle analyzer with a microscope camera (AmScope) was used to analyze the pendent droplet.

#### **4.3.3 Fiber Characterization**

A FEI Teneo Scanning electron microscope (SEM) was employed to assess morphology and size of the prepared gravitational-spun fibers collected at different heights. All samples were sputter coated with gold for 20 s at a coating rate of 0.1 nm/s prior to the imaging.

#### **4.3.4 Polarization**

The polarization dependent optical transmission of straight and twisted fibers were measured by a home-built optical transmission setup. A halogen light source (Oceanoptics, HL-2000-HP) was used to generate a broadband light beam (400 – 900 nm). The light beam was then collimated and polarized by an optical polarizer (Thorlabs, LPVISE100-A) with extinction ratio > 1:1000 in the visible range. The polarization of light can be adjusted to be perpendicular or parallel to the polymer fibers. The polarized light beam was then focused to the samples by an objective lens (Olympus 10x/NA = 0.25), and the transmitted light was collected by an identical objective lens and coupled to an optical fiber. The optical fiber eventually guided the light to a spectrometer (Oceanoptics, USB4000-VIS-NIR) and the transmission spectra were recorded by Spectrasuite Oceanoptics software.

### **4.3.5 Cell Culture**

RAW264.7 murine macrophages were purchased from ATCC. RAW264.7 cells were cultured in RPMI1640 medium (Corning, USA) with 10% FBS (Corning, USA) and 1% penicillin-streptomycin (MediaTech, USA). The cell line was incubated humidly under 37°C and 5% CO<sub>2</sub>. The cells were visualized using the 488nm laser of a Zeiss LSM 710 inverted confocal microscope with a ZSMmeta head (Welwyn Garden City, UK). The images were analyzed using Image Pro Plus.

## 4.4 Results and Discussion

### **4.4.1 Gravitational Dry-Spun Ultralong Micro and Nanofibers**

To prepare the gravitational dry-spun fibers, the polymer solution was pushed by an automated pump (Razel Scientific Instruments, variable speed syringe pump, model R99-E) through a syringe (Hamilton™ 1000 series gastight™ syringe, 1 mL) at a flow rate of 100  $\mu\text{L}\cdot\text{min}^{-1}$ . The pump, syringe, and needle were placed on top of a 100-inch long polyethylene pipe and as the droplet fell down the fiber was formed inside the pipe. The pipe was used to avoid the air flow turbulence. The pipe was sprayed by antistatic spray to avoid any electrostatic forces through the pipe. The inner diameter of the needle was 0.9 mm. The fibers were fabricated at room temperature. 100 fibers were collected for every measurement. The fibers were collected at 4-inch, 7-inch, 10-inch, 13-inch, 16-inch, 34-inch, 52-inch, 73-inch, and 93-inch above the stage. The SEM images of a microfiber from a solution of PCL 10wt% in chloroform and a nanofiber from a solution of PEO 0.5wt% in water are shown in Figure 4.12a and Figure 4.12b, respectively.

### **4.4.2 Effect of Distance from the Ground**

In order to analyze the effect of height on the diameter of the gravitational dry-spun fibers, the droplet of the PCL 10wt% solution in chloroform was held at 94 inches above the ground, and

once it dropped and reached the ground level, the fiber was formed. The diameter of the drawn fiber was measured at different positions from the maximum height where the droplet fell down (height = 93 inch) to the ground (height = 0 inch). This process was repeated 50 times at similar conditions to find the average diameter of the fibers at different heights. This experiment was repeated while the droplet fell down from height = 53 inch and height = 18 inch, and the average diameters of the fibers were measured at different positions from the ground level. The results are exhibited in Figure 4.3a.

#### **4.4.3 Effect of Evaporation Rate**

In order to study the effect of evaporation rate of solvent, solutions of PEO 2wt% in various organic solvents with similar surface tension values were prepared. The evaporation rates of 1,4-dioxane, acetonitrile, and methanol are 29 mmHg, 72.8 mmHg, and 97 mmHg, respectively. The surface tension and viscosity of these solutions were similar and only the effect of evaporation rate was studied in this part of the study. The properties of these solutions are exhibited in Table 4.2. A droplet of every solution that was made separately in these three solvents was held at 94 inches above the ground and once the fiber was drawn the diameter of the fibers at different positions from height = 0 inch to height = 93 inch was measured. The average diameter of the fibers for these three solutions are shown in Figure 4.4a.

#### **4.4.4 Effect of Surface Tension**

In order to study the effect of surface tension, different concentrations of the TritonX-100 surfactant was prepared in PEO solutions. The viscosity of these solutions was similar. The surface tension values of PEO solutions in water with different concentrations of TritonX-100 are shown in Table 4.3. The surface tension of the PEO solutions in water decreased from 71.12 mN.m<sup>-1</sup> to 27.94 mN.m<sup>-1</sup> as the concentration of the surfactant in the solution increased from 0wt% to

0.5wt%. As it is shown in Figure 4.5a, adding surfactant to the polymer solution may reduce surface tension of the solution, therefore, less force is required to overcome the surface tension and at lower surface tension fibers become thicker.<sup>147</sup> According to Figure 4.5a and Figure 4.5b, increasing the surface tension acts to make the fiber size more uniform across its profile. The SEM images of the fibers drawn from TritonX-100 0.05wt% and 0.1wt% in PEO solution are shown in Figure 4.13a and Figure 4.13b, respectively.

#### **4.4.5 Obtaining a Master Curve**

According to Table 4.1, the polymer solutions mixed in various solvents have different evaporation rates, surface tensions, and viscosity. In order to consider the effect of all three properties on the diameter of the gravitational dry-spun ultralong fibers, PEO 2wt% solutions were made in various solvents such as anisole, water, 1,4-dioxane, acetonitrile, and methanol. The viscosity values of these solvents are almost the same, therefore, it is possible to show the relationships between vapor pressure, surface tension, and fiber diameter in a 3D-master plot (Figure 4.10c). In Figure 4.9, the sizes of single fibers are shown as a function of distance above the ground, and the effect of surface tension and evaporation rate has been demonstrated with different colors. Figure 4.9 verifies that by reducing the surface tension we can create a fiber with a larger radius even when the evaporation rate is larger, exactly as is observed experimentally in Figure 4.8.

### 4.5 Applications of the Gravitational Dry-Spun Ultralong Micro and Nanofibers

#### **4.5.1 Polarization**

A dense bundle of twisted gravitational dry-spun nanofibers was fabricated to study their chirality effect. The twisted fibers contained one fiber made from PCL 10 wt% solution in

chloroform and one fiber made from PCL 10wt% with embedded silver nanowires with the concentration of 6 wt%. Silver nanowires (Ag NWs) dispersed in ethanol (20 mg.mL<sup>-1</sup>) with an average diameter of 90 nm and length of 30 μm were obtained from ACS Material. The labelled fibers were fabricated at the flow rate of 30 μL.min<sup>-1</sup>. The polarization of the twisted fibers is compared to that of straight PCL fibers in Figure 4.15.

Figure 4.15a presents the optical transmission of the straight fiber with perpendicularly- and horizontally-polarized light, regards to the orientation of the fibers. The transmission in two cases show a strong fluctuation in terms of wavelength dependence which might come from the strong polarization dependent scattering of light with the straight polymer fiber. On the other hand, with twisted fiber, the polarization dependent transmission shows much less fluctuation. The twisted fiber with an extra dimension, has reduced the polarization dependence of scattering, results in a less fluctuation which can be seen in Figure 4.15b. The straight fibers are generally considered as one-dimension which exhibit polarization-dependent light scattering. However, the twisted and braided fibers can be considered as zero-dimension which do not show this polarization-dependence scattering. Therefore, the braided and twisted fibers have various potential applications.

#### **4.5.2 Cell Attachment on Fibers**

A 3D-scaffold was assembled by layer-by-layer deposition of nanofibers from the solution of PCL 10wt% in chloroform. The spacing between nanofibers was 50 μm in every layer and the layers were separated from one another by biodegradable polyglycolic acid (PGA) sutures with the thickness of 100 nm. The 3D-scaffold was placed in a 6-well plate and sterilized by UV irradiation for 3 days. For cell attachment experiment, 0.5 million RAW264.7 cells dispersed in 4.0 mL medium were added to co-culture with fibers for 24 hours, and fibers were fully submerged

in medium during this whole process. Afterwards, medium supernatant was removed and cells were washed with cold PBS for three times. Then, cells were lightly fixed with 100% ethanol under room temperature for 10 min and washed with cold PBS for three times. Optical images of cells that attached to fibers were taken. For confocal imaging purpose, fixed cells were further incubated with  $5.0 \mu\text{g.mL}^{-1}$  Wheat Germ Agglutinin, Alexa Fluor 488 conjugate (Invitrogen™) and  $2.0 \mu\text{g.mL}^{-1}$  Dapi (Invitrogen™) in PBS under room temperature in the darkness for 30 min and washed with PBS twice. Cells attaching on the fibers were imaged using LSM710 confocal microscope. According to Figure 4.16, the z-stack confocal images confirmed that the cells infiltrated into the scaffold and attached to the nanofibers. More experiments are required to create vascularization by inserting porous gravitational dry-spun microfibers in the scaffold.

#### 4.6 Conclusion

The gravitational-spinning method is a modified dry-spinning method that allows for drawing free standing single ultralong micro- and nanofibers for various biomedical, photonics, and textile applications. In the previous drawing techniques, the pulling speed was not efficient for manufacturing productivity, however, gravitational-spinning is capable of producing ultralong nanofibers in fraction of second. The productivity would be enhanced if more nozzles are available to eject polymer droplets. Furthermore, almost all of the polymer solutions and melts can be used in this technique for fiber spinning and the single nanofibers can precisely be placed on the surface of the substrate during fabrication.

#### 4.7 Acknowledgement

D.A. thanks Dr. J. Xie for giving access to his cell-culture facilities and A. Zakharchenko for his help for part of the 3D-scaffold fabrication. D.A. also thanks Georgia Electron Microscopy at the University of Georgia for access to SEM instrument and Dr. M.K. Kandasamy at Biomedical Microscopy Core at the University of Georgia for help with confocal imaging.

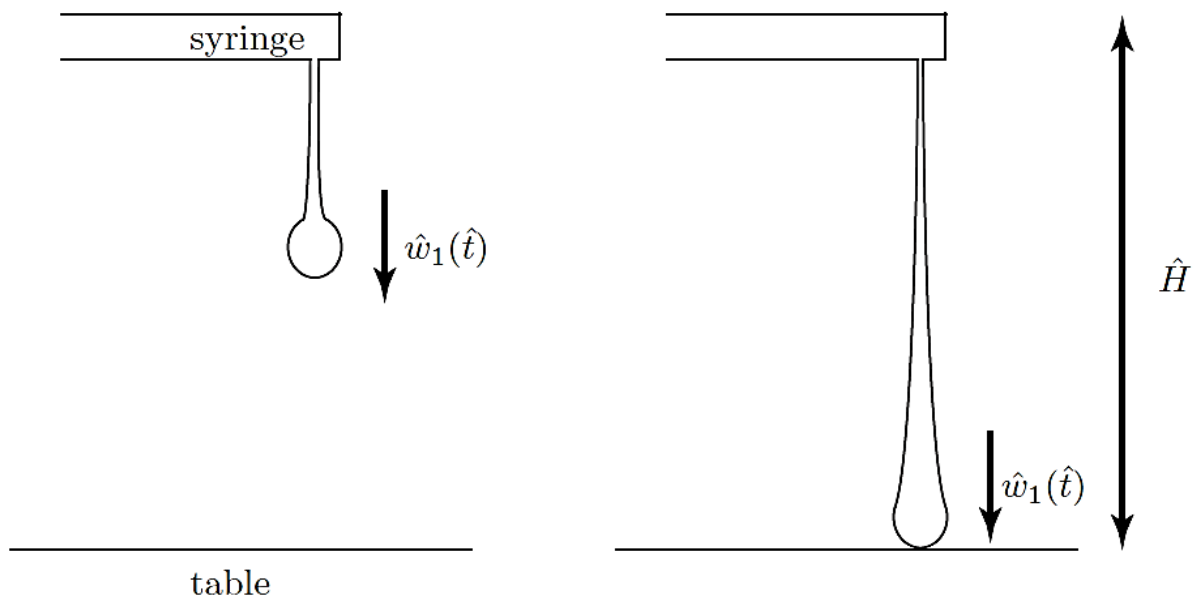


**Figure 4.1.** The gravity-spinning set-up. A droplet falls from a syringe at a velocity  $\hat{w}_1(\hat{t})$  striking the stage a distance  $\hat{H}$  below.

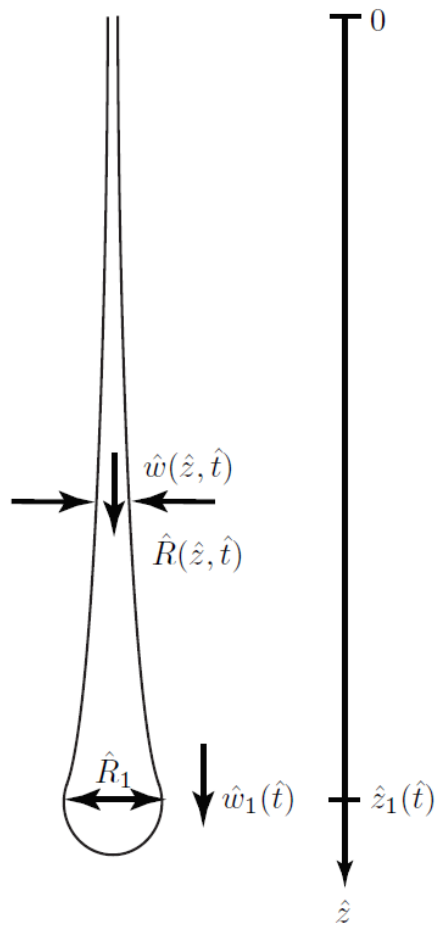


**Figure 4.2.** The schematic diagram of the gravity-spinning experiment. The droplet falls at speed  $\hat{w}_1(\hat{t})$  drawing out a fiber with cross-sectional radius  $\hat{R}(\hat{z}, \hat{t})$  and fluid velocity  $\hat{w}(\hat{z}, \hat{t})$ . The radius of the droplet  $\hat{R}_1$  remains constant as the droplet falls.

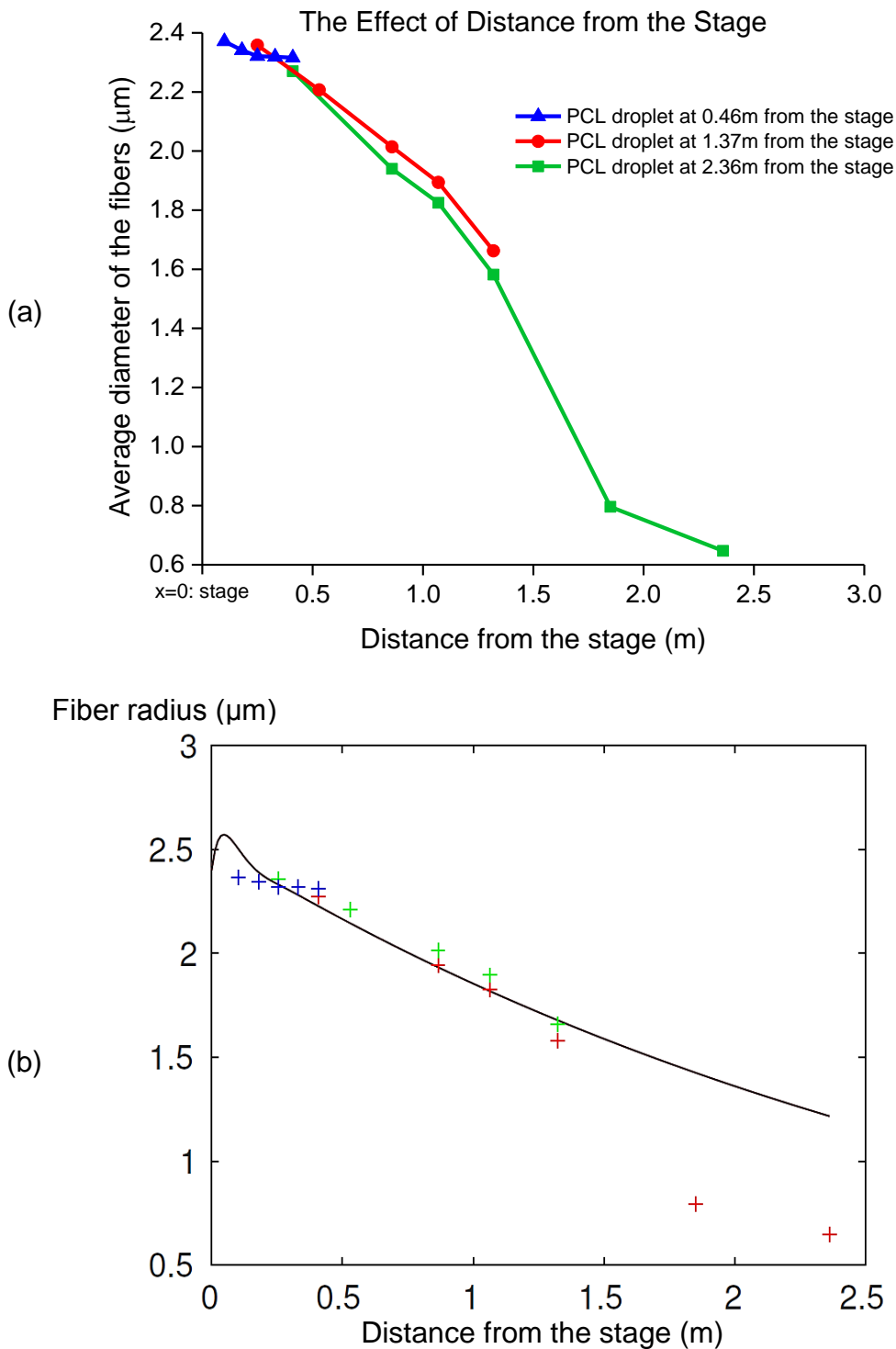


**Figure 4.3.** Comparison of theoretical prediction for the variation of fibre radius  $R$  with distance from the stage (solid curve) with experimental data (crosses) for the parameter values  $\alpha = 0$ ,  $\gamma = 0$ ,  $g = 0.9$ , and  $G = 1$ . (a) Experimental data; (b) Mathematical modeling.

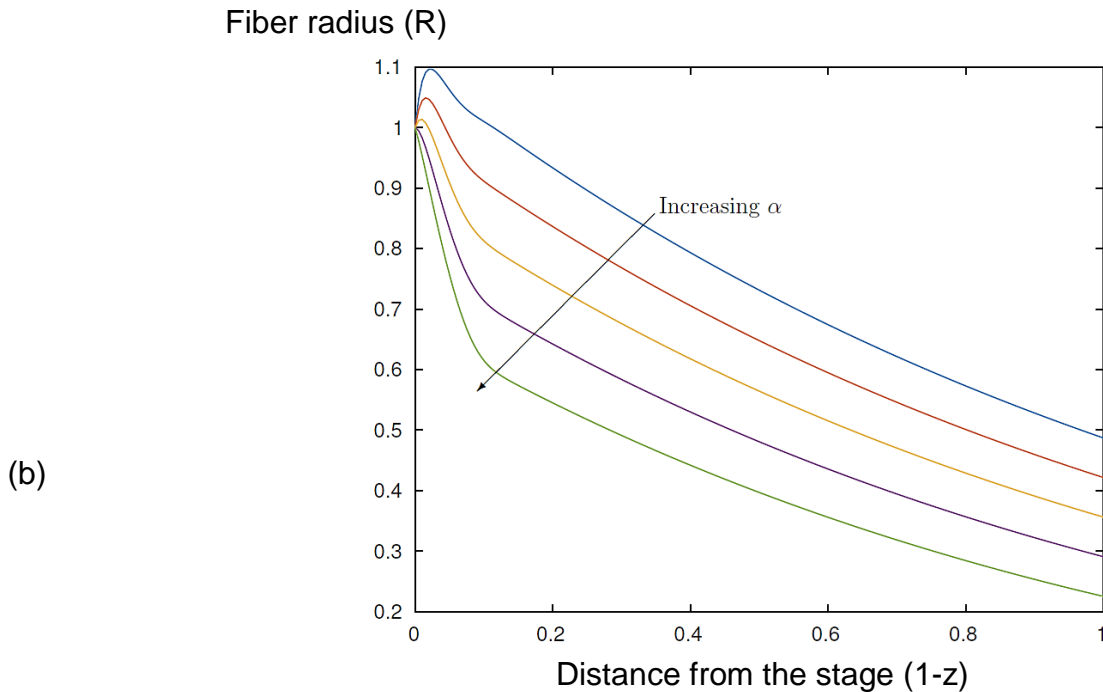
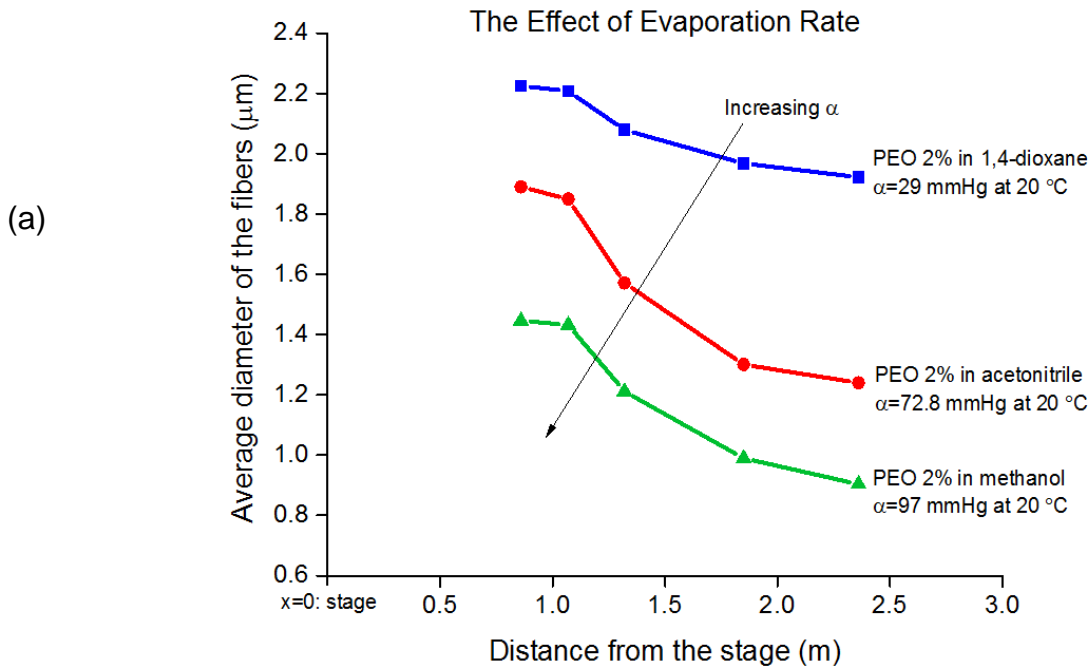


**Figure 4.4.** Variation of dimensionless fiber radius  $R$  (scaled with radius at the droplet) with dimensionless distance from the stage  $1-z$  (scaled with total stage height) as we vary the evaporation strength  $\alpha=0,0.1,0.2,0.3,0.4$ . Other parameters are  $\gamma=1$ ,  $g=1$ , and  $G=1$ . (a) Experimental data; (b) Mathematical modeling.

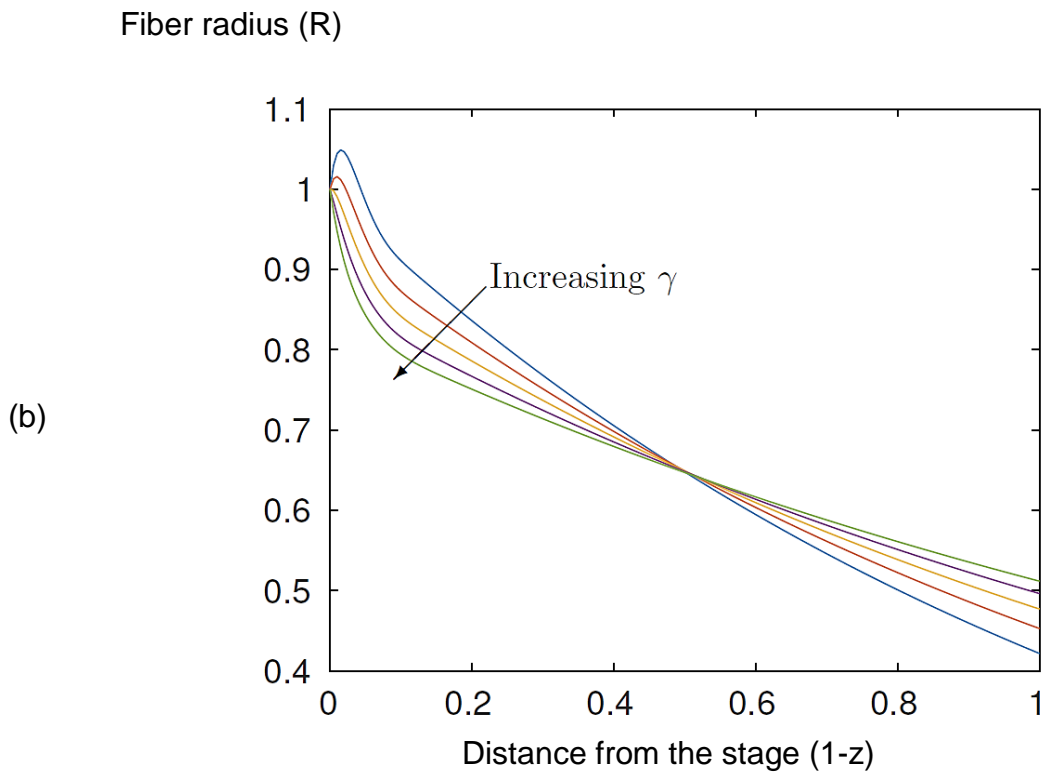
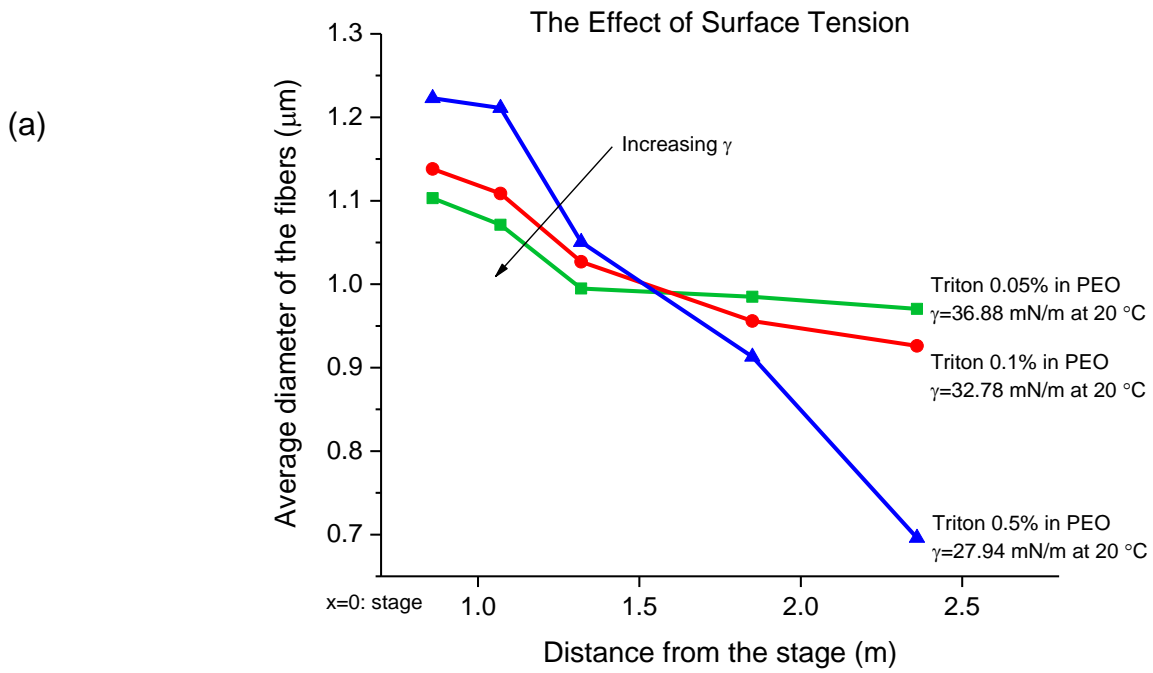


**Figure 4.5.** (a) Variation of dimensionless fiber radius  $R$  (scaled with radius at the droplet) with dimensionless distance from the stage  $1-z$  (scaled with total stage height) as we vary the surface

tension  $\gamma = 0, 1, 2, 3, 4$ . Other parameters are  $\alpha = 0.1$ ,  $g = 1$ ,  $G = 1$ . (b) Comparison with experiment showing the same qualitative agreement. (a) Experimental data; (b) Mathematical modeling. (a) Experimental data; (b) Mathematical modeling.

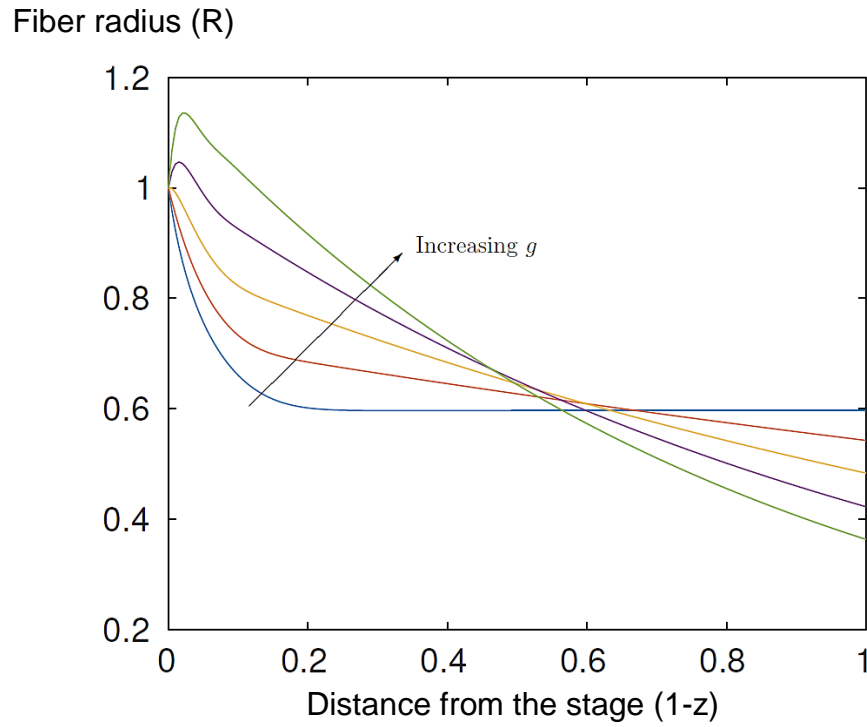


**Figure 4.6.** Variation of dimensionless fiber radius  $R$  (scaled with radius at the droplet) with dimensionless distance from the stage  $1-z$  (scaled with total stage height) as we vary the gravitational force on the fluid  $g = 0, 1, 2, 3, 4$ . Other parameters are  $\alpha = 0.1$ ,  $\gamma = 1$ , and  $G = 1$ .

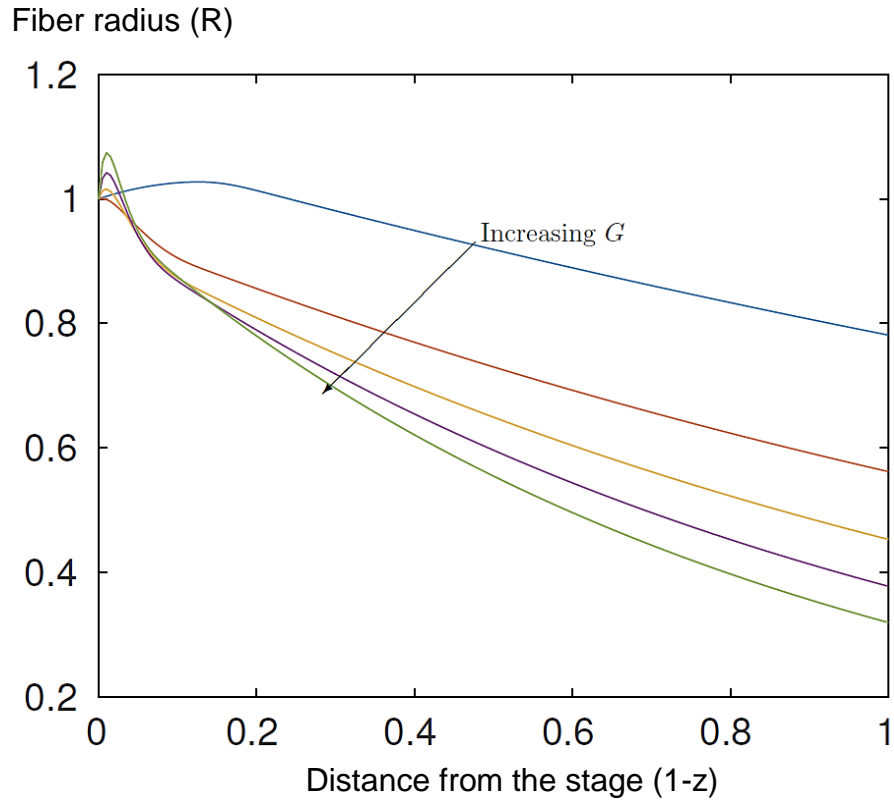


**Figure 4.7.** Variation of dimensionless fiber radius  $R$  (scaled with radius at the droplet) with dimensionless distance from the stage  $1-z$  (scaled with total stage height) as we vary the force on the droplet  $G = 0, 0.3, 0.6, 0.9, 1.2$ . Other parameters are  $\alpha = 0.1$ ,  $\gamma = 1$ , and  $g = 1$ .

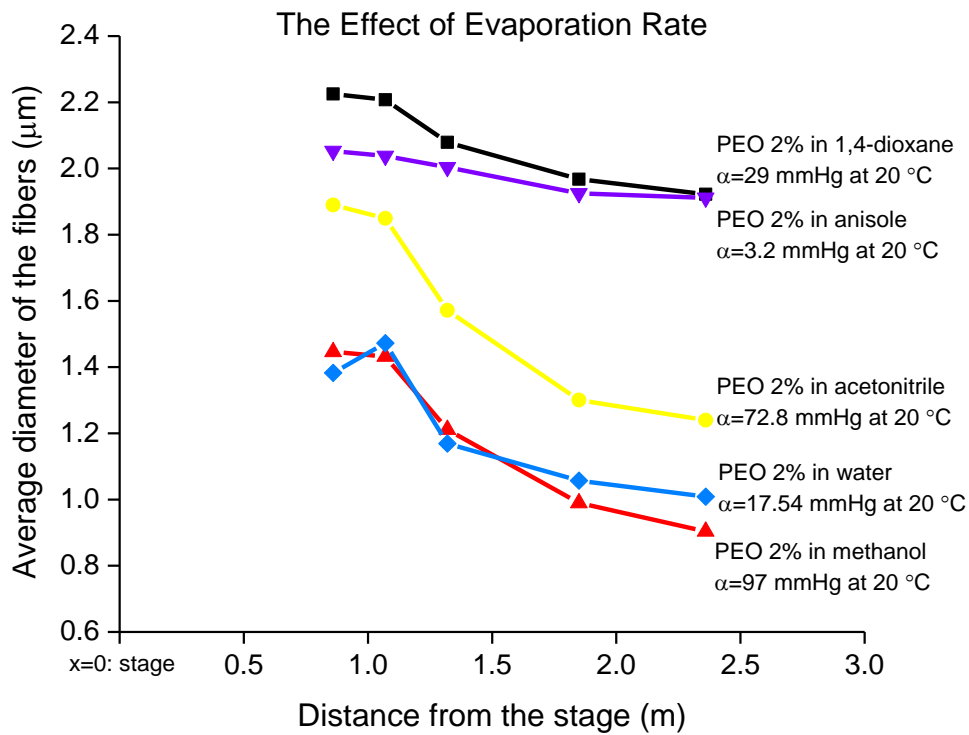


**Figure 4.8.** Variation of dimensionless fiber radius  $R$  (scaled with radius at the droplet) with dimensionless distance from the stage  $1-z$  (scaled with total stage height) determined experimentally for different solvents. Note that both evaporation rate and surface tension vary so we need a master plot to predict the variation.

**Table 4.1.** Vapor pressure, viscosity, and surface tension for the solvents used.

Solvent	Vapor Pressure (mmHg)	Viscosity (Pa.s)	Surface Tension (mN.m <sup>-1</sup> )
Anisole	2.4	$1.05 \times 10^{-3}$	36
Water	17.54	$1 \times 10^{-3}$	72.9
1,4-dioxane	29	$1.37 \times 10^{-3}$	33
Acetonitrile	72.8	$3.5 \times 10^{-4}$	19.1
Methanol	97	$5.9 \times 10^{-4}$	22.5

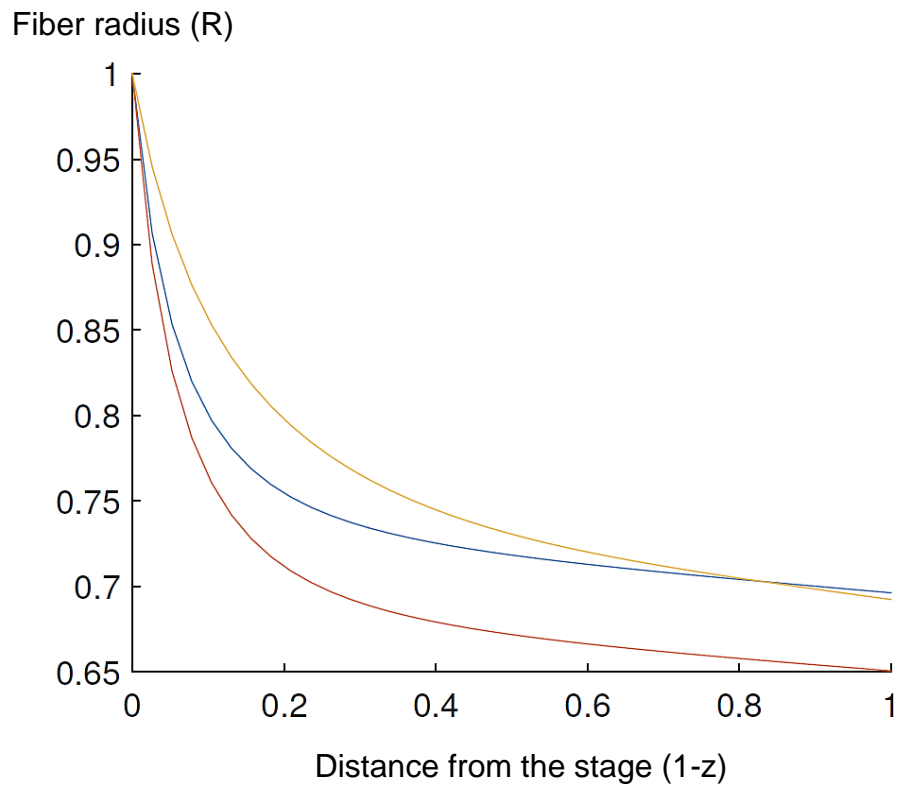


**Figure 4.9.** Variation of dimensionless fiber radius  $R$  (scaled with radius at the droplet) with dimensionless distance from the stage  $1-z$  (scaled with total stage height) for  $\alpha = 0.1$  and  $\gamma = 10$  (blue);  $\alpha = 0.15$  and  $\gamma = 10$  (red) and  $\alpha = 0.1$  and  $\gamma = 5$  (yellow). The graph illustrates that, by reducing the surface tension we can create a fiber with a larger radius even when the evaporation rate is larger, exactly as is observed experimentally in Figure 8.

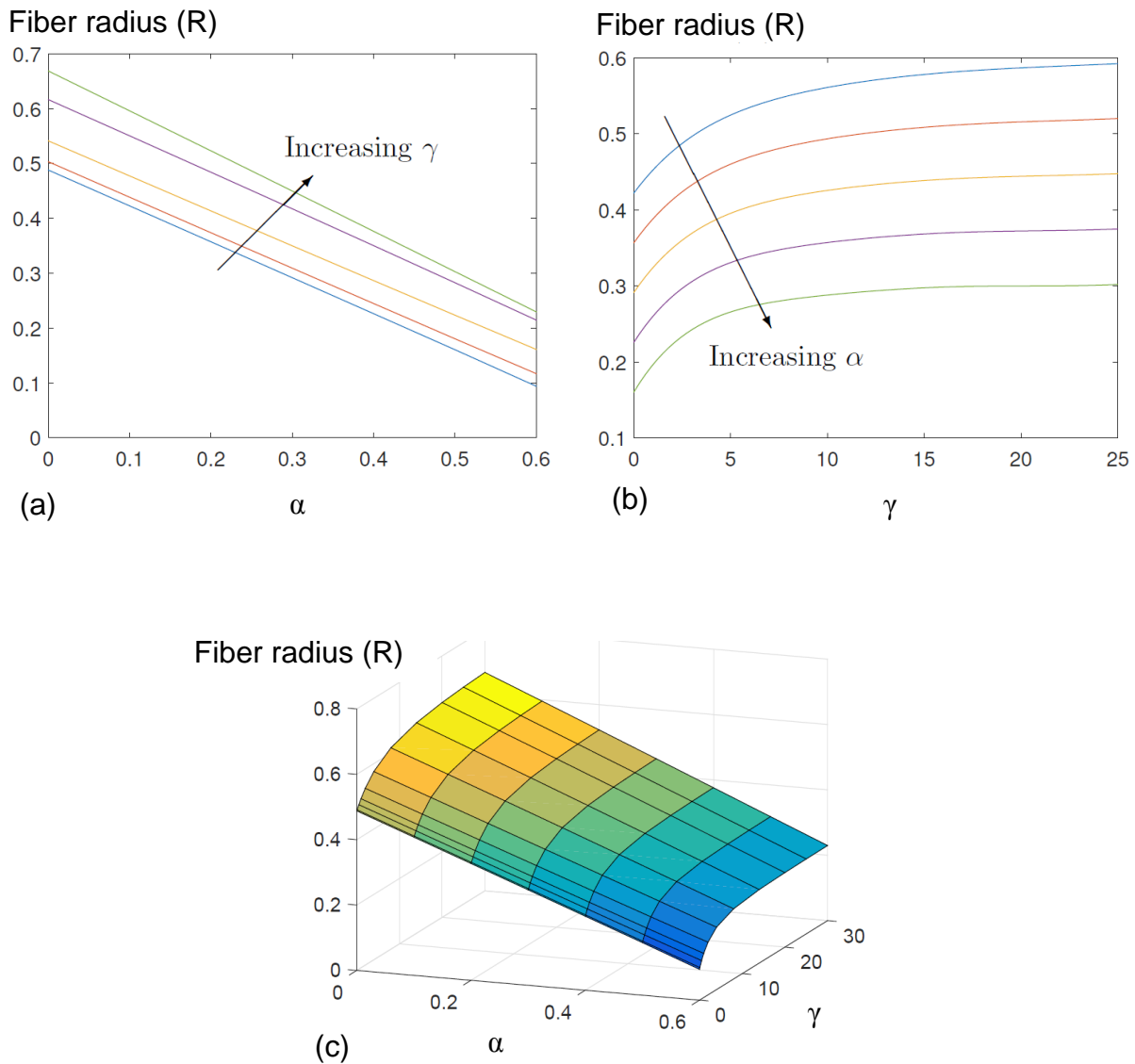


**Figure 4.10.** (a) Variation of dimensionless final fiber radius  $R$  (scaled with radius at the droplet) with evaporation rate  $\alpha$  as we vary surface tension  $\gamma = 0.02, 0.5, 2, 8, 30$ , with  $g = G = 1$ . (b) Variation of dimensionless final fiber radius  $R$  (scaled with radius at the droplet) with surface tension  $\gamma$  as we vary evaporation rate  $\alpha = 0.1, 0.2, 0.3, 0.4, 0.5, 0.6$ , with  $g = G = 1$ . (c) 3D-master plot showing dependence of final radius on  $\alpha$  and  $\gamma$  when  $g = G = 1$ .

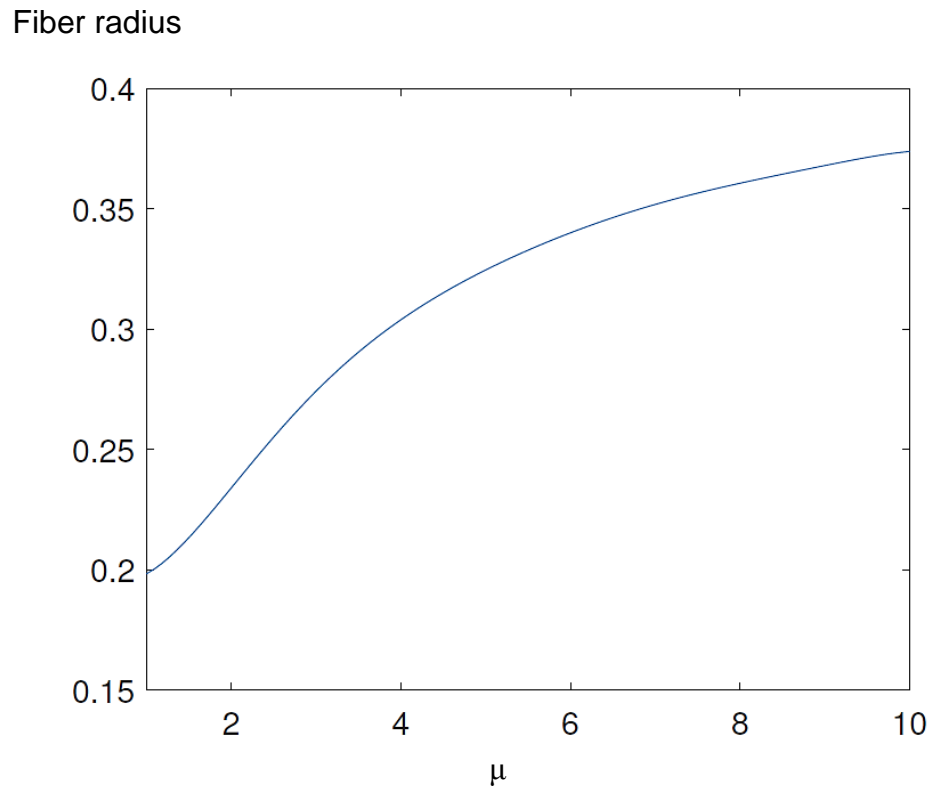
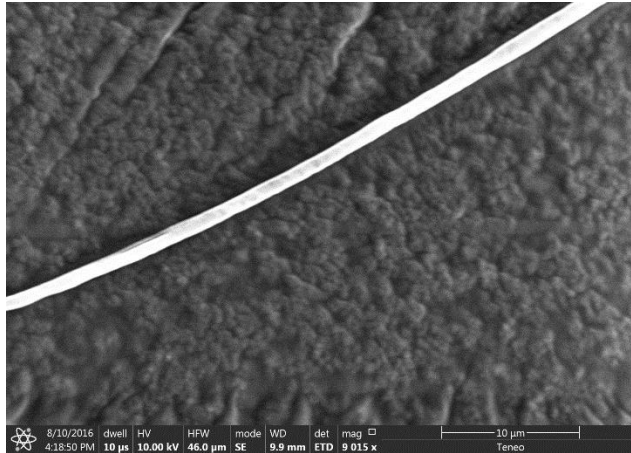


**Figure 4.11.** Variation of dimensionless final fiber radius  $R$  (scaled with radius at the droplet) with viscosity  $\mu$ . Here  $g = G = 1$  and we take  $\gamma = 5/\mu$ ;  $\alpha = 0.3/\mu$ .

(a)



(b)

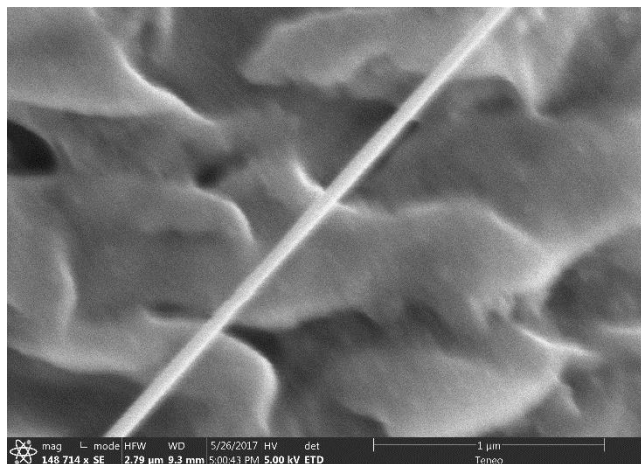


**Figure 4.12.** SEM images of a (a) microfibrillar structure from the solution of PCL ( $M_w \sim 80k$ ) 10wt% in chloroform, and (b) nanofibrillar structure from the solution of PEO ( $M_w \sim 8000k$ ) 0.5wt% in water using gravitational dry-spinning technique.

**Table 4.2.** Properties of PEO solution in various solvents at 20 °C.

	Evaporation Rate (mmHg)	Surface Tension (mN.m <sup>-1</sup> )	Viscosity (Pa.s)
PEO 2wt% in 1,4-dioxane	29	42.96	9.59
PEO 2wt% in acetonitrile	72.8	30.06	11.44
PEO 2wt% in methanol	97	36.28	18.18

**Table 4.3.** Properties of TritonX-100 in PEO solution at 20 °C.

	Surface Tension (mN.m <sup>-1</sup> )	Viscosity (Pa.s)
TritonX-100 (0wt%) in PEO in water	71.12	19.9
TritonX-100 (0.05wt%) in PEO in water	36.88	19.25
TritonX-100 (0.1wt%) in PEO in water	32.78	18.43
TritonX-100 (0.5wt%) in PEO in water	27.94	16.37

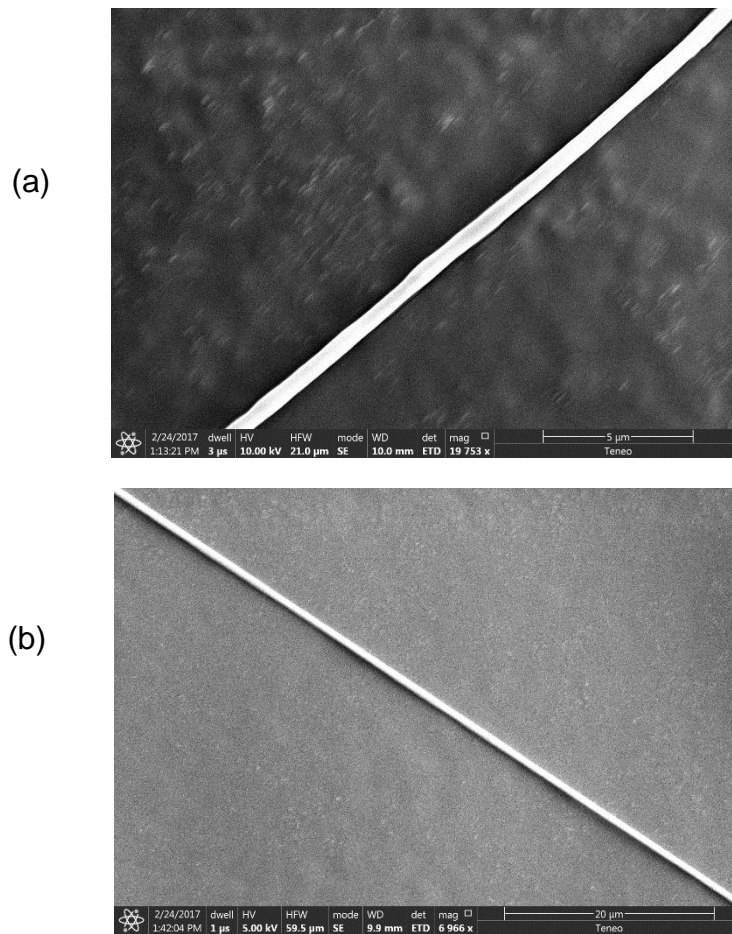
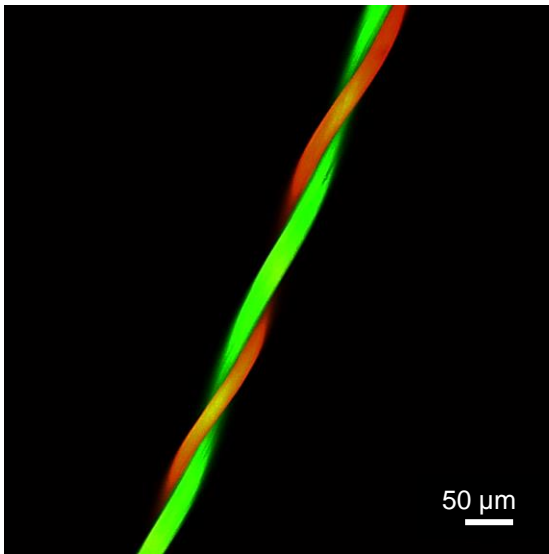


**Figure 4.13.** SEM images of (a) fiber from the solution of Triton 0.05wt% in PEO in water; (b) fiber from the solution of Triton 0.1 wt% in PEO in water.

(a)



(b)

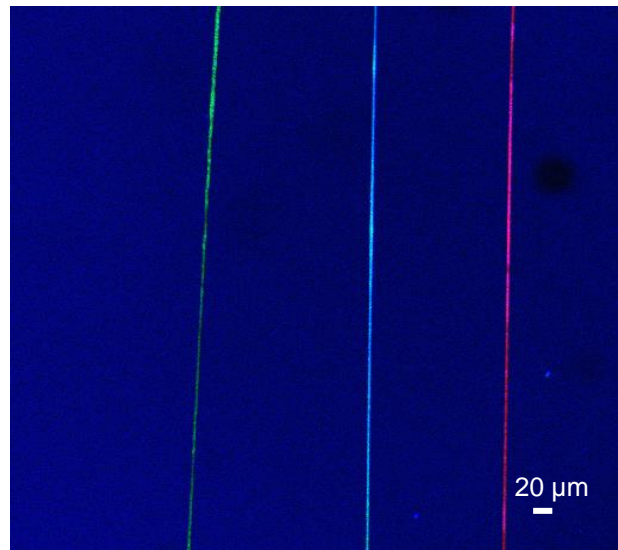
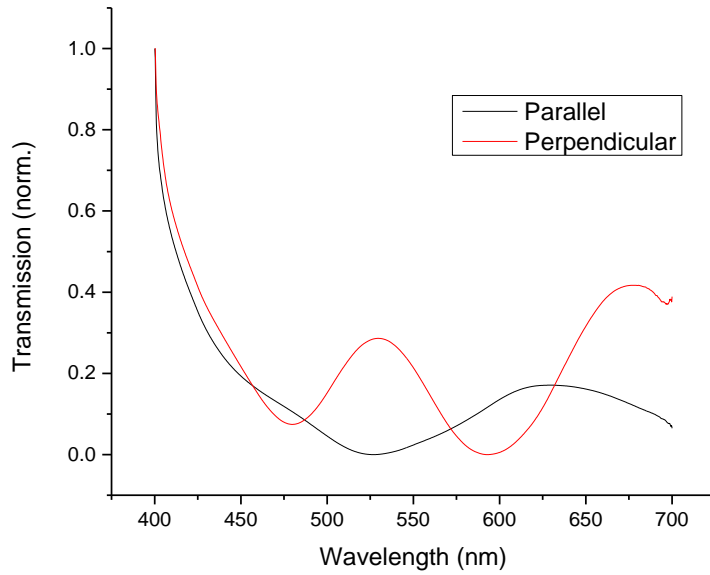


**Figure 4.14.** (a) Twisted and (b) straight fibers using gravitational dry-spinning technique.

(a)



(b)

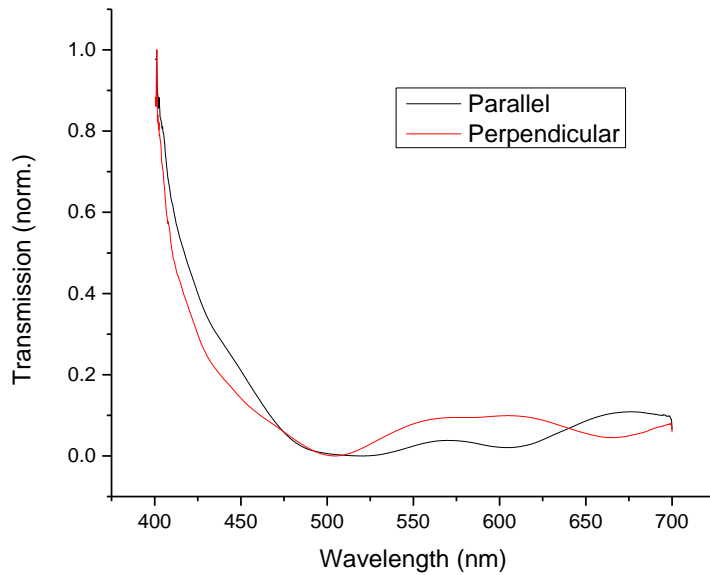


**Figure 4.15.** (a) straight fibers: including PCL straight fiber (diameter of 1 to 2  $\mu\text{m}$ ) embedded with silver nanowire (diameter = 90 nm, Length = 30  $\mu\text{m}$ ); (b) twisted fibers: including plain PCL fiber twisted with PCL fiber (diameter of 1 to 2  $\mu\text{m}$ ) embedded with silver nanowire (diameter = 90 nm, Length = 30  $\mu\text{m}$ ).

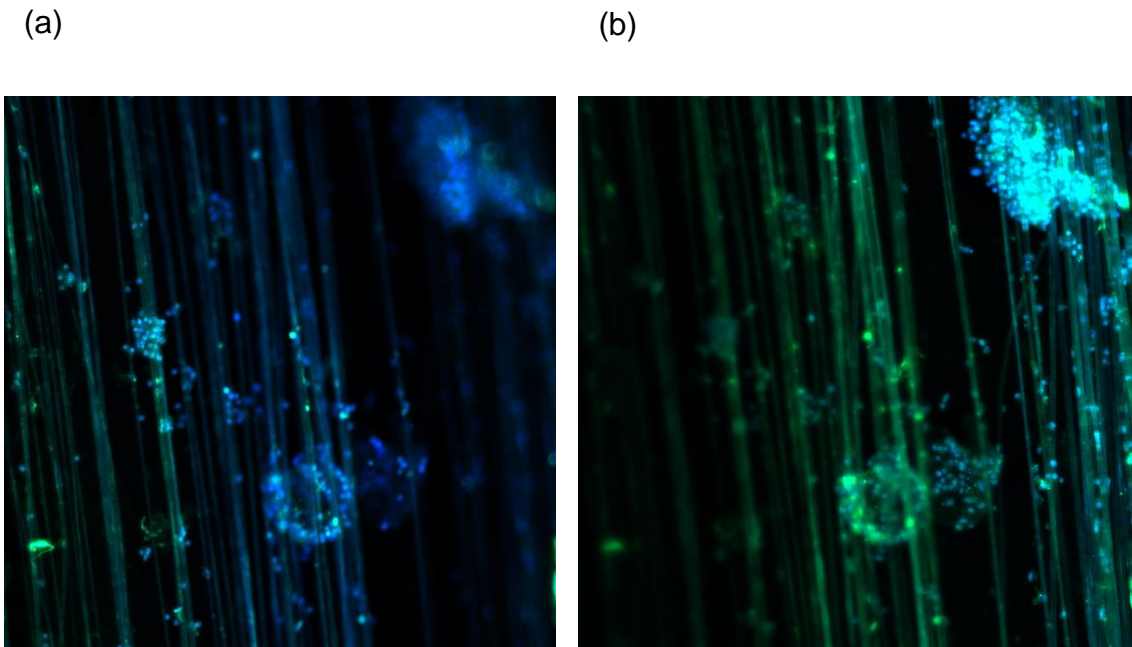


**Figure 4.16.** z-stack confocal images of the RAW264.7 murine macrophages attached to the gravitational-spun PCL fibers. The layers of PCL fibers were separated by 100- $\mu$ m thick PGA sutures. The cells infiltrated into the 3D-scaffold.

## CHAPTER 5

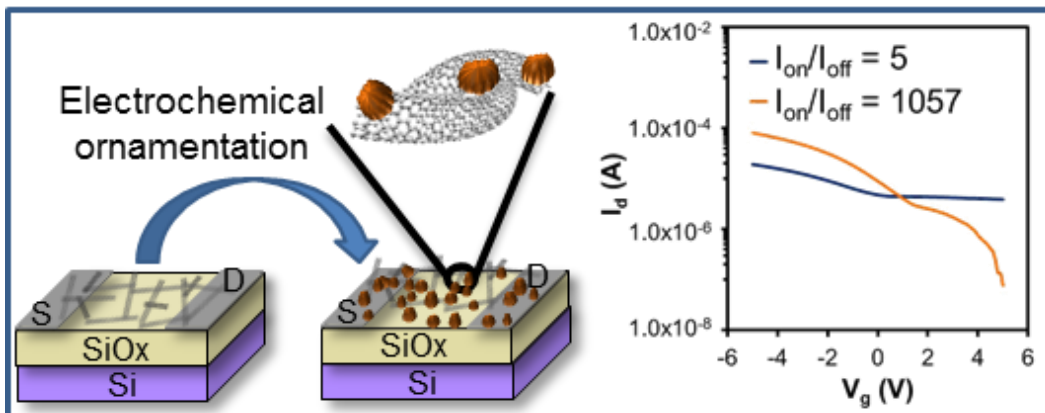
### CONVERSION OF METALLIC SINGLE-WALLED CARBON NANOTUBE NETWORKS TO SEMICONDUCTING THROUGH ELECTROCHEMICAL ORNAMENTATION <sup>4</sup>

---

<sup>4</sup> D. Asheghali, P. Vichchulada, M. D. Lay, 2013, *Journal of the American Chemical Society* **135** (20): 7511-7522. Reprinted here with permission from *JACS* **2013**, 135(20), 7511-7522. Copyright ©2013, American Chemical Society.

## 5.1 Abstract

Field-effect transistors (FETs) that incorporate single-walled carbon nanotube (SWNT) networks experience decreased on-off current ratios ( $I_{on}/I_{off}$ ) due to the presence of metallic nanotubes. Herein, we describe a method to increase  $I_{on}/I_{off}$  without the need for either specialized SWNT growth methods or post growth processing to remove metallic nanotubes. SWNTs that were grown using conventional arc discharge methods were deposited from aqueous suspension. Then, the SWNTs in the network were decorated with  $\text{Cu}_2\text{O}$  nanoparticles that acted as controllable valves that restricted current flow at positive gate voltages. This resulted in an unprecedented reduction in  $I_{off}$ , as sub-10 nm sized electrodeposited nanoclusters acted as numerous tunable valves, providing greatly improved network sensitivity to gate voltages in the relatively small range of  $\pm 5$  V. Larger nanoclusters were found to increase network conductivity, but not  $I_{on}/I_{off}$ . The ability to convert metallic SWNTs to semiconducting without removing them allows for enhanced  $I_{on}$ , and lower noise while still achieving greater magnitudes of  $I_{off}$ .



## 5.2 Introduction

Pristine, individual single-walled carbon nanotubes (SWNTs) have excellent electrical properties that far exceed those of semiconductors and metals currently used in microchip manufacturing. Depending on chirality and diameter, individual SWNTs may be semiconductive (s-SWNT) or metallic (m-SWNT). For s-SWNTs, the electron mobility is orders of magnitude greater than that for Si and GaAs.<sup>148</sup> While in m-SWNTs, the mean free path for an electron can exceed 2  $\mu\text{m}$ , making them prime candidates for use as electrical interconnects. Additionally, since conduction occurs via an extended  $\pi$  bonding network, they are not susceptible to electromigration, the movement of metal nuclei in response to momentum transfer from electrons during current flow. This is an increasingly significant failure mechanism as device structures decrease in size.<sup>149</sup> Therefore, both varieties of SWNTs have great potential in many microelectronics applications.

However, significant challenges remain for developing manufacturable electronic materials that make use of an individual SWNT as the active component, as one of the most notable characteristics of SWNTs is their polydispersity: for bulk growth processes, 1/3<sup>rd</sup> are m-SWNTs, while the other 2/3<sup>rd</sup> are s-SWNTs. Approaches to dealing with this problem include attempts at selective growth of s-SWNTs,<sup>150-152</sup> or post growth solution processing to remove m-SWNTs.<sup>153-156</sup> Even amongst s-SWNTs, the band gap varies with diameter and chirality from near 0 to  $\sim 1.8$  eV. Therefore, even after the separation of SWNTs based on their type of electrical conductivity, widely varying band gaps remain in the semiconductive portion, causing semiconductor device structures formed from individual SWNTs to be highly irreproducible. Additionally, the current drive through an individual SWNT is limited to the nA range, while higher current drives are needed by modern electronic devices. Further, device structures based on individual SWNTs will

require significant advances in the ability to control the length, orientation, and location of SWNTs during their growth or deposition.

Therefore, 2-D SWNT networks are the proximate route to their widespread use. In a 2-D array, the nanotube density and alignment largely dictate performance. Also, multiple SWNTs connected in parallel provide orders of magnitude more current than an individual SWNT. Further, unlike Si-based electronic materials, SWNT networks have great potential in transparent, lightweight, and flexible electronic materials, especially as new aqueous suspension-based deposition methods are developed for the polymer substrates used in these applications.

A drawback to the use of SWNT networks is their greatly reduced performance, relative to that observed for single-SWNT systems. This reduced performance is due to several factors that are addressed in this work: (i) Inter-device precision is low in field-effect transistors (FETs) based on SWNT networks in part because changes in the Schottky barrier height between s-SWNTs in direct contact with the metal source and drain electrodes dictate much of the response to the gate voltage ( $V_g$ ),<sup>157-159</sup> leaving the semiconductive channel largely unaffected. Also, the OFF-state current of SWNT network-based FETs is limited by the presence of the metallic pathways provided by m-SWNTs and small band gap s-SWNTs, since they are largely unaffected by  $V_g$ . These effects combine to increase the OFF-state source/drain currents in SWNT-based devices, greatly reducing their energy efficiency. (ii) Due to the inter-SWNT tunnel junctions that must be traversed in a network, their electron mobility decreases up to three orders of magnitude, relative to that for individual nanotubes.<sup>148, 160</sup> (iii) The poor attractive forces between metals and the  $\pi$  bonding network in nanotubes results in non-Ohmic contacts, increasing contact R and thereby reducing the level of ON-state current efficiency that can be achieved at a given

source/drain voltage, reducing the ON-STATE/OFF-STATE current ratio ( $I_{on}/I_{off}$ ). The approach to overcoming these three challenges is described in detail below.

To address issues related to the variability in conduction for SWNTs (*i*), electrodeposition was used to form numerous  $V_g$ -tunable contacts composed of high work function nanoclusters along the SWNT sidewalls. This facilitated much greater coupling between the nanotube network and  $V_g$ , as occurs in conventional Si-based FETs, allowing several orders magnitude in the reduction of  $I_{off}$  that could be achieved. This was facilitated by the decorating the network with nanoclusters of the high work function species  $Cu_2O$  ( $\Phi = 4.9$  eV).<sup>161</sup> This value is slightly higher than the experimentally determined work function of 4.6 - 4.8 eV for SWNT films.<sup>162</sup> High work function adsorbates withdraw electron density from s-SWNTs at the point of contact, increasing their band gap on a local level and increasing their sensitivity to gate voltages.  $Cu_2O$  is readily formed via electrochemical methods and has been widely investigated for use in solar cells,<sup>163-164</sup> sensors<sup>165-166</sup> and catalysis.<sup>167-168</sup> The  $\pi$  network in SWNTs is strongly affected by molecular adsorbates, with a molecular electron-withdrawing species increasing the nanotube's semiconductive character by increasing its band gap on a local level.

This manuscript also presents evidence that a band gap can be opened in m-SWNTs, obviating the need to separate them from s-SWNTs before network formation. This will greatly simplify network formation and optimization. In fact, OFF-state source/drain leakage currents were greatly reduced, facilitating a 211-fold increase in  $I_{on}/I_{off}$ . As the effect of metallic pathways on  $I_{off}$  is reduced, networks of increased density may be deposited without sacrificing  $I_{on}/I_{off}$ , facilitating the advantages in reproducibility and current drive provided by greater numbers of SWNTs.<sup>169</sup> This apparent conversion of m-SWNTs is attributed to the fact that they are not true metals, but in fact zero band gap semiconductors, or semimetals, like graphene.<sup>170-171</sup> Therefore,

our deposition method for metal oxide nanoclusters is an effective way to open a band gap in m-SWNTs by inserting a point where conductivity can be controlled along an otherwise conductive nanotube.<sup>172</sup>

The inter-SWNT tunnel junction (*ii*) is unique to network devices. At these junctions, surface-bound SWNTs have a slightly increased contact area to each other due to a slight deformation of the tubes caused by van der Waals attractions. However, since the tunneling probability for an electron decays exponentially with distance, the 3.5 Å van der Waals spacing between crossed nanotubes presents a non-trivial barrier. Additionally, Schottky barriers between m- and s-SWNTs present numerous high-R barriers in a network.<sup>173-175</sup>

In this work, inter-SWNT R was reduced by depositing low-defect, unbundled nanotubes in a manner that allowed control over the density and alignment of SWNTs in the network. Inter-SWNT R is greatly increased for a network composed of bundles of nanotubes, compared to individuals.<sup>176</sup> Therefore, we employed a new method for producing suspensions of unbundled high aspect ratio SWNTs and depositing them without allowing bundle formation,<sup>177</sup> while maintaining strict density control over the network during all states of its formation.<sup>178-179</sup> Density control is important because as density increases, conductivity, current drive,  $I_{on}/I_{off}$ , and reproducibility increase. However, at very high nanotube density, the electron mobility and  $I_{on}/I_{off}$  begin to decrease due to bundle formation and charge shielding.<sup>180</sup> Further, this deposition method allowed large number of SWNTs to be deposited either in a random orientation, or with partial alignment.<sup>181</sup> The ability to increase the SWNT alignment allowed the number of inter-SWNT tunnel junctions to be reduced, maximizing the advantages in electron mobility provided by the SWNT.

Recent computational studies by Li and Marzari found that while the inter-SWNT van der Waals distance is 3.5 Å, the C-transition metal atom distance is 2.4 Å.<sup>182</sup> This is a significant reduction in distance, considering the exponential dependence of tunneling current on barrier distance. They also reported that the Cu-C bond was found to have a very low binding energy (0.38 eV), due to the full d-orbitals in Cu, and that transition metals with low binding energies with C had greater quantum conductance near the Fermi level between crossed s-SWNTs. Therefore, the electrodeposition of randomly distributed Cu-containing nanoparticles is expected to produce nanoparticles that fortuitously bridge inter-SWNT junctions and reduce inter-SWNT R by reducing the tunneling barrier height between s-SWNTs, and the Schottky barrier height between m-SWNTs and s-SWNTs.

Optimizing electron transfer across heterojunctions (*iii*), is an important consideration for incorporating any nanomaterial into conventional device structures. For SWNTs, this is complicated by difficulties with forming low-resistance metal-C bonds due to the poor “wetting” of sp<sup>2</sup>-hybridized C by most transition metals, and Schottky barriers between s-SWNTs and metals.<sup>183</sup> This reduced attraction between metals and SWNTs leads to an increased electron tunnel barrier, increasing the R between source and drain contacts. An additional obstacle to interfacial transport is presented by the semiconductive variety of SWNTs, due to the formation of a Schottky barrier at their contacts to metal electrodes severely limiting the transistor ON-state current  $I_{on}$ .

Interfacial R was reduced as electrodeposited nanoclusters effectively nanosoldered the metal/SWNT junctions, providing an increased contact area to all SWNTs, and a reduced Schottky barrier height to s-SWNTs. The reduced C-transition metal atom distance expected for the Cu oxides allowed them to act as low resistance “shunts” that facilitated electron transfer from/to

metal source and drain electrode pairs. This addresses a critical concern, as interfacial contacts often dictate the electrical properties of SWNT-based systems, rather than the enhanced properties of nanotubes.<sup>184</sup>

Previous efforts to reduce the interfacial R between SWNTs and metals often involve high temperature annealing. For example, chemical reactions between SWNTs and various metal carbides were driven at temperatures above 900 °C to form nanotube-carbides, reducing R to  $\sim 1/4^{\text{th}}$  of its original value.<sup>185</sup> In another instance, resistive heating of a gold electrode was used to effect “local melting,” in order to embed multi-walled carbon nanotubes (MWNTs) into the electrodes.<sup>186</sup> The R was reduced by 60%, with the effect being attributed to increased interfacial contact area to the MWNT. A 5-fold increase in current was also achieved by using the electron beam in a scanning electron microscope to solder MWNTs to Au electrodes by decomposing a gas phase gold-C precursor.<sup>187</sup>

A recent report by this group revealed that controlled chemical oxidation, followed by annealing at just 300 °C could greatly improve conductivity in SWNT networks.<sup>188</sup> The order in which the various device structures were formed played a crucial role in the extent to which R could be reduced during post-fabrication treatments. When electrical contacts were deposited on top of pre-existing networks, a moderate level of R reduction was observed. This indicates that if the metal/SWNT contacts are closed to further chemical reactions, the only reduction in R observed is that due to the enhanced inter-SWNT contacts formed during annealing. This was confirmed by Raman microscopy, which indicated a reduction in the density of sidewall defects in SWNTs, and desorption residual dopants. However, when the network was deposited on top of prefabricated Ti electrodes, a 13-fold reduction in R and an 18-fold increase in the inter-device precision could be ascribed to the formation of “molecular anchors” at the inter-SWNT and

metal/SWNT junctions. Evidently, the large contact area over which there was chemical access to the metal/SWNT interface, relative to device structures with nanotubes buried in metal electrodes, allowed for greater optimization of the interface. The chemical access provided by depositing SWNTs onto prefabricated Ti electrodes provides a unique opportunity to use electrodeposition to increase electronic transport.

In order to test an electrochemical approach to device optimization, Ti electrodes were formed on a variety of silica-terminated surfaces. SWNTs do not readily adhere to native silica or Ti surfaces. However, the native oxide that formed on Ti in air resulted in a titania-terminated surface, which like silica was amenable to modification via self-assembled monolayer formation by a silane. Therefore, all surfaces were treated with a silanization agent to form a self-assembled monolayer that served as an adhesion layer. Then, electrodeposition was used to form conductive shunts through the silane and the native  $\text{TiO}_x$  adlayers, bridging the gap between SWNTs and the conductive Ti below. To simplify the discussion of the titania surfaces, they will be referred to as Ti/ $\text{TiO}_x$ . Although Ti/ $\text{TiO}_x$  was used for these studies, this method is expected to significantly improve interfacial electron transport between SWNTs and other metals that form native oxides, like Al, Ta, Ni and various ferrous systems.  $\text{Cu}^{2+}$  was used for electrodeposition in these studies since its oxides form readily in an electrochemical environment, and they are p-type, wide band gap semiconductors, like SWNTs. Also, the copper oxides have high work functions, which allow them to serve as electron withdrawing dopants when in direct contact with nanotubes.

The electrochemical nanosoldering method described in this manuscript is a room temperature, inexpensive, and facile route to obtaining great gains in conductance and  $I_{on}/I_{off}$  since it specifically decorates the SWNTs and metal electrodes with nanoclusters of controllable size distributions. This is facilitated by control over the magnitude of the driving force for the metal

deposition (via the electrochemical potential), and precise control over the average size of the nanoparticles (via the charge that is allowed to pass). Further, electrodeposition is a non-line-of-sight deposition method that prohibits deposition on nonconductive parts of the surface, allowing preferential deposition on individual SWNTs dispersed on insulating substrates. These abilities provide distinct advantages over physical vapor deposition methods, which indiscriminately deposit molten metal nanoparticles over the entire sample.

### 5.3 Experimental Details

#### **5.3.1 Substrate Preparation**

A dual-filament thermal evaporator (Thermionics), operating under high vacuum ( $P < 1 \times 10^{-6}$  torr), was used to deposit 150 nm of Ti (99.995% pure, 1/8" diameter pellets, Kurt J. Lesker Company) onto either Ti-coated glass slides or photoresist-coated, lithographically patterned Si/SiO<sub>x</sub> wafers. Then, the substrates were cleaned with a compressed CO<sub>2</sub> snow-jet. The entire samples, including the Ti/TiO<sub>x</sub> electrodes were modified with a silane monolayer that served as an adhesion layer for the SWNTs, using a method described by this group previously.<sup>177-178</sup> Briefly, samples were immersed for 45 min. in a solution of 10 mM 3-(aminopropyl) triethoxysilane (3-APTES, 99%, Aldrich) in ethanol (99.5%, absolute 200 proof, ACROS). Next, the samples were cleaned in a stream of fresh ethanol and then water. In order to ensure that excess layers of the silane were removed, the surfaces were cleaned with compressed CO<sub>2</sub> from a snow-jet as this has proven effective for removing excess silane, leaving only a strongly bound monolayer on the surface.<sup>189</sup>

For testing the effect of nanocluster formation on SWNT network FETs, source and drain electrode pairs were formed using standard optical lithography methods. UV-light exposure

through a patterned quartz mask was used to project the pattern for the electrodes onto photoresist-coated Si/SiO<sub>x</sub> wafers. This was followed by Ti physical vapor deposition and photoresist lift-off to yield 150 nm-thick source/drain electrode pairs on top of a 500-nm thick dielectric SiO<sub>x</sub> layer. Prior to SWNT network deposition, these samples were modified with a silane layer, as described above.

### 5.3.2 SWNT Suspension and Network Formation

Arc discharge soot (AP grade, Carbon Solutions, Inc.) was dispersed into an aqueous 1% sodium dodecyl sulfate (SDS, J.T.Baker) solution via probe ultrasonication (Fisher Model 500) at a power density of 0.4 W/mL. These conditions have been previously described as effective at forming stable suspensions of high aspect ratio SWNTs, while minimizing sonication induced damage to the nanotube sidewalls.<sup>190</sup> Next, a low relative centrifugal force (RCF) processing method was used to separate the undamaged, high aspect ratio SWNTs from amorphous C and residual catalyst contaminants.<sup>177</sup>

This group has developed an SWNT network formation method that uses iterative deposition cycles to grow a network from the bottom up, while avoiding SWNT bundle formation.<sup>181</sup> To deposit reproducible densities of unbundled SWNTs bridging the electrodes, the silanized surfaces were wet with a purified SWNT suspension and immediately dried in a unidirectional stream of N<sub>2</sub> and rinsed with copious amounts of H<sub>2</sub>O. This deposition cycle was repeated eight times for all samples to build networks that were composed of similar densities of unbundled SWNTs, as described previously.<sup>178-179, 181</sup> For samples designated “aligned,” one drying direction was used to deposit SWNTs, while for “crossbar” samples an equal number of orthogonal drying steps were used. The initial R, prior to electrochemical experiments, for all samples was ~1 MΩ.

### 5.3.3 Electrochemical Setup

In order to determine the effect of the area of the SWNT network relative to the contact area provided by the metal electrodes ( $A_{\text{network}}/A_{\text{Ti}}$ ) on the electrochemical response and change in two-terminal R, samples of various dimensions were analyzed in either sealed glass beakers, or homemade glass electrochemical cells, as described below. The glass cells employed a Viton gasket at the bottom that restricted the working electrode area to a 1.0 cm diameter disk. All cells were purged with high-purity N<sub>2</sub> for at least 30 minutes prior to all experiments. Solutions were composed of 0.1 M CuSO<sub>4</sub> and 0.5 M H<sub>2</sub>SO<sub>4</sub> (Aldrich) in ultrapure water (18.2 MΩ, Millipore). Standard three-electrode electrochemical cells, with each sample serving as the working electrode, were connected to a potentiostat (CH Instruments, 600C), with a Au wire serving as a counter electrode, and a Ag/AgCl reference electrode (3 M KCl, BASi). A scan rate of 50 mV/s was used for all cyclic voltammetry (CV).

### 5.3.4 Analytical Methods

Atomic force microscopy (AFM) was performed in air using intermittent contact mode (Molecular Imaging, PicoPlus). To determine the effect of various electrodeposition conditions on the density and height of the nanoclusters, at least five areas of each sample were analyzed with AFM image analysis software (WSxM, v5.0).<sup>191</sup> Raman spectroscopy (Thermo Scientific, DXR SmartRaman) was performed on samples using a 532 nm laser excitation source with 5 mW intensity at the sample, 100 X objective, and a charge-coupled (CCD) detector. A semiconductor characterization system (Keithley, 4200SCS) and probe station (Signatone, S-1160A) were used to ascertain the effect of nanoparticle size on two-terminal R and transistor performance.

## 5.4 Results and Discussion

### **5.4.1 Electrochemistry of Cu<sup>2+</sup> on Ti/TiO<sub>x</sub> Surfaces**

The ~20 Å thick native oxide that spontaneously forms on fresh Ti surfaces is largely composed of TiO<sub>2</sub>, which is essentially an insulator having a band gap of 3.7 eV.<sup>192</sup> Crystalline forms of this passivation layer are of interest as a dielectric material in electronic device structures.<sup>193</sup> In these studies, thermal evaporation was used to form amorphous Ti layers with native oxides that were highly inhomogeneous, characterized by numerous grain boundaries and defects. Previously reported conductive atomic force microscopy (C-AFM) studies of polycrystalline Ti/TiO<sub>x</sub> electrodes demonstrated that grain boundaries between crystals in the underlying Ti exhibit more than a 200-fold increase in conductivity compared to TiO<sub>2</sub> layers over crystal facets.<sup>194-195</sup> They were only able to estimate the size of these conductive hotspots at <50 nm, due to the resolution limits imposed by the C-AFM probe. The electrochemical response of Ta electrodes (terminated by a 25 Å thick native oxide) was also found to be defined by similar microscopic electrochemically active low-valence-oxide defects in a largely dielectric layer.<sup>194</sup>

In the case of the Ti surfaces described herein, low valence Ti oxides (Ti<sub>2</sub>O<sub>3</sub> and nonstoichiometric TiO) existed as shunts through the dielectric TiO<sub>2</sub> adlayer. Metallic conduction is observed for the nonstoichiometric Ti oxides which have a Ti/O ratio of 0.8 to 1.7.<sup>196</sup> The amorphous Ti/TiO<sub>x</sub> surfaces used in these studies are expected to have numerous sub-nm sized electrochemically active hotspots that represent conductive shunts to the underlying Ti. These shunts, when electrically connected to SWNTs, provide a valuable route to reducing the interfacial R in device structures.

The TiO<sub>2</sub> oxide caused the Ti/TiO<sub>x</sub> samples to have a smaller electrochemically active surface area, as the conductive defects acted as an array of connected nanoelectrodes. This resulted

in the nucleation and growth of numerous nanoparticles, rather than the formation of the conformal monolayers observed on noble metals. Ti/TiO<sub>x</sub> surfaces were investigated at every step of the surface preparation process as follows (Figure 1a): the unmodified Ti/TiO<sub>x</sub> surface, the silane-modified Ti/TiO<sub>x</sub> surface (TiO<sub>x</sub>/silane), and the silane-modified Ti/TiO<sub>x</sub> surface in the presence of adsorbed SWNTs (TiO<sub>x</sub>/silane/SWNTs).

Numerous Ti/TiO<sub>x</sub> samples were prepared as described above and mounted in a cell that restricted the electrochemically active area to 3.14 cm<sup>2</sup>. Freshly made samples were used for each electrochemical experiment and AFM analysis of deposits demonstrated that the density of nucleation points was similar for all samples of Ti/TiO<sub>x</sub>. As each CV started at the open circuit potential, 0.315 V, and progressed at 50 mV/s in the negative (cathodic) direction, a large peak between -0.20 and -0.30 V corresponded to the reductive deposition of copper oxide nanoclusters (Figure 1b). The TiO<sub>x</sub>/silane/SWNTs samples had increased electrochemical current for these cathodic waves, relative to the TiO<sub>x</sub>/silane samples. Evidently, the presence of the highly conductive SWNTs provided an increased density of nucleation points, resulting in the deposition of greater densities of nanoparticles, and commensurately higher current.

Each cathodic scan ended at -0.4 V, where the scan direction was reversed, and an anodic scan (toward positive potentials) began. Initially, the magnitude of reductive current remained high enough to cause each anodic curve to cross the cathodic scan at two points, near -0.16 and 0.02 V. While this behavior would be unusual for the electrodeposition of a conformal layer on a flat, noble metal surface, it is commonly observed for electrodeposition on metal oxide-terminated surfaces. Such crossover points are caused by nucleation and growth processes enhancing the electrode area, and thus the deposition current.<sup>197-198</sup>

As the anodic scans continued, large waves around 0.4 V represented the oxidation of  $\text{Cu}_2\text{O}$  to form  $\text{CuO}_{(s)}$ . For the Ti/TiO<sub>x</sub> samples, the amount of charge flow was 9,539 and 1,300 mC in the cathodic, and anodic waves, respectively. The larger magnitude of anodic current indicated that the CuO remained stable on the surface. The oxidative dissolution of CuO was not observed since potentials positive enough to facilitate this would have further oxidized the Ti/TiO<sub>x</sub> surface,<sup>197, 199</sup> increasing the thickness of its native oxide and the interfacial R between the SWNTs and electrode. The amount of current for the deposition of nanoparticles decreased notably for the TiO<sub>x</sub>/silane samples, relative to the Ti/TiO<sub>x</sub> samples. This was due in part to the silane effectively reducing the active electrode area by inhibiting access to the conductive shunts in the Ti/TiO<sub>x</sub> surface.

After CV revealed the potentials at which nanoparticle deposition occurred, constant potential deposition (chronoamperometry) at 0.10 V vs. Ag/AgCl was used to obtain information about the reaction rate on each surface. The amount of charge allowed to flow was limited to 16.7 mC for each surface, as this allowed the growth of nanoparticles of sufficient size to be characterized with AFM, as discussed subsequently. As 0.10 V is just negative of the equilibrium potential (0.35 V), the reaction rate was slow and the shape of the extended *i* vs. *t* curves could be examined (Figure 1c). The Ti/TiO<sub>x</sub> samples had the highest current density, followed by the TiO<sub>x</sub>/silane samples due to inhibition of electron transfer caused by the silane monolayer, as observed for CVs. However, the TiO<sub>x</sub>/silane/SWNT samples differed markedly with respect to the other samples, as the *i* vs. *t* curves had a sigmoidal shape that indicated that the initial nucleation process was enhanced. Then, the current reached a brief diffusion-limited regime that was followed by a broad wave of increasing current density. Additional experiments revealed that this increase in current continued indefinitely for the TiO<sub>x</sub>/silane/SWNT samples.

Metals that are not terminated by oxide layers (i.e. Au, or Pt) typically have  $i$  vs.  $t$  traces with an initial spike in current, followed by an extended region of steady-state current. This initial current spike is due to the charging of the electric double-layer and the immediate reaction of electroactive species at the electrode's surface, while in the steady-state region, deposition is limited by the rate of diffusion of the analyte to the electrode. Alternatively, unique chronoamperometric current transients are often observed during electrodeposition at heterogeneous metal oxide surfaces,<sup>200</sup> where an initial spike in current indicates instantaneous nucleation. This is followed by a broad sigmoidal feature that is typical of progressive nucleation (the density of nucleation sites increases with time), in addition to growth, resulting in continually increasing current density. This sigmoidal feature is typically observed at high driving forces (more negative potentials) for the reaction, so its observation for the TiO<sub>x</sub>/silane/SWNT samples indicated that the SWNT enhanced the nucleation process. Then, at longer deposition times continually increasing current is expected due to the continuously increasing electrode area.

Electrodeposited Cu microstructures are known to exist as composites of Cu, Cu<sub>2</sub>O, and CuO, with Cu<sub>2</sub>O being the dominate species.<sup>201-202</sup> In our work, Raman microscopy indicated that the nanoparticles existed as Cu<sub>2</sub>O, CuO, or Cu nanoparticles for small, intermediate, and large charge densities, respectively (Figure 1d). For electrodeposition on Ti/TiO<sub>x</sub> substrates, size gradients were observed for the nanoparticles, with the size decreasing with increasing distance from the point of contact for the working electrode. This can be attributed to the electrical resistance in the Ti/TiO<sub>x</sub> samples caused by numerous grain boundaries in these amorphous samples, and the various inclusions and defects at the surface. For the smaller nanoparticles, confocal Raman spectra had peaks expected for scattering at phonons in Cu<sub>2</sub>O, at 95, 216, and 420 cm<sup>-1</sup>.<sup>165,203</sup> As the size of the nanoclusters increased, these peaks decreased in intensity and a wave

at  $295\text{ cm}^{-1}$ , indicative of  $\text{CuO}$ ,<sup>204</sup> increased in prominence.  $\text{Cu}_2\text{O}$  and  $\text{CuO}$  have overlapping Raman active phonons at and  $620\text{ cm}^{-1}$ . While an observable spectrum was not obtainable for the sub-10 nm clusters that were deposited in these studies, they are assumed to be largely composed of  $\text{Cu}_2\text{O}$ .

The inhomogeneous nature of the native oxide layer in these samples resulted in conductive  $\text{TiO}$  and  $\text{Ti}_2\text{O}_3$  shunts through the nonconductive  $\text{TiO}_2$  adlayer.  $\text{TiO}$ , in particular, exhibits metallic conduction,<sup>205</sup> but defects at grain boundaries in these samples also provided conductive shunts to the underlying Ti. The examination of numerous  $\text{Ti/TiO}_x$  deposits with AFM allowed visualization of the density of conductive shunts, as evidenced by the presence of nanoparticles (Figure 2). A histogram of the height information obtained in every pixel of the image, or z-range, revealed that the average height increased from 6.83 nm (image not shown), to 20.69 nm, with a maximum height of 115.27 nm.

For the  $\text{TiO}_x/\text{silane}$  samples, a larger density, but smaller size of nanoparticles was observed under identical deposition conditions. Also, their spatial distribution decreased, with closely spaced clusters appearing throughout each AFM image (Figure 3). The average height in this representative image decreased to 13.97 nm, with a maximum of 84.51 nm. These observations can be explained by the silane monolayer acting as a defect-prone dielectric atop the conductive shunts in the electrode, increasing the electrode/electrolyte separation by  $\sim 7\text{ \AA}$ ,<sup>206</sup> the monolayer thickness for 3-APTES. Due to the surface roughness of the  $\text{Ti/TiO}_x$  samples, the silane was expected to have few crosslinkages between monomers and to be characterized by a high defect density. This resulted in a larger number of smaller diameter conductive pinholes through the silane, which were revealed by the location of the nanoparticles. This resulted in closely spaced clusters of smaller  $\text{Cu}_2\text{O}$  nanoparticles, relative to those observed on the  $\text{Ti/TiO}_x$  surface.

While the presence of a silane monolayer inhibited electrodeposition on Ti/TiO<sub>x</sub>, the TiO<sub>x</sub>/silane/SWNT samples had much larger nanoparticles, with many observed to preferentially deposit the sidewalls of the nanotubes (Figure 5.4). The average height observed in a representative image increased from 13.97 for the TiO<sub>x</sub>/silane samples, to 18.85 nm, with a maximum of 111.11 nm. AFM image analysis software allows the estimation of the volume occupied by the nanoclusters by multiplying the distance information obtained for the x, y and z data for each point higher than 1 nm across the surface. As the same charge and electrochemical conditions were used to form these three types of deposits, they are expected to have similar amounts of material deposited, despite their clear differences in morphology. Analyzing the volume occupied by these nanoclusters provides insight into the effect of surface properties on the charge efficiency for deposition on each surface. The volume occupied by deposits for the three surfaces were 1.3, 0.83, and 1.1 μm<sup>3</sup>, for the Ti/TiO<sub>x</sub>, TiO<sub>x</sub>/silane, and TiO<sub>x</sub>/silane/SWNT surfaces, respectively. The decreased amount of nanoclusters on the TiO<sub>x</sub>/silane samples may be attributed in part to strong silane/surface bond disrupting the local oxidation state of the Ti/TiO<sub>x</sub> surface, thus increasing the density of conductive shunts. Also, the silane monolayer increased the distance between the electrolyte/electrode interface. This would effectively decrease the interfacial capacitance and result in the need for greater charging current to achieve the applied electrochemical potential, decreasing the current efficiency for nanoparticle formation. This effect is expected to be lessened for the TiO<sub>x</sub>/silane/SWNT samples since the nanotubes provided a high capacitance electrode through which more efficient electrodeposition could occur. The formation of these conductive nanoclusters presents an important opportunity to reduce the interfacial R caused by the weak attraction between sp<sup>2</sup> hybridized C and metal electrodes. This possibility will be explored in a subsequent section.

### 5.4.2 Electrochemistry of SWNT Networks

In order to investigate the effect of the electrodeposition of nanoparticles on the two-terminal R of networks, an SWNT network was deposited across two Ti/TiO<sub>x</sub> electrodes that were bridged by an insulating glass substrate (Figure 5.5a). This configuration approximates that of the source and drain electrodes found in field-effect transistors. The devices were constructed so that two Ti/TiO<sub>x</sub> electrodes with a combined area of 1.5 cm<sup>2</sup> were separated by a 1.0 cm insulating gap with an area of 2.5 cm<sup>2</sup>. After each sample was silanized, a network composed of similar densities of either partially aligned or crossbar oriented SWNTs was deposited. Finally, electrodeposition at 0.10 V was performed until a total charge of 16.7 mC passed (Figure 5.5b). The aligned network reached this charge at 2,908 s, while the crossbar network required only 2,026 s. Chronoamperometry curves for the two types of networks differed, with the crossbar networks having higher current densities.

At the instant a macroscopic planar electrode is polarized to a potential at which an electroactive species is reduced, there is a spike in current as the electroactive species in the immediate vicinity of the electrode is consumed. Then, the magnitude of the current decays until a steady-state level is reached. This decay in current is described by the Cottrell equation,<sup>207</sup>

$$i = nFACD^{1/2}\pi^{-1/2}t^{-1/2} \quad (1)$$

where  $i$  is current,  $n$  is the number of electrons transferred per electroactive ion or molecule,  $F$  is Faraday's constant,  $A$  is the area of the electrode,  $C$  is the bulk concentration of the electroactive species,  $D$  is its diffusion coefficient, and  $t$  is the time in seconds. This equation demonstrates how the diffusion limited current decays as a function of the inverse square root of time as the other factors are constants. Then, a plot of  $i$  vs.  $t^{-1/2}$  is expected to lead to a linear regression with a current that approaches zero at very long times. Even though the Ti/TiO<sub>x</sub> electrodes are

electrochemically active only at the conductive shunts through the TiO<sub>2</sub> adlayer, at long times (i.e. small values of  $t^{-1/2}$ ) they behaved as planar macroscopic electrodes of an area that included the shunts and insulating part of the surface as the diffusion layers for each conductive shunt grew and overlapped to form one large zone from which the Cu<sup>2+</sup> could diffuse.<sup>208</sup> The slight non-linearity at long times is due to convective currents. However, at short times, the current density was affected by the much smaller diffusion fields that surrounded each conductive shunt, reducing the effective area of the electrode. Also, at short times, capacitive currents (non-Faradaic) contribute significantly to the current response as the volume of electrolyte that contributes to them are much larger than the diffusion layer. However, at longer times, the capacitive currents decay exponentially, while the diffusion layer grows to encompass a larger volume. So at short times, the current essentially represents the combined area of the each isolated shunt, and non-Faradaic processes, while at longer times, the current is more indicative of the diffusion-limited reduction of Cu<sup>2+</sup> at a homogeneous macroscopic planar electrode.

Comparison of the regressions for the SWNT networks and the Ti/TiO<sub>x</sub> electrodes at long times provides a clear indication of the difference in electrochemical performance of the two systems. The Cottrell equation assumes that planar diffusion is the only significant contributor to mass transport. However, the current response of an SWNT array approximates that of an array of interconnected nanoscaled cylindrical nano-electrodes, where hemispherical diffusion dominates. Further, although the entire electrode is conductive, the reduction of Cu<sup>2+</sup> only occurs at electrochemically active defect sites. Therefore, hemispherical diffusion is responsible for mass transport to these isolated active sites. The small potential, relative to the equilibrium potential, applied in these studies resulted in the diffusion-limited regime not being achieved for the networks, resulting in a linear response curves. Unlike the case for planar diffusion at a

macroscopic electrode, hemispherical diffusion is characterized by continuing growth of the diffusion layer, allowing each defect site to draw from an ever-expanding zone of the bulk solution. Then, at long times, convection currents in the solution begin to result in the increase in current observed for  $0 < t^{-1/2} < 1.3 \text{ s}^{-1/2}$ . The effect of convective currents is more pronounced for the SWNT network electrodes because of their ever-expanding diffusion zone. This situation can be described by the equation

$$i = nFACD^{1/2}\pi^{-1/2}t^{-1/2} + 2nFACDr^{-1}\ln(4Dtr^{-2})^{-1} \quad (2)$$

where  $r$  is the radius of the electrode. Then, the first term is important at very short times, when planar diffusion dominated, and the second term describes the steady-state current observed at long times, when hemispherical diffusion dominated. As the radius of the electrode decreases to the nm-regime, the time it takes the second term to dominate, and thus the time to reach a steady state, is very short and a steady state current is observed for much of the plot.

### 5.4.3 Electrochemical Growth of Nanoclusters on SWNT Networks

The reduction of defect density in suspension processed SWNTs is an important consideration for their ultimate use in electronic and structural materials. Recently, Fan and coworkers found that 3.5 M HCl treatments increased sidewall defect density at a rate of  $\sim 1/\mu\text{m/hr}$  for chemical vapor deposition-grown nanotubes, and that suspension processed arc discharge SWNTs had a defect density exceeding 1 per 100 nm, due to the harsh ultrasonication and acid treatments used to suspend and purify the nanotubes.<sup>209</sup> In order to minimize defect density, the arc discharge soot used in these studies was processed using low power ultrasonic agitation for dispersion, followed by iterative centrifugation at low G to separate high aspect ratio SWNTs.<sup>177</sup> This resulted in stable suspensions of high aspect ratio SWNTs having low defect densities, while acid purification methods would have imparted defects that increase electron scattering along the

length of each SWNT, thus increasing  $R$ . Additionally, because defect sites are preferred locations for nanoparticle nucleation on SWNTs, reducing the sidewall defect density increased the spacing between  $\text{Cu}_2\text{O}$  nanoparticles to a level that allowed each to act as a discrete, tunable valve. Therefore, varying the ultrasonication or chemical conditions used during suspension formation presents a powerful opportunity to control the overall density of nanoparticles for other electronic applications. Then, control over the density of SWNTs in the network and their defect density obviates the need to control the location of defect sites. Additionally, inter-SWNT conduction is facilitated by conductive nanoparticles that fortuitously bridge such junctions.

In order to investigate the effect of electrodeposited metal oxide nanoclusters on the  $I_{on}/I_{off}$  of SWNT network-based FETs, standard lithographic methods were used to form Ti/TiO<sub>x</sub> electrodes on Si/SiO<sub>x</sub> substrates, so that the conductive Si could be used as a gate electrode during device testing. Then, Ti/TiO<sub>x</sub> electrodes served as source and drain electrodes that were bridged by SWNT networks. These FETs had a channel length and width of 300 and 100  $\mu\text{m}$ , respectively. While methods for aligning and coating SWNTs with metals have microelectronic applications, the focus of these investigations was the effect of  $\text{Cu}_2\text{O}$  nanoparticles on the semiconductive character of a network composed of a mixture of s- and m-SWNTs. Therefore, a deposition voltage of 0.10 V vs Ag/AgCl and charge flow limits were used to control the size of the nanoparticles. The use of potentials increasingly negative of the equilibrium potential on these Ti/TiO<sub>x</sub> surfaces were found to increase the size of the nanoparticles until they coalesced and completely coated the individual SWNTs comprising the network.

The electrode area was a 1.0 cm diameter disc that encompassed the Ti/TiO<sub>x</sub> electrodes (Figure 5.6a). This was accomplished by mounting each sample in a homemade glass cell that housed the reference and counter electrodes. Then, the electrochemically active area was defined

by the  $\text{TiO}_x$ /silane electrodes and the SWNTs in the macroscopic network that bridged the electrodes. A deposition charge of 16.7 mC resulted in the growth of nanoparticles on the SWNTs within the network that bridged the source/drain channel (Figure 5.6b). Although they are highly conductive like metals, the sidewalls of SWNTs are generally inert toward electrochemical deposition of adsorbates. Therefore, deposits general form via nucleation and growth at defects at the ends and sidewalls of the nanotubes. On graphite, this type of preferential nucleation at defects has been attributed to the higher coordination provided by oxygen-containing defects.<sup>210</sup> For SWNTs, the nanoclusters nucleated at defects, and then grew into nm-sized clusters having their size predetermined by the amount of electrochemical charge allowed to pass. Therefore, van der Waals attractions existed between the nanoclusters and sidewalls, while a stronger bond, possibly containing a significant degree of covalent character, existed between the defect and nanoclusters.

The average height observed for AFM images of unbundled arc discharge SWNTs is 1.4 nm.<sup>177</sup> The average height observed 200  $\mu\text{m}$  from the  $\text{TiO}_x$ /SWNT network interface to  $8.5 \pm 0.3$  nm. The average size of the nanoparticles decreased to  $7.3 \pm 0.2$  nm at 2,000  $\mu\text{m}$  from the  $\text{TiO}_x$ /SWNT network interface. Such a gradient in nanoparticle size is typically observed in SWNT networks,<sup>211-212</sup> as the SWNTs acts as a collection of low-R wires, with high R at each inter-SWNT junction causing a drop in the electrochemical potential with distance. Nanoparticle growth was not observed on isolated SWNTs or the silica substrate, indicating that electrodeposition is an effective manner to preferentially modify the SWNTs in a conductive network.

#### **5.4.4 Effect of $\text{Cu}_2\text{O}$ Nanoparticles on Electrical Resistance**

To determine the effect of  $\text{Cu}_2\text{O}$  nanoparticles on R for low-density networks of unbundled SWNTs, R was measured by obtaining I/V curves in air, for the range  $\pm 0.3$  V, using a

semiconductor characterization unit. For all electrochemical experiments involving FETs, the amount of Cu<sub>2</sub>O deposited was limited by controlling the total charge allowed to flow before the cell was returned to  $V_{rev.}$ , and the sample removed from the cell. Control experiments, where R was measured before and after samples were immersed in the electrochemical cell and held at potentials near or slightly positive of the  $V_{rev.}$  for Cu resulted in no appreciable change in two-terminal R or FET response. However, the magnitude of R was observed to decrease with decreasing deposition potential. Two-point probe R measurements were used, as this configuration closely resembles that of the measurements for the FETs described below.

The change in R was strongly affected by the overall alignment of the SWNTs in the network. For a deposition potential of 0.1 V vs. Ag/AgCl, the average R decreased from  $1.14 \pm 0.09$  to  $0.75 \pm 0.06$  M $\Omega$  for the “aligned” samples when a deposition potential of 0.1 V was used. This represents a 34% decrease in R. The average R decreased from  $1.3 \pm 0.1$  to  $0.63 \pm 0.06$  M $\Omega$  for the “crossbar” samples, corresponding to a 52% reduction in R. The increased response of the crossbar samples can be attributed to the greater number of inter-SWNT junctions.

Part of the reduction in R for both levels of alignment is attributed to the formation of ohmic contacts between s- and m-SWNTs in the network when nanoparticles bridged those junctions, reducing the Schottky barrier between the two types of conductors. When high aspect ratio SWNTs were oriented orthogonally, the number of junctions increased significantly. This allowed greater gains in conductivity. The effect of the density of the nanoclusters on the two-terminal R and FET performance of both types of networks is currently under investigation, but it is expected that performance gains will decrease as the density of defects on the SWNTs increases, since sidewall defects impede current flow in nanotubes.

#### 5.4.5 Effect of Cu<sub>2</sub>O Nanoparticles on SWNT Network Field-Effect Transistors

When the performance of “aligned” and “crossbar” samples were examined in FETs, the “aligned” samples had increased performance gains with respect to  $I_{on}/I_{off}$ . The magnitude of  $I_{on}$  and  $I_{off}$  were determined at -5 and +5 V, respectively. For the representative devices in Figure 5.7, a deposition charge of 2 mC was accompanied by a slight increase in  $I_{on}$  and a dramatic decrease in  $I_{off}$ . The highest increase in  $I_{on}/I_{off}$  was observed for “aligned” networks, as it increased from 5 to 1057, representing a 211-fold increase in  $I_{on}/I_{off}$ . The “crossbar” networks had a significantly greater initial R, and  $I_{on}/I_{off}$  changed from 16 to 561, representing a 35-fold increase. At higher electrochemical charge densities, both the two-terminal R and  $I_{on}/I_{off}$  decreased, as the transistor response exhibited increasing metallic behavior for both types of networks. It was also notable that the initial R was higher for “crossbar” networks, although the density of nanotubes for the two networks was similar. This can be attributed to the fewer junctions that have to be traversed during electron transport if the SWNTs are partially aligned. This facilitated greater gains in two-terminal R for “crossbar” networks after nanoparticle deposition (Figure 5.7a, b, insets).

As un-separated SWNTs have a distribution of 1/3<sup>rd</sup> metallic and 2/3<sup>rd</sup> semiconductive, low density networks of unbundled nanotubes behave as semiconductors due to the lack of metallic pathways in the network. However, at the higher densities used in these studies, metallic SWNTs formed short circuit pathways that greatly reduced the initial  $I_{on}/I_{off}$  of SWNT network transistors. Then, the OFF-state current was indicative of the number of metallic pathways through the film. Therefore, starting with FETs that exhibited a low initial  $I_{on}/I_{off}$  allowed confirmation of the fact that Cu<sub>2</sub>O nanoparticle deposition increased the  $V_g$  sensitivity of the m-SWNTs in the conductive pathways.

It is possible to controllably open a bandgap in m-SWNTs since they are not true metals, in fact semimetals or zero band gap semiconductors, like graphene. Since graphene is a 2-dimensional material, efforts to open a band gap in it have centered on reducing its one of its lateral dimensions and/or functionalizing its edges.<sup>213-215</sup> However, the 1-dimensional nature of SWNTs simplifies the process of band gap opening and tuning. The ability to induce quantum confinement effects, by the electrodeposition of Cu<sub>2</sub>O nanoparticles, which increase sensitivity to V<sub>g</sub> essentially inserts a controllable valve along a conducting wire. Therefore, while much of the SWNT continues to exhibit high conductivity in the presence of positive values of V<sub>g</sub>, electrical transport is stopped near the nanoparticles, as expected for a p-type semiconductor. The mechanism of this involves the local depletion of electron density within a few nm of the Cu<sub>2</sub>O nanoclusters, due to their high work function.

The great increase in  $I_{on}/I_{off}$  for both types of networks indicated that metallic short circuit pathways in the networks were converted to semiconductive, as much of the increase in  $I_{on}/I_{off}$  occurred via a greatly reduced  $I_{off}$  for FETs that initially showed little response to V<sub>g</sub>. This indicated that at positive values of V<sub>g</sub>, the Cu<sub>2</sub>O adsorbates opened a band gap in m-SWNTs, and small band gap s-SWNTs, by locally withdrawing electron density. This would effectively allow each nanoparticle/SWNT contact to act as a nanoscale valve that could be closed at positive values of V<sub>g</sub>, allowing much lower magnitudes of  $I_{on}/I_{off}$  to be achieved.

Scanned gate microscopy studies have indicated that point defects along m-SWNTs led to resonant electron scattering that resulted in moderate sensitivity of the conductance of unmodified nanotubes to changes in V<sub>g</sub>.<sup>216</sup> Further, the conductivity through defects in unmodified m-SWNTs has been shown to exhibit local gate dependence. In the work described herein, local gating effect at defects on m-SWNTs was enhanced by the high work function Cu<sub>2</sub>O adsorbates. Therefore,

when  $\text{Cu}_2\text{O}$  nanoparticles were deposited on m-SWNTs, the modification of the density of electronic states near the defect opened a band gap in the otherwise metallic nanotubes causing a decrease in  $I_{off}$  at positive values of  $V_g$ .

## 5.5 Conclusions

Forming SWNT networks on prefabricated metal electrodes using liquid deposition methods provides a facile route to device assembly. This device geometry also facilitated the use of electrochemical methods to enhance the interfacial electron transport by the formation of chemisorbed  $\text{Cu}_2\text{O}$  shunts through a silane monolayer to the conductive underlying Ti. This provides greatly improved connections, compared to the weak van der Waals contacts that exist at unmodified metal/SWNT interfaces. As self-assembled monolayers (SAMs) composed of silane are used as adhesion layers on  $\text{SiO}_x$  surfaces, the use of metal electrodes that are terminated with a thin oxide layer allows the formation of a single silane monolayer that coats the entire surface. Then, after network formation, electrochemical methods were used to optimize the electrical properties of the thin films.

For SWNT network FETs,  $I_{on}$  was improved by reducing R at inter-SWNT junctions and at interfacial contacts between the nanotubes and metal. Metal oxide nanoclusters were electrodeposited onto the SWNT sidewalls resulting in the formation of numerous valves that allowed a much-enhanced response of the network to  $V_g$ . This has great potential to increase the operating efficiency of SWNT network-based electronic device structures, as less expensive gate dielectrics can be used when the sensitivity to  $V_g$  is increased. This approach also reduces the effect of metallic SWNTs in networks without the need for expensive processing steps to separate them based on their type of conductivity.

## 5.6 Acknowledgements

The authors gratefully acknowledge financial support from the National Science Foundation through the Center for Nanostructured Electronic Materials, a Phase I Center for Chemical Innovation (NSF grant CHE-1038015) and NSF Grant Number DMR-0906564.

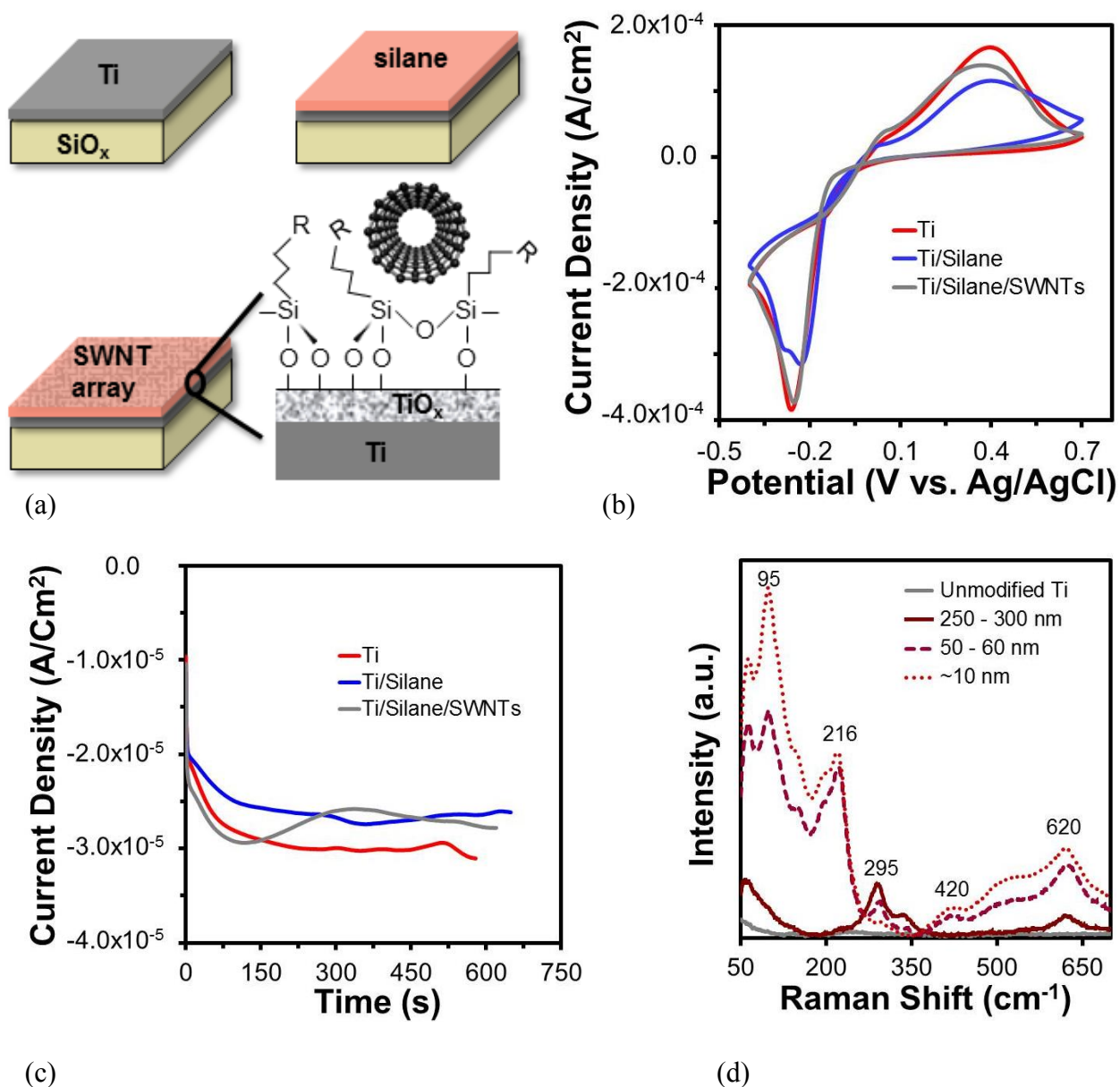


**Figure 5.1.** Electrochemical samples consisted of (a) Ti/ $\text{TiO}_x$ ,  $\text{TiO}_x$ /silane, or  $\text{TiO}_x$ /silane/SWNT samples of equal surface area; (b) representative cyclic voltammograms of the three surfaces showed enhanced reductive currents for the  $\text{TiO}_x$ /silane/SWNT surfaces, relative to the  $\text{TiO}_x$ /silane samples, indicating that the SWNTs facilitated the reduction of Cu; (c)  $i$  vs.  $t$  traces obtained at a constant potential of 0.10 V vs. Ag/AgCl, for a total of 16.7 mC of charge, displayed a sigmoidal shape for the  $\text{TiO}_x$ /silane/SWNT samples, indicative of enhanced instantaneous and

progressive nucleation processes; (d) Raman microscopy of revealed that the Cu species varied with the nanoparticle size.

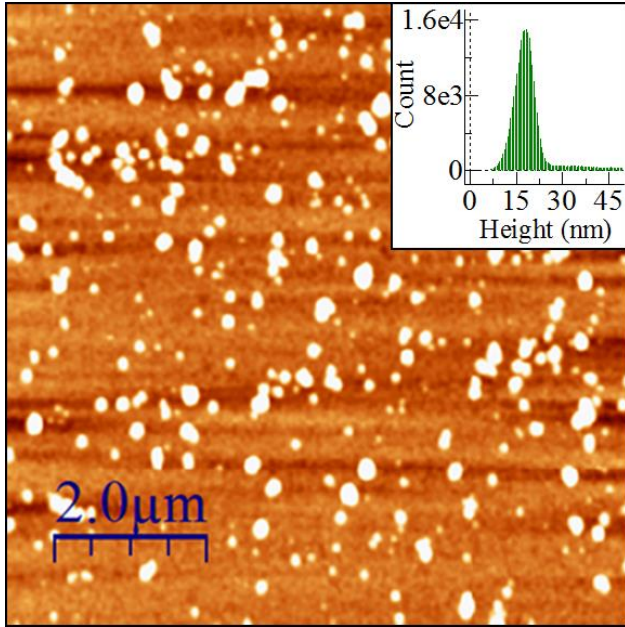


**Figure 5.2.** Representative AFM micrograph ( $8 \times 8 \mu\text{m}$ ) showing nanoparticle growth on the Ti/TiO<sub>x</sub> surface after deposition at 0.10 V for a charge of 16.7 mC. Each nanoparticle reveals the location of a conductive pinhole (low valence Ti oxide, or conductive grain boundary) through the dielectric TiO<sub>2</sub> surface.

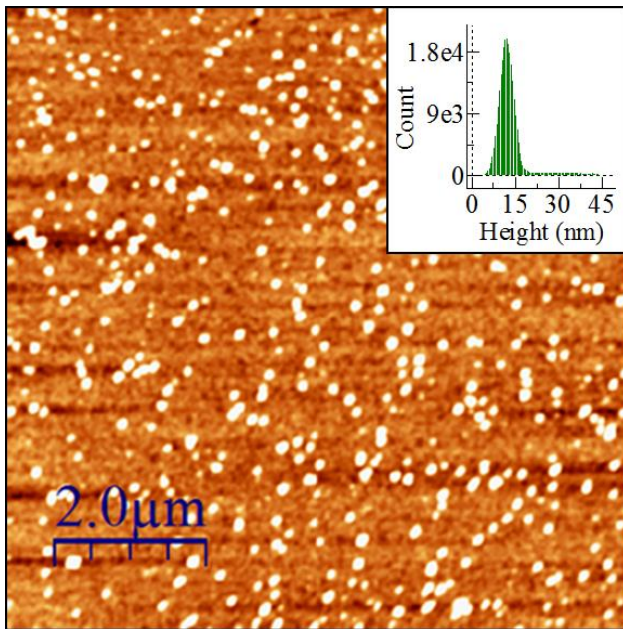


**Figure 5.3.** Representative AFM image ( $8 \times 8 \mu\text{m}$ ) of the  $\text{TiO}_x/\text{silane}$  samples showing how the addition of a silane monolayer resulted in smaller and more closely clustered nanoparticles than those observed on the  $\text{Ti}/\text{TiO}_x$  surface.

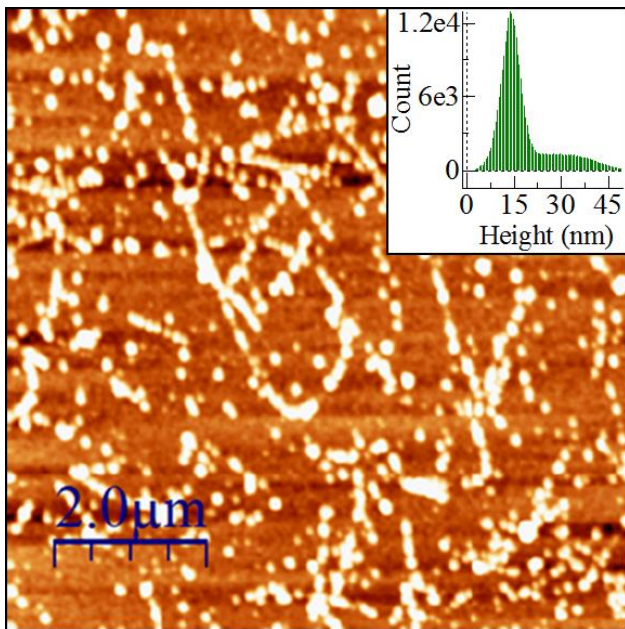


**Figure 5.4.** This representative AFM image ( $8 \times 8 \mu\text{m}$ ) of a  $\text{TiO}_x/\text{silane}/\text{SWNT}$  sample shows that the deposition of a low-density network of SWNTs provided nucleation points for  $\text{Cu}_2\text{O}$  along the conductive sidewalls of the nanotubes, as observed from the greatly increased density of nanoparticles observed. This presents a unique opportunity to decrease the interfacial R at SWNT/metal electrode interfaces.

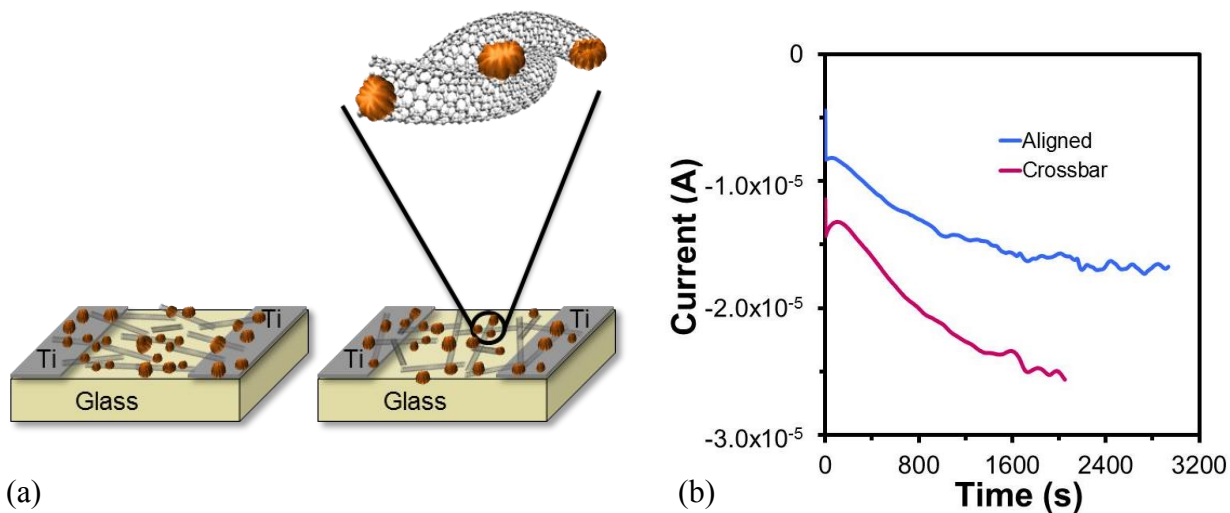
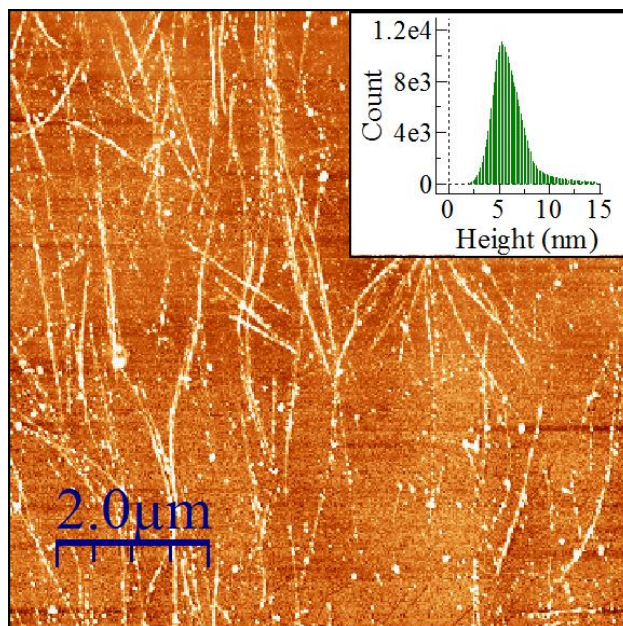
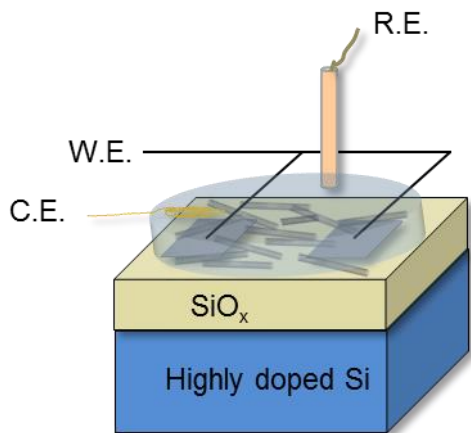


**Figure 5.5.** (a) The effect of Cu nanoparticle deposition on the two terminal R of aligned (left), and crossbar (right) networks (schematic, not drawn to scale); (b) representative  $i$  vs.  $t$  curves for the two types of networks showed that when the charge allowed to pass was limited to 16.7 mC, the higher current densities for the crossbar networks caused them to achieve that value at significantly shorter times.



(a)

(b)

**Figure 5.6.** (a) The source/drain electrode pair, and the SWNT network between, served as the working electrode during the electrodeposition of various amounts of  $\text{Cu}_2\text{O}$  nanoparticles at 0.10 V vs. Ag/AgCl. The charge was used to tune the amount of metallization that occurred; (b) sub-10 nm sized  $\text{Cu}_2\text{O}$  nanoparticles were consistently observed on the SWNTs that bridged the source/drain channel between the Ti/ $\text{TiO}_x$  electrodes.

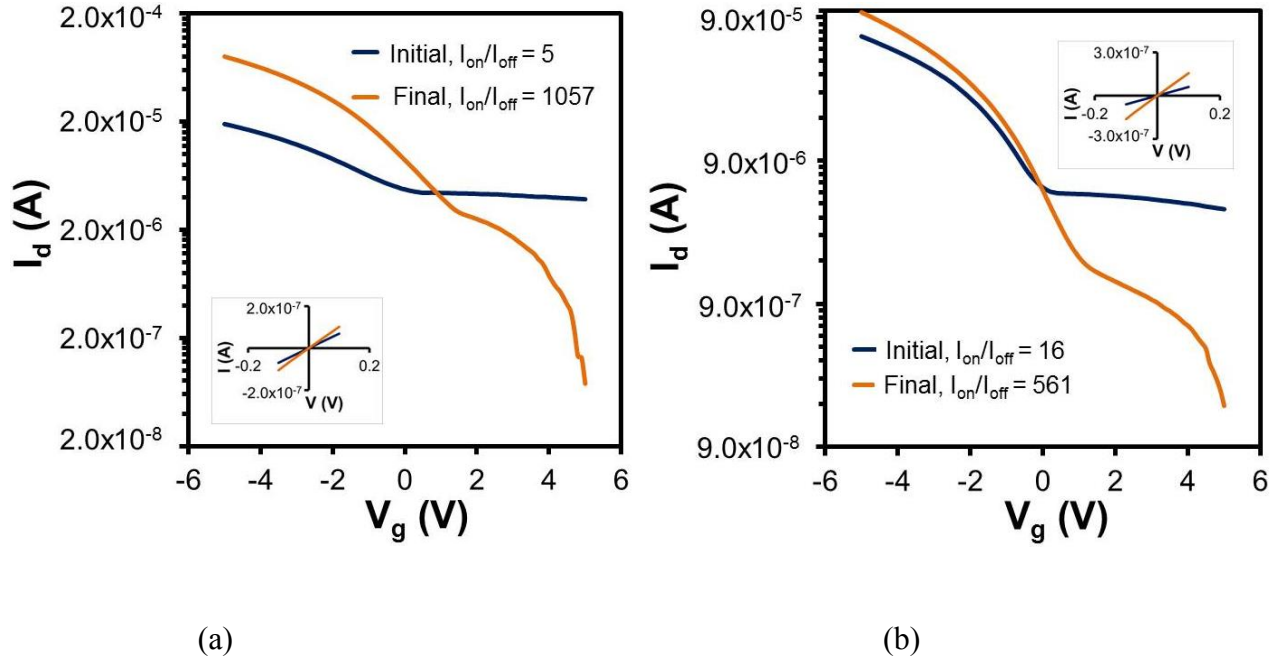


**Figure 5.7.** Representative log plots showing the dependence of the change in  $I_{on}/I_{off}$  on the alignment of SWNTs comprising the network revealed that (a) partially aligned SWNTs allowed for reduced R and greater improvements in  $I_{on}/I_{off}$  than (b) orthogonally oriented SWNTs, as the increase in  $I_{on}/I_{off}$  observed was 211- and 35-fold, respectively. Insets: two-terminal  $i$  vs,  $V$  curves obtained in the range  $\pm 0.10$  V showed that a greater reduction in R was achieved for “crossbar” networks.

## CHAPTER 6

### CONCLUSIONS AND FUTURE WORK

#### 6.1 Conclusions

The technique of touchspinning was developed to spin fibers from almost any degradable or synthetic polymer solution and melt. The fibers fabricated by touchspinning exhibited a higher degree of crystallinity over the fibers made by conventional electrospinning. The enhanced physical, chemical, and mechanical properties of the touchspun aligned nanofibers was compared to those of electrospun fibers. Specifically, the crystallinity of the touchspun PCL nanofiber was much higher than that of electrospun fibers. Incorporated BSA within the touchspun fibers increased the expression of neuron-specific class III  $\beta$ -tubulin compared to other scaffolds. More importantly, the aligned PCL touchspun nanofibers promoted aligned neurite outgrowth of NSCs, suggesting its potential utility in treating conditions ranging from spinal cord injury to peripheral nerve lesions.

In electrospinning, the electrical force depends on the distance from the charged needle to the pendent droplet. Hypothetically, the touchspinning process resembles the cold-drawing method resulting in higher degree of crystallinity. In touchspinning, the rods on the spinneret apply a mechanical force to the pendent droplet and the force is uniformly and continuously applied to the entire length of the fiber during the fiber fabrication stage. In contrast, in electrospinning, the electrical force is being applied to a local point on the pendent droplet and the force is not uniformly applied to the points along the fiber since the electrical force depends on the distance from the charged needle. The high degree of crystallinity and high Young's modulus make the

touchspun nanofibrous scaffolds a promising candidate for the nerve regeneration applications compared to the electrospun scaffolds.

In addition, a new fiber spinning technique named gravitational-spinning was introduced as a modified dry-spinning method that allows for drawing free standing single ultralong micro- and nanofibers for various biomedical, photonics, and textile applications. In the previous drawing techniques, the pulling speed was not efficient for manufacturing productivity, however, gravitational-spinning is capable of producing ultralong nanofibers in fraction of second. The productivity would be enhanced if more nozzles are available to eject polymer droplets. Furthermore, almost all of the polymer solutions and melts can be used in this technique for fiber spinning and the single nanofibers can precisely be placed on the surface of the substrate during fabrication.

Also, electrochemical decoration of single-walled carbon nanotubes (SWNT) resulted in higher performance of the field-effect transistors. The silane was deposited on the surface of the electrode for better adhesion of SWNTs to the electrode. This device geometry also facilitated the use of electrochemical methods to enhance the interfacial electron transport by the formation of chemisorbed  $\text{Cu}_2\text{O}$  shunts through a silane monolayer to the conductive underlying Ti. This resulted in greatly improved connections, compared to the weak van der Waals contacts that exist at unmodified metal/SWNT interfaces. For SWNT network FETs,  $I_{on}$  was improved by reducing the contact resistance at inter-SWNT junctions and at interfacial contacts between the nanotubes and metal. Metal oxide nanoclusters were electrodeposited onto the SWNT sidewalls resulting in the formation of numerous valves that allowed a much-enhanced response of the network to gate potential. This has great potential to increase the operating efficiency of SWNT network-based electronic device structures. This approach also reduces the effect of metallic SWNTs in networks

without the need for expensive processing steps to separate them based on their type of conductivity.

## 6.2 Future Work

Regarding the effect of BSA on the neural differentiation more analysis is needed to figure out the activity of BSA in chloroform before and after fiber spinning using two techniques of touchspinning and electrospinning. The results from circular dichroism, UV-vis, SDS-PAGE, and FTIR might show better understanding of the effect of BSA on neural differentiation. BSA solution before and after electrospinning need to be analyzed via UV-vis and circular dichroism to figure out whether the high voltage denatured BSA or not. Also, contact angle measurements may give a better understanding about the location of BSA in the fiber. Since BSA is hydrophilic and PCL is hydrophobic, the contact angle may differ on these two surfaces, therefore, better understanding of the surface will be obtained.

## REFERENCES

1. Nguyen, L. T.; Chen, S.; Elumalai, N. K.; Prabhakaran, M. P.; Zong, Y.; Vijila, C.; Allakhverdiev, S. I.; Ramakrishna, S., Biological, chemical, and electronic applications of nanofibers. *Macromolecular materials and engineering* **2013**, *298* (8), 822-867.
2. Huang, Z.-M.; Zhang, Y.-Z.; Kotaki, M.; Ramakrishna, S., A review on polymer nanofibers by electrospinning and their applications in nanocomposites. *Composites science and technology* **2003**, *63* (15), 2223-2253.
3. Leung, V.; Ko, F., Biomedical applications of nanofibers. *Polymers for Advanced Technologies* **2011**, *22* (3), 350-365.
4. Thavasi, V.; Singh, G.; Ramakrishna, S., Electrospun nanofibers in energy and environmental applications. *Energy & Environmental Science* **2008**, *1* (2), 205-221.
5. Feng, C.; Khulbe, K.; Matsuura, T., Recent progress in the preparation, characterization, and applications of nanofibers and nanofiber membranes via electrospinning/interfacial polymerization. *Journal of applied polymer science* **2010**, *115* (2), 756-776.
6. Mirjalili, M.; Zohoori, S., Review for application of electrospinning and electrospun nanofibers technology in textile industry. *Journal of Nanostructure in Chemistry* **2016**, *6* (3), 207-213.
7. Yang, F.; Murugan, R.; Wang, S.; Ramakrishna, S., Electrospinning of nano/micro scale poly (L-lactic acid) aligned fibers and their potential in neural tissue engineering. *Biomaterials* **2005**, *26* (15), 2603-2610.
8. Liu, W.; Thomopoulos, S.; Xia, Y., Electrospun nanofibers for regenerative medicine. *Advanced healthcare materials* **2012**, *1* (1), 10-25.
9. Ramakrishna, S.; Fujihara, K.; Teo, W.-E.; Yong, T.; Ma, Z.; Ramaseshan, R., Electrospun nanofibers: solving global issues. *Materials today* **2006**, *9* (3), 40-50.
10. El-Newehy, M. H.; El-Naggar, M. E.; Alotaiby, S.; El-Hamshary, H.; Moydeen, M.; Al-Deyab, S., Green Electrospinning of Hydroxypropyl Cellulose Nanofibres for Drug Delivery Applications. *Journal of Nanoscience and Nanotechnology* **2018**, *18* (2), 805-814.
11. Weng, L.; Xie, J., Smart electrospun nanofibers for controlled drug release: recent advances and new perspectives. *Current pharmaceutical design* **2015**, *21* (15), 1944-1959.
12. Chen, T.; Qiu, L.; Cai, Z.; Gong, F.; Yang, Z.; Wang, Z.; Peng, H., Intertwined aligned carbon nanotube fiber based dye-sensitized solar cells. *Nano letters* **2012**, *12* (5), 2568-2572.
13. Zhu, Z.; Garcia-Gancedo, L.; Flewitt, A. J.; Moussy, F.; Li, Y.; Milne, W. I., Design of carbon nanotube fiber microelectrode for glucose biosensing. *Journal of Chemical Technology and Biotechnology* **2012**, *87* (2), 256-262.
14. Ballengee, J. B.; Pintauro, P. N., Composite fuel cell membranes from dual-nanofiber electrospun mats. *Macromolecules* **2011**, *44* (18), 7307-7314.
15. Neubert, S.; Pliszka, D.; Thavasi, V.; Wintermantel, E.; Ramakrishna, S., Conductive electrospun PANi-PEO/TiO<sub>2</sub> fibrous membrane for photo catalysis. *Materials Science and Engineering: B* **2011**, *176* (8), 640-646.

16. Luo, C.; Stoyanov, S. D.; Stride, E.; Pelan, E.; Edirisinghe, M., Electrospinning versus fibre production methods: from specifics to technological convergence. *Chemical Society Reviews* **2012**, *41* (13), 4708-4735.
17. Bhardwaj, N.; Kundu, S. C., Electrospinning: a fascinating fiber fabrication technique. *Biotechnology advances* **2010**, *28* (3), 325-347.
18. Andreu, V.; Mendoza, G.; Arruebo, M.; Irusta, S., Smart Dressings Based on Nanostructured Fibers Containing Natural Origin Antimicrobial, Anti-Inflammatory, and Regenerative Compounds. *Materials* **2015**, *8* (8), 5154-5193.
19. Jain, A.; Betancur, M.; Patel, G. D.; Valmikinathan, C. M.; Mukhatyar, V. J.; Vakharia, A.; Pai, S. B.; Brahma, B.; MacDonald, T. J.; Bellamkonda, R. V., Guiding intracortical brain tumour cells to an extracortical cytotoxic hydrogel using aligned polymeric nanofibres. *Nature materials* **2014**, *13* (3), 308-316.
20. Borjigin, M.; Eskridge, C.; Niamat, R.; Strouse, B.; Bialk, P.; Kmiec, E. B., Electrospun fiber membranes enable proliferation of genetically modified cells. *Int J Nanomedicine* **2013**, *8*, 855-64.
21. Liu, W.; Thomopoulos, S.; Xia, Y., Electrospun nanofibers for regenerative medicine. *Adv Healthc Mater* **2012**, *1* (1), 10-25.
22. Lee, S. J.; Nowicki, M.; Harris, B.; Zhang, L. G., Fabrication of a Highly Aligned Neural Scaffold via a Table Top Stereolithography 3D Printing and Electrospinning. *Tissue Eng Part A* **2017**.
23. Zhu, W.; Masood, F.; O'Brien, J.; Zhang, L. G., Highly aligned nanocomposite scaffolds by electrospinning and electrospraying for neural tissue regeneration. *Nanomedicine* **2015**, *11* (3), 693-704.
24. Yoshimoto, H.; Shin, Y.; Terai, H.; Vacanti, J., A biodegradable nanofiber scaffold by electrospinning and its potential for bone tissue engineering. *Biomaterials* **2003**, *24* (12), 2077-2082.
25. Shin, M.; Yoshimoto, H.; Vacanti, J. P., In vivo bone tissue engineering using mesenchymal stem cells on a novel electrospun nanofibrous scaffold. *Tissue engineering* **2004**, *10* (1-2), 33-41.
26. Grayson, W. L.; Chao, P. H. G.; Marolt, D.; Kaplan, D. L.; Vunjak-Novakovic, G., Engineering custom-designed osteochondral tissue grafts. *Trends Biotechnol.* **2008**, *26* (4), 181-189.
27. Tsang, V. L.; Bhatia, S. N., Three-dimensional tissue fabrication. *Adv. Drug Deliv. Rev.* **2004**, *56* (11), 1635-1647.
28. Papkov, D.; Zou, Y.; Andalib, M. N.; Goponenko, A.; Cheng, S. Z. D.; Dzenis, Y. A., Simultaneously Strong and Tough Ultrafine Continuous Nanofibers. *Acs Nano* **2013**, *7* (4), 3324-3331.
29. McCulloch, W., The history of the development of melt blowing technology. *International Nonwovens Journal* **1999**, *8* (1), 66-72.
30. Bonyadi, S.; Chung, T. S.; Krantz, W. B., Investigation of corrugation phenomenon in the inner contour of hollow fibers during the non-solvent induced phase-separation process. *Journal of membrane science* **2007**, *299* (1-2), 200-210.
31. Hartgerink, J. D.; Beniash, E.; Stupp, S. I., Self-assembly and mineralization of peptide-amphiphile nanofibers. *Science* **2001**, *294* (5547), 1684-1688.
32. Hooper, J. P. Centrifugal spinneret. US1500931 A, 1924.

33. Nayak, R.; Padhye, R.; Kyratzis, I. L.; Truong, Y.; Arnold, L., Recent advances in nanofibre fabrication techniques. *Textile Research Journal* **2011**, 0040517511424524.
34. Cooley, J. F., Apparatus for electrically dispersing fluids. Google Patents: 1902.
35. Morton, W. J., Method of dispersing fluids. Google Patents: 1902.
36. Anton, F., Process and apparatus for preparing artificial threads. Google Patents: 1934.
37. Li, D.; Xia, Y., Electrospinning of nanofibers: reinventing the wheel? *Advanced materials* **2004**, *16* (14), 1151-1170.
38. Doshi, J.; Reneker, D. H. In *Electrospinning process and applications of electrospun fibers*, Industry Applications Society Annual Meeting, 1993., Conference Record of the 1993 IEEE, IEEE: 1993; pp 1698-1703.
39. Williamson, M. R.; Black, R.; Kielty, C., PCL-PU composite vascular scaffold production for vascular tissue engineering: Attachment, proliferation and bioactivity of human vascular endothelial cells. *Biomaterials* **2006**, *27* (19), 3608-3616.
40. Pham, Q. P.; Sharma, U.; Mikos, A. G., Electrospinning of polymeric nanofibers for tissue engineering applications: a review. *Tissue engineering* **2006**, *12* (5), 1197-1211.
41. Sarkar, K.; Gomez, C.; Zambrano, S.; Ramirez, M.; de Hoyos, E.; Vasquez, H.; Lozano, K., Electrospinning to forcespinning™. *Materials Today* **2010**, *13* (11), 12-14.
42. Persano, L.; Camposeo, A.; Tekmen, C.; Pisignano, D., Industrial upscaling of electrospinning and applications of polymer nanofibers: a review. *Macromolecular Materials and Engineering* **2013**, *298* (5), 504-520.
43. van de Weert, M.; Hennink, W. E.; Jiskoot, W., Protein instability in poly (lactic-co-glycolic acid) microparticles. *Pharmaceutical research* **2000**, *17* (10), 1159-1167.
44. Yang, Y.; Li, X.; Qi, M.; Zhou, S.; Weng, J., Release pattern and structural integrity of lysozyme encapsulated in core-sheath structured poly(DL-lactide) ultrafine fibers prepared by emulsion electrospinning. *Eur J Pharm Biopharm* **2008**, *69* (1), 106-16.
45. Casper, C. L.; Yamaguchi, N.; Kiick, K. L.; Rabolt, J. F., Functionalizing electrospun fibers with biologically relevant macromolecules. *Biomacromolecules* **2005**, *6* (4), 1998-2007.
46. Ellison, C. J.; Phatak, A.; Giles, D. W.; Macosko, C. W.; Bates, F. S., Melt blown nanofibers: Fiber diameter distributions and onset of fiber breakup. *Polymer* **2007**, *48* (11), 3306-3316.
47. Podgórski, A.; Bałazy, A.; Gradoń, L., Application of nanofibers to improve the filtration efficiency of the most penetrating aerosol particles in fibrous filters. *Chemical Engineering Science* **2006**, *61* (20), 6804-6815.
48. Brang, J.; Wilkie, A.; Haggard, J., Method and apparatus for production of meltblown nanofibers. Google Patents: 2007.
49. Postema, A.; Luiten, A.; Pennings, A., High-strength poly (L-lactide) fibers by a dry-spinning/hot-drawing process. I. Influence of the ambient temperature on the dry-spinning process. *Journal of applied polymer science* **1990**, *39* (6), 1265-1274.
50. Cong, H.-P.; Ren, X.-C.; Wang, P.; Yu, S.-H., Wet-spinning assembly of continuous, neat, and macroscopic graphene fibers. *Scientific reports* **2012**, *2*, 613.
51. Qin, J.-J.; Gu, J.; Chung, T.-S., Effect of wet and dry-jet wet spinning on the shear-induced orientation during the formation of ultrafiltration hollow fiber membranes. *Journal of Membrane Science* **2001**, *182* (1-2), 57-75.
52. Nain, A. S.; Wong, J. C.; Amon, C.; Sitti, M., Drawing suspended polymer micro-/nanofibers using glass micropipettes. *Applied Physics Letters* **2006**, *89* (18), 183105.

53. Tokarev, A.; Asheghali, D.; Griffiths, I. M.; Trotsenko, O.; Gruzd, A.; Lin, X.; Stone, H. A.; Minko, S., Touch-and Brush-Spinning of Nanofibers. *Advanced Materials* **2015**, *27* (41), 6526-6532.
54. Muthiah, P.; Hsu, S.-H.; Sigmund, W., Coaxially Electrospun PVDF–Teflon AF and Teflon AF–PVDF Core–Sheath Nanofiber Mats with Superhydrophobic Properties. *Langmuir* **2010**, *26* (15), 12483-12487.
55. Scheffler, R.; Bell, N. S.; Sigmund, W., Electrospun Teflon AF fibers for superhydrophobic membranes. *Journal of Materials Research* **2010**, *25* (08), 1595-1600.
56. Amini, A. R.; Laurencin, C. T.; Nukavarapu, S. P., Bone tissue engineering: recent advances and challenges. *Critical Reviews™ in Biomedical Engineering* **2012**, *40* (5).
57. Ratheesh, G.; Venugopal, J. R.; Chinappan, A.; Ezhilarasu, H.; Sadiq, A.; Ramakrishna, S., 3D fabrication of polymeric scaffolds for regenerative therapy. *ACS Biomaterials Science & Engineering* **2017**, *3* (7), 1175-1194.
58. Bose, S.; Vahabzadeh, S.; Bandyopadhyay, A., Bone tissue engineering using 3D printing. *Materials today* **2013**, *16* (12), 496-504.
59. Khorshidi, S.; Solouk, A.; Mirzadeh, H.; Mazinani, S.; Lagaron, J. M.; Sharifi, S.; Ramakrishna, S., A review of key challenges of electrospun scaffolds for tissue-engineering applications. *Journal of tissue engineering and regenerative medicine* **2016**, *10* (9), 715-738.
60. Guo, B.; Sun, Y.; Finne-Wistrand, A.; Mustafa, K.; Albertsson, A.-C., Electroactive porous tubular scaffolds with degradability and non-cytotoxicity for neural tissue regeneration. *Acta biomaterialia* **2012**, *8* (1), 144-153.
61. Ashammakhi, N.; Ndreu, A.; Nikkola, L.; Wimpenny, I.; Yang, Y., Advancing tissue engineering by using electrospun nanofibers. **2008**.
62. Pham, Q. P.; Sharma, U.; Mikos, A. G., Electrospun poly ( $\epsilon$ -caprolactone) microfiber and multilayer nanofiber/microfiber scaffolds: characterization of scaffolds and measurement of cellular infiltration. *Biomacromolecules* **2006**, *7* (10), 2796-2805.
63. Barnes, C. P.; Sell, S. A.; Boland, E. D.; Simpson, D. G.; Bowlin, G. L., Nanofiber technology: designing the next generation of tissue engineering scaffolds. *Advanced drug delivery reviews* **2007**, *59* (14), 1413-1433.
64. Cunha-Reis, C.; TuzlaKoglu, K.; Baas, E.; Yang, Y.; El Haj, A.; Reis, R., Influence of porosity and fibre diameter on the degradation of chitosan fibre-mesh scaffolds and cell adhesion. *Journal of Materials Science: Materials in Medicine* **2007**, *18* (2), 195-200.
65. Agarwal, S.; Wendorff, J. H.; Greiner, A., Progress in the field of electrospinning for tissue engineering applications. *Advanced Materials* **2009**, *21* (32-33), 3343-3351.
66. Eichhorn, S. J.; Sampson, W. W., Statistical geometry of pores and statistics of porous nanofibrous assemblies. *Journal of the royal society Interface* **2005**, *2* (4), 309-318.
67. Zou, B.; Liu, Y.; Luo, X.; Chen, F.; Guo, X.; Li, X., Electrospun fibrous scaffolds with continuous gradations in mineral contents and biological cues for manipulating cellular behaviors. *Acta biomaterialia* **2012**, *8* (4), 1576-1585.
68. Phipps, M. C.; Clem, W. C.; Grunda, J. M.; Clines, G. A.; Bellis, S. L., Increasing the pore sizes of bone-mimetic electrospun scaffolds comprised of polycaprolactone, collagen I and hydroxyapatite to enhance cell infiltration. *Biomaterials* **2012**, *33* (2), 524-534.
69. Ju, Y. M.; San Choi, J.; Atala, A.; Yoo, J. J.; Lee, S. J., Bilayered scaffold for engineering cellularized blood vessels. *Biomaterials* **2010**, *31* (15), 4313-4321.

70. Nisbet, D.; Forsythe, J. S.; Shen, W.; Finkelstein, D.; Horne, M. K., A review of the cellular response on electrospun nanofibers for tissue engineering. *Journal of biomaterials applications* **2009**, *24* (1), 7-29.
71. Rnjak-Kovacina, J.; Weiss, A. S., Increasing the pore size of electrospun scaffolds. *Tissue Engineering Part B: Reviews* **2011**, *17* (5), 365-372.
72. Schindelin, J.; Arganda-Carreras, I.; Frise, E.; Kaynig, V.; Longair, M.; Pietzsch, T.; Preibisch, S.; Rueden, C.; Saalfeld, S.; Schmid, B., Fiji: an open-source platform for biological-image analysis. *Nature methods* **2012**, *9* (7), 676-682.
73. Daerr, A.; Mogne, A., Pendent\_drop: an imagej plugin to measure the surface tension from an image of a pendent drop. *Journal of Open Research Software* **2016**, *4* (1).
74. Papkov, D.; Zou, Y.; Andalib, M. N.; Goponenko, A.; Cheng, S. Z.; Dzenis, Y. A., Simultaneously strong and tough ultrafine continuous nanofibers. *ACS nano* **2013**, *7* (4), 3324-3331.
75. Raghavan, B.; Soto, H.; Lozano, K., Fabrication of Melt Spun Polypropylene Nanofibers by Forcespinning. *Journal of Engineered Fabrics & Fibers (JEFF)* **2013**, *8* (1).
76. Zhang, L.; Webster, T. J., Nanotechnology and nanomaterials: promises for improved tissue regeneration. *Nano today* **2009**, *4* (1), 66-80.
77. Dvir, T.; Timko, B. P.; Kohane, D. S.; Langer, R., Nanotechnological strategies for engineering complex tissues. *Nature nanotechnology* **2011**, *6* (1), 13.
78. Eyster, T. W.; Ma, P. X., Nanostructured Materials in Tissue Engineering. In *Nano/Micro-Structured Materials for Energy and Biomedical Applications*, Springer: 2018; pp 255-290.
79. Smith, I.; Liu, X.; Smith, L.; Ma, P., Nanostructured polymer scaffolds for tissue engineering and regenerative medicine. *Wiley Interdisciplinary Reviews: Nanomedicine and Nanobiotechnology* **2009**, *1* (2), 226-236.
80. Thomas, V.; Dean, D. R.; Jose, M. V.; Mathew, B.; Chowdhury, S.; Vohra, Y. K., Nanostructured biocomposite scaffolds based on collagen coelectrospun with nanohydroxyapatite. *Biomacromolecules* **2007**, *8* (2), 631-637.
81. Lee, S. J.; Nowicki, M.; Harris, B.; Zhang, L. G., Fabrication of a Highly Aligned Neural Scaffold via a Table Top Stereolithography 3D Printing and Electrospinning. *Tissue Eng Part A* **2017**, *23* (11-12), 491-502.
82. Genchi, G. G.; Ciofani, G.; Polini, A.; Liakos, I.; Iandolo, D.; Athanassiou, A.; Pisignano, D.; Mattoli, V.; Menciassi, A., PC12 neuron-like cell response to electrospun poly (3-hydroxybutyrate) substrates. *Journal of tissue engineering and regenerative medicine* **2015**, *9* (2), 151-161.
83. Tian, L.; Prabhakaran, M. P.; Hu, J.; Chen, M.; Besenbacher, F.; Ramakrishna, S., Synergistic effect of topography, surface chemistry and conductivity of the electrospun nanofibrous scaffold on cellular response of PC12 cells. *Colloids and Surfaces B: Biointerfaces* **2016**, *145*, 420-429.
84. Hu, J.; Tian, L.; Prabhakaran, M. P.; Ding, X.; Ramakrishna, S., Fabrication of nerve growth factor encapsulated aligned poly ( $\epsilon$ -caprolactone) nanofibers and their assessment as a potential neural tissue engineering scaffold. *Polymers* **2016**, *8* (2), 54.
85. Lim, S. M.; Jang, S. H.; Oh, S. H.; Yuk, S. H.; Im, G. I.; Lee, J. H., Dual-Growth-Factor-Releasing PCL Scaffolds for Chondrogenesis of Adipose-Tissue-Derived Mesenchymal Stem Cells. *Advanced Engineering Materials* **2010**, *12* (1-2).

86. Polini, A.; Pisignano, D.; Parodi, M.; Quarto, R.; Scaglione, S., Osteoinduction of human mesenchymal stem cells by bioactive composite scaffolds without supplemental osteogenic growth factors. *PloS one* **2011**, *6* (10), e26211.
87. Rubert, M.; Dehli, J.; Li, Y.-F.; Taskin, M. B.; Xu, R.; Besenbacher, F.; Chen, M., Electrospun PCL/PEO coaxial fibers for basic fibroblast growth factor delivery. *Journal of Materials Chemistry B* **2014**, *2* (48), 8538-8546.
88. Tıǧlı, R. S.; Kazaroǧlu, N. M.; Maviş, B.; Gümüşderelioǧlu, M., Cellular behavior on epidermal growth factor (EGF)-immobilized PCL/gelatin nanofibrous scaffolds. *Journal of Biomaterials Science, Polymer Edition* **2011**, *22* (1-3), 207-223.
89. Tabernero, A.; Granda, B.; Medina, A.; Sánchez-Abarca, L. I.; Lavado, E.; Medina, J. M., Albumin promotes neuronal survival by increasing the synthesis and release of glutamate. *Journal of neurochemistry* **2002**, *81* (4), 881-891.
90. Park, A.; Cima, L. G., In vitro cell response to differences in poly-L-lactide crystallinity. *Journal of Biomedical Materials Research Part A* **1996**, *31* (1), 17-30.
91. Washburn, N. R.; Yamada, K. M.; Simon, C. G.; Kennedy, S. B.; Amis, E. J., High-throughput investigation of osteoblast response to polymer crystallinity: influence of nanometer-scale roughness on proliferation. *Biomaterials* **2004**, *25* (7-8), 1215-1224.
92. Cui, H.; Sinko, P. J., The role of crystallinity on differential attachment/proliferation of osteoblasts and fibroblasts on poly (caprolactone-co-glycolide) polymeric surfaces. *Frontiers of Materials Science* **2012**, *6* (1), 47-59.
93. Areias, A. C.; Ribeiro, C.; Sencadas, V.; Garcia-Giralt, N.; Diez-Perez, A.; Gómez Ribelles, J. L.; Lanceros-Méndez, S., Influence of crystallinity and fiber orientation on hydrophobicity and biological response of poly(l-lactide) electrospun mats. *Soft Matter* **2012**, *8* (21), 5818.
94. Bognitzki, M.; Czado, W.; Frese, T.; Schaper, A.; Hellwig, M.; Steinhart, M.; Greiner, A.; Wendorff, J. H., Nanostructured fibers via electrospinning. *Advanced Materials* **2001**, *13* (1), 70-72.
95. Reneker, D. H.; Yarin, A. L.; Fong, H.; Koombhongse, S., Bending instability of electrically charged liquid jets of polymer solutions in electrospinning. *Journal of Applied physics* **2000**, *87* (9), 4531-4547.
96. Reneker, D. H.; Yarin, A. L., Electrospinning jets and polymer nanofibers. *Polymer* **2008**, *49* (10), 2387-2425.
97. Varga, B. V.; Hadinger, N.; Gocza, E.; Dulberg, V.; Demeter, K.; Madarasz, E.; Herberth, B., Generation of diverse neuronal subtypes in cloned populations of stem-like cells. *BMC Dev Biol* **2008**, *8*, 89.
98. Kornyei, Z.; Szlavik, V.; Szabo, B.; Gocza, E.; Czirok, A.; Madarasz, E., Humoral and contact interactions in astroglia/stem cell co-cultures in the course of glia-induced neurogenesis. *Glia* **2005**, *49* (3), 430-44.
99. Schindelin, J.; Rueden, C. T.; Hiner, M. C.; Eliceiri, K. W., The ImageJ ecosystem: an open platform for biomedical image analysis. *Molecular reproduction and development* **2015**, *82* (7-8), 518-529.
100. Longair, M. H.; Baker, D. A.; Armstrong, J. D., Simple Neurite Tracer: open source software for reconstruction, visualization and analysis of neuronal processes. *Bioinformatics* **2011**, *27* (17), 2453-2454.

101. Kuzelova Kostakova, E.; Meszaros, L.; Maskova, G.; Blazkova, L.; Turcsan, T.; Lukas, D., Crystallinity of Electrospun and Centrifugal Spun Polycaprolactone Fibers: A Comparative Study. *Journal of Nanomaterials* **2017**, 2017, 1-9.
102. Sehaqui, H.; Ezekiel Mushi, N.; Morimune, S.; Salajkova, M.; Nishino, T.; Berglund, L. A., Cellulose nanofiber orientation in nanopaper and nanocomposites by cold drawing. *ACS applied materials & interfaces* **2012**, 4 (2), 1043-1049.
103. Courtney, T.; Sacks, M. S.; Stankus, J.; Guan, J.; Wagner, W. R., Design and analysis of tissue engineering scaffolds that mimic soft tissue mechanical anisotropy. *Biomaterials* **2006**, 27 (19), 3631-8.
104. Carp, S., *Peripheral Nerve Injury An Anatomical and Physiological Approach for Physical Therapy Intervention*. FA Davis: 2015.
105. Masaeli, E.; Morshed, M.; Nasr-Esfahani, M. H.; Sadri, S.; Hilderink, J.; van Apeldoorn, A.; van Blitterswijk, C. A.; Moroni, L., Fabrication, characterization and cellular compatibility of poly(hydroxy alkanooate) composite nanofibrous scaffolds for nerve tissue engineering. *PLoS One* **2013**, 8 (2), e57157.
106. Liu, G.; Zhang, Q.; Jin, Y.; Gao, Z., Stress and strain analysis on the anastomosis site sutured with either epineurial or perineurial sutures after simulation of sciatic nerve injury. *Neural Regen Res* **2012**, 7 (29), 2299-304.
107. Francis, G. L., Albumin and mammalian cell culture: implications for biotechnology applications. *Cytotechnology* **2010**, 62 (1), 1-16.
108. Li, P.-S.; Lee, I.-L.; Yu, W.-L.; Sun, J.-S.; Jane, W.-N.; Shen, H.-H., A novel albumin-based tissue scaffold for autogenic tissue engineering applications. *Scientific reports* **2014**, 4, 5600.
109. Liu, Z.; Liu, J.; Wang, S.; Liu, S.; Zhao, Y., Neuronal uptake of serum albumin is associated with neuron damage during the development of epilepsy. *Exp Ther Med* **2016**, 12 (2), 695-701.
110. Bekard, I.; Dunstan, D. E., Electric field induced changes in protein conformation. *Soft Matter* **2014**, 10 (3), 431-437.
111. Okumura, T.; Yamada, K.; Yaegashi, T.; Takahashi, K.; Syuto, B.; Takaki, K., External AC Electric Field-Induced Conformational Change in Bovine Serum Albumin. *IEEE Transactions on Plasma Science* **2017**, 45 (3), 489-494.
112. Ji, W.; Sun, Y.; Yang, F.; van den Beucken, J. J.; Fan, M.; Chen, Z.; Jansen, J. A., Bioactive electrospun scaffolds delivering growth factors and genes for tissue engineering applications. *Pharm Res* **2011**, 28 (6), 1259-72.
113. Ji, W.; Yang, F.; van den Beucken, J. J.; Bian, Z.; Fan, M.; Chen, Z.; Jansen, J. A., Fibrous scaffolds loaded with protein prepared by blend or coaxial electrospinning. *Acta Biomater* **2010**, 6 (11), 4199-207.
114. Hu, X.; Park, S. H.; Gil, E. S.; Xia, X. X.; Weiss, A. S.; Kaplan, D. L., The influence of elasticity and surface roughness on myogenic and osteogenic-differentiation of cells on silk-elastin biomaterials. *Biomaterials* **2011**, 32 (34), 8979-89.
115. Breuls, R. G.; Jiya, T. U.; Smit, T. H., Scaffold stiffness influences cell behavior: opportunities for skeletal tissue engineering. *The open orthopaedics journal* **2008**, 2 (1).
116. Forte, G.; Pagliari, S.; Ebara, M.; Uto, K.; Tam, J. K.; Romanazzo, S.; Escobedo-Lucea, C.; Romano, E.; Di Nardo, P.; Traversa, E.; Aoyagi, T., Substrate stiffness modulates gene expression and phenotype in neonatal cardiomyocytes in vitro. *Tissue Eng Part A* **2012**, 18 (17-18), 1837-48.

117. Lin, H.-Y.; Chen, H.-H.; Chang, S.-H.; Ni, T.-S., Pectin-chitosan-PVA nanofibrous scaffold made by electrospinning and its potential use as a skin tissue scaffold. *Journal of Biomaterials Science, Polymer Edition* **2013**, *24* (4), 470-484.
118. Alborzi, S.; Lim, L. T.; Kakuda, Y., Electrospinning of Sodium Alginate-Pectin Ultrafine Fibers. *Journal of food science* **2010**, *75* (1), C100-C107.
119. Chen, W.; Shao, Y.; Li, X.; Zhao, G.; Fu, J., Nanotopographical surfaces for stem cell fate control: engineering mechanobiology from the bottom. *Nano Today* **2014**, *9* (6), 759-784.
120. Das, R. K.; Zouani, O. F.; Labrugère, C.; Oda, R.; Durrieu, M.-C., Influence of nanohelical shape and periodicity on stem cell fate. *ACS nano* **2013**, *7* (4), 3351-3361.
121. Lemischka, I. R.; Moore, K. A., Stem cells: interactive niches. *Nature* **2003**, *425* (6960), 778-779.
122. Spradling, A.; Drummond-Barbosa, D.; Kai, T., Stem cells find their niche. *Nature* **2001**, *414* (6859), 98.
123. Mikhaylova, Y.; Ionov, L.; Rappich, J.; Gensch, M.; Esser, N.; Minko, S.; Eichhorn, K.-J.; Stamm, M.; Hinrichs, K., In situ infrared ellipsometric study of stimuli-responsive mixed polyelectrolyte brushes. *Analytical chemistry* **2007**, *79* (20), 7676-7682.
124. Furchner, A.; Kroning, A.; Rauch, S.; Uhlmann, P.; Eichhorn, K.-J.; Hinrichs, K., Molecular Interactions and Hydration States of Ultrathin Functional Films at the Solid-Liquid Interface. *Analytical Chemistry* **2017**, *89* (6), 3240-3244.
125. Coleman, M.; Zarian, J., Fourier-transform infrared studies of polymer blends. II. Poly ( $\epsilon$ -caprolactone)-poly (vinyl chloride) system. *Journal of Polymer Science Part B: Polymer Physics* **1979**, *17* (5), 837-850.
126. Hinrichs, K.; Eichhorn, K.-J., *Ellipsometry of functional organic surfaces and films*. Springer: 2014; Vol. 52.
127. Higuchi, A.; Ling, Q.-D.; Chang, Y.; Hsu, S.-T.; Umezawa, A., Physical cues of biomaterials guide stem cell differentiation fate. *Chemical reviews* **2013**, *113* (5), 3297-3328.
128. Lee, S.-J.; Nowicki, M.; Harris, B.; Zhang, L. G., Fabrication of a highly aligned neural scaffold via a table top stereolithography 3D printing and electrospinning. *Tissue Engineering Part A* **2017**, *23* (11-12), 491-502.
129. Lv, Z. J.; Liu, Y.; Miao, H.; Leng, Z. Q.; Guo, J. H.; Liu, J., Effects of multiwalled carbon nanotubes on electrospun poly (lactide-co-glycolide)-based nanocomposite scaffolds on neural cells proliferation. *Journal of Biomedical Materials Research Part B: Applied Biomaterials* **2017**, *105* (5), 934-943.
130. Jiang, X.; Mi, R.; Hoke, A.; Chew, S. Y., Nanofibrous nerve conduit-enhanced peripheral nerve regeneration. *Journal of tissue engineering and regenerative medicine* **2014**, *8* (5), 377-385.
131. Masaeli, E.; Morshed, M.; Nasr-Esfahani, M. H.; Sadri, S.; Hilderink, J.; van Apeldoorn, A.; van Blitterswijk, C. A.; Moroni, L., Fabrication, characterization and cellular compatibility of poly (hydroxy alkanooate) composite nanofibrous scaffolds for nerve tissue engineering. *PloS one* **2013**, *8* (2), e57157.
132. Prabhakaran, M. P.; Ghasemi-Mobarakeh, L.; Jin, G.; Ramakrishna, S., Electrospun conducting polymer nanofibers and electrical stimulation of nerve stem cells. *Journal of bioscience and bioengineering* **2011**, *112* (5), 501-507.
133. Dalton, P. D.; Joergensen, N. T.; Groll, J.; Moeller, M., Patterned melt electrospun substrates for tissue engineering. *Biomedical materials* **2008**, *3* (3), 034109.

134. Jin, G.-Z.; Kim, M.; Shin, U. S.; Kim, H.-W., Neurite outgrowth of dorsal root ganglia neurons is enhanced on aligned nanofibrous biopolymer scaffold with carbon nanotube coating. *Neuroscience letters* **2011**, *501* (1), 10-14.
135. Xie, J.; Willerth, S. M.; Li, X.; Macewan, M. R.; Rader, A.; Sakiyama-Elbert, S. E.; Xia, Y., The differentiation of embryonic stem cells seeded on electrospun nanofibers into neural lineages. *Biomaterials* **2009**, *30* (3), 354-362.
136. Gu, F.; Yu, H.; Wang, P.; Yang, Z.; Tong, L., Light-emitting polymer single nanofibers via waveguiding excitation. *ACS nano* **2010**, *4* (9), 5332-5338.
137. Kose, R.; Mitani, I.; Kasai, W.; Kondo, T., "Nanocellulose" as a single nanofiber prepared from pellicle secreted by gluconacetobacter xylinus using aqueous counter collision. *Biomacromolecules* **2011**, *12* (3), 716-720.
138. Huang, Y.; Duan, Y.; Ding, Y.; Bu, N.; Pan, Y.; Lu, N.; Yin, Z., Versatile, kinetically controlled, high precision electrohydrodynamic writing of micro/nanofibers. *Scientific reports* **2014**, *4*, 5949.
139. Suryavanshi, A. P.; Hu, J.; Yu, M. F., Meniscus-Controlled Continuous Fabrication of Arrays and Rolls of Extremely Long Micro-and Nano-Fibers. *Advanced Materials* **2008**, *20* (4), 793-796.
140. Huang, S.; Zhao, C.; Pan, W.; Cui, Y.; Wu, H., Direct writing of half-meter long CNT based fiber for flexible electronics. *Nano letters* **2015**, *15* (3), 1609-1614.
141. Hu, J.; Yu, M.-F., Meniscus-confined three-dimensional electrodeposition for direct writing of wire bonds. *Science* **2010**, *329* (5989), 313-316.
142. Xing, X.; Wang, Y.; Li, B., Nanofiber drawing and nanodevice assembly in poly (trimethylene terephthalate). *Optics express* **2008**, *16* (14), 10815-10822.
143. Liao, S.; Bai, X.; Song, J.; Zhang, Q.; Ren, J.; Zhao, Y.; Wu, H., Draw-Spinning of Kilometer-Long and Highly Stretchable Polymer Submicrometer Fibers. *Advanced Science* **2017**, *4* (9).
144. Ondarcuhu, T.; Joachim, C., Drawing a single nanofibre over hundreds of microns. *EPL (Europhysics Letters)* **1998**, *42* (2), 215.
145. Zhang, L.; Kopperstad, P.; West, M.; Hedin, N.; Fong, H., Generation of polymer ultrafine fibers through solution (air-) blowing. *Journal of applied polymer science* **2009**, *114* (6), 3479-3486.
146. Trouton, F. T., On the coefficient of viscous traction and its relation to that of viscosity. *Proceedings of the Royal Society of London. Series A* **1906**, *77* (519), 426-440.
147. Fong, H.; Chun, I.; Reneker, D., Beaded nanofibers formed during electrospinning. *Polymer* **1999**, *40* (16), 4585-4592.
148. Zhou, X. J.; Park, J. Y.; Huang, S. M.; Liu, J.; McEuen, P. L., Band structure, phonon scattering, and the performance limit of single-walled carbon nanotube transistors. *Phys. Rev. Lett.* **2005**, *95* (14), -.
149. Taychatanapat, T.; Bolotin, K. I.; Kuemmeth, F.; Ralph, D. C., Imaging Electromigration during the Formation of Break Junctions. *Nano Lett.* **2007**, *7* (3), 652-656.
150. Zhou, W.; Zhan, S.; Ding, L.; Liu, J., General Rules for Selective Growth of Enriched Semiconducting Single Walled Carbon Nanotubes with Water Vapor as in Situ Etchant. *J. Am. Chem. Soc.* **2012**, *134* (34), 14019-14026.
151. Yang, X.; Liu, L.; Wu, M.; Wang, W.; Bai, X.; Wang, E., Wet-Chemistry-Assisted Nanotube-Substitution Reaction for High-Efficiency and Bulk-Quantity Synthesis of Boron- and

Nitrogen-Codoped Single-Walled Carbon Nanotubes. *J. Am. Chem. Soc.* **2011**, *133* (34), 13216-13219.

152. Hong, G.; Zhang, B.; Peng, B.; Zhang, J.; Choi, W. M.; Choi, J.-Y.; Kim, J. M.; Liu, Z., Direct Growth of Semiconducting Single-Walled Carbon Nanotube Array. *J. Am. Chem. Soc.* **2009**, *131* (41), 14642-14643.

153. Zhang, L.; Tu, X.; Welsher, K.; Wang, X.; Zheng, M.; Dai, H., Optical Characterizations and Electronic Devices of Nearly Pure (10,5) Single-Walled Carbon Nanotubes. *J. Am. Chem. Soc.* **2009**, *131* (7), 2454-2455.

154. Palacin, T.; Le Khanh, H.; Joussetme, B.; Jegou, P.; Filoramo, A.; Ehli, C.; Guldi, D. M.; Campidelli, S., Efficient Functionalization of Carbon Nanotubes with Porphyrin Dendrons via Click Chemistry. *J. Am. Chem. Soc.* **2009**, *131* (42), 15394-15402.

155. Zhang, L.; Zaric, S.; Tu, X.; Wang, X.; Zhao, W.; Dai, H., Assessment of chemically separated carbon nanotubes for nanoelectronics. *J. Am. Chem. Soc.* **2008**, *130* (8), 2686-2691.

156. So, H. M.; Kim, B.-K.; Park, D.-W.; Kim, B. S.; Kim, J.-J.; Kong, K.-J.; Chang, H.; Lee, J.-O., Selective suppression of conductance in metallic carbon nanotubes. *J. Am. Chem. Soc.* **2007**, *129* (16), 4866-4867.

157. Byon, H. R.; Choi, H. C., Network Single-Walled Carbon Nanotube-Field Effect Transistors (SWNT-FETs) with Increased Schottky Contact Area for Highly Sensitive Biosensor Applications. *J. Am. Chem. Soc.* **2006**, *128* (7), 2188-2189.

158. Chen, Z. H.; Appenzeller, J.; Knoch, J.; Lin, Y. M.; Avouris, P., The role of metal-nanotube contact in the performance of carbon nanotube field-effect transistors. *Nano Lett.* **2005**, *5* (7), 1497-1502.

159. Freitag, M.; Tsang, J. C.; Bol, A.; Yuan, D.; Liu, J.; Avouris, P., Imaging of the schottky barriers and charge depletion in carbon nanotube transistors. *Nano Lett.* **2007**, *7* (7), 2037-2042.

160. Rouhi, N.; Jain, D.; Burke, P. J., High-Performance Semiconducting Nanotube Inks: Progress and Prospects. *Acs Nano* **2011**, *5* (11), 8471-8487.

161. Caballero-Briones, F.; Artes, J. M.; Diez-Perez, I.; Gorostiza, P.; Sanz, F., Direct Observation of the Valence Band Edge by in Situ ECSTM-ECTS in p-Type Cu<sub>2</sub>O Layers Prepared by Copper Anodization. *J. Phys. Chem. C* **2009**, *113* (3), 1028-1036.

162. Hu, L.; Hecht, D. S.; Grüner, G., Carbon Nanotube Thin Films: Fabrication, Properties, and Applications. *Chem. Rev.* **2010**, *110* (10), 5790-5844.

163. Yuhas, B. D.; Yang, P., Nanowire-Based All-Oxide Solar Cells. *J. Am. Chem. Soc.* **2009**, *131* (10), 3756-3761.

164. McShane, C. M.; Choi, K.-S., Photocurrent Enhancement of n-Type Cu<sub>2</sub>O Electrodes Achieved by Controlling Dendritic Branching Growth. *J. Am. Chem. Soc.* **2009**, *131* (7), 2561-2569.

165. Deng, S.; Tjoa, V.; Fan, H. M.; Tan, H. R.; Sayle, D. C.; Olivo, M.; Mhaisalkar, S.; Wei, J.; Sow, C. H., Reduced Graphene Oxide Conjugated Cu<sub>2</sub>O Nanowire Mesocrystals for High-Performance NO<sub>2</sub> Gas Sensor. *J. Am. Chem. Soc.* **2012**, *134* (10), 4905-4917.

166. Yang, F.; Choi, Y.; Liu, P.; Stacchiola, D.; Hrbek, J.; Rodriguez, J. A., Identification of 5-7 Defects in a Copper Oxide Surface. *J. Am. Chem. Soc.* **2011**, *133* (30), 11474-11477.

167. Li, C. W.; Kanan, M. W., CO<sub>2</sub> Reduction at Low Overpotential on Cu Electrodes Resulting from the Reduction of Thick Cu<sub>2</sub>O Films. *J. Am. Chem. Soc.* **2012**, *134* (17), 7231-7234.

168. Huang, W.-C.; Lyu, L.-M.; Yang, Y.-C.; Huang, M. H., Synthesis of Cu<sub>2</sub>O Nanocrystals from Cubic to Rhombic Dodecahedral Structures and Their Comparative Photocatalytic Activity. *J. Am. Chem. Soc.* **2012**, *134* (2), 1261-1267.

169. Kocabas, C.; Pimparkar, N.; Yesilyurt, O.; Kang, S. J.; Alam, M. A.; Rogers, J. A., Experimental and theoretical studies of transport through large scale, partially aligned arrays of single-walled carbon nanotubes in thin film type transistors. *Nano Lett.* **2007**, *7*, 1195-1202.
170. Yan, X.; Cui, X.; Li, L.-s., Synthesis of Large, Stable Colloidal Graphene Quantum Dots with Tunable Size. *J. Am. Chem. Soc.* **2010**, *132* (17), 5944-5945.
171. Heller, I.; Chatoor, S.; Männik, J.; Zevenbergen, M. A. G.; Dekker, C.; Lemay, S. G., Influence of Electrolyte Composition on Liquid-Gated Carbon Nanotube and Graphene Transistors. *J. Am. Chem. Soc.* **2010**, *132* (48), 17149-17156.
172. Lay Marcus, D.; Vichchulada, P.; Asheghali, D. 2012.
173. Yang, M. H.; Teo, K. B. K.; Milne, W. I.; Hasko, D. G., Carbon nanotube Schottky diode and directionally dependent field-effect transistor using asymmetrical contacts. *Appl. Phys. Lett.* **2005**, *87* (25), 3.
174. Lu, C. G.; An, L.; Fu, Q. A.; Liu, J.; Zhang, H.; Murduck, J., Schottky diodes from asymmetric metal-nanotube contacts. *Appl. Phys. Lett.* **2006**, *88* (13), 3.
175. Fuhrer, M. S.; Nygard, J.; Shih, L.; Forero, M.; Yoon, Y. G.; Mazzoni, M. S. C.; Choi, H. J.; Ihm, J.; Louie, S. G.; Zettl, A.; McEuen, P. L., Crossed nanotube junctions. *Science* **2000**, *288* (5465), 494-497.
176. Nirmalraj, P. N.; Lyons, P. E.; De, S.; Coleman, J. N.; Boland, J. J., Electrical Connectivity in Single-Walled Carbon Nanotube Networks. *Nano Lett.* **2009**, *9* (11), 3890-3895.
177. Bhatt, N. P.; Vichchulada, P.; Lay, M. D., Bulk Purification and Deposition Methods for Selective Enrichment in High Aspect Ratio Single-Walled Carbon Nanotubes. *J. Am. Chem. Soc.* **2012**, *134* (22), 9352-9361.
178. Zhang, Q.; Vichchulada, P.; Lay, M. D., Length, Bundle, and Density Gradients in Spin Cast Single-Walled Carbon Nanotube Networks. *J. Phys. Chem. C* **2010**, *114* (39), 16292-16297.
179. Vichchulada, P.; Zhang, Q.; Duncan, A.; Lay, M. D., Macroscopic Electrical Properties of Ordered Single-Walled Carbon Nanotube Networks. *ACS Appl. Mater. Interfaces* **2010**, *2* (2), 467-473.
180. Sangwan, V. K.; Ortiz, R. P.; Alaboson, J. M. P.; Emery, J. D.; Bedzyk, M. J.; Lauhon, L. J.; Marks, T. J.; Hersam, M. C., Fundamental Performance Limits of Carbon Nanotube Thin-Film Transistors Achieved Using Hybrid Molecular Dielectrics. *Acs Nano* **2012**, *6* (8), 7480-7488.
181. Zhang, Q.; Vichchulada, P.; Cauble, M. A.; Lay, M. D., Percolation in networks of aligned SWNTs formed with laminar flow deposition. *J. Mater. Sci.* **2009**, *44* (5), 1206-1211.
182. Li, E. Y.; Marzari, N., Improving the Electrical Conductivity of Carbon Nanotube Networks: A First-Principles Study. *Acs Nano* **2011**, *5* (12), 9726-9736.
183. Zhang, Y.; Franklin, N. W.; Chen, R. J.; Dai, H. J., Metal coating on suspended carbon nanotubes and its implication to metal-tube interaction. *Chem. Phys. Lett.* **2000**, *331* (1), 35-41.
184. Rodriguez-Manzo, J. A.; Banhart, F.; Terrones, M.; Terrones, H.; Grobert, N.; Ajayan, P. M.; Sumpter, B. G.; Meunier, V.; Wang, M.; Bando, Y.; Golberg, D., Heterojunctions between metals and carbon nanotubes as ultimate nanocontacts. *Proc. Natl. Acad. Sci. USA* **2009**, *106* (12), 4591-4595.
185. Zhang, Y.; Ichihashi, T.; Landree, E.; Nihey, F.; Iijima, S., Heterostructures of Single-Walled Carbon Nanotubes and Carbide Nanorods. *Science* **1999**, *285* (5434), 1719-1722.
186. Asaka, K.; Karita, M.; Saito, Y., Modification of interface structure and contact resistance between a carbon nanotube and a gold electrode by local melting. *Appl. Surf. Sci.* **2011**, *257* (7), 2850-2853.

187. Madsen, D. N.; Mølhave, K.; Mateiu, R.; Rasmussen, A. M.; Brorson, M.; Jacobsen, C. J. H.; Bøggild, P., Soldering of Nanotubes onto Microelectrodes. *Nano Lett.* **2002**, *3* (1), 47-49.
188. Zhang, Q.; Vichchulada, P.; Shivareddy, S. B.; Lay, M. D., Reducing Electrical Resistance in Single-Walled Carbon Nanotube Networks: Effect of the Location of Metal Contacts and Low-Temperature Annealing *J. Mat. Sci.* **2012**, *47*, 6812-6822.
189. Chow, B. Y.; Mosley, D. W.; Jacobson, J. M., Perfecting imperfect "monolayers": Removal of siloxane multilayers by CO<sub>2</sub> snow treatment. *Langmuir* **2005**, *21* (11), 4782-4785.
190. Vichchulada, P.; Cauble, M. A.; Abdi, E. A.; Obi, E. I.; Zhang, Q.; Lay, M. D., Sonication Power for Length Control of Single-Walled Carbon Nanotubes in Aqueous Suspensions Used for 2-Dimensional Network Formation. *J. Phys. Chem. C* **2010**, *114* (29), 12490-12495.
191. Horcas, I.; Fernandez, R.; Gomez-Rodriguez, J. M.; Colchero, J.; Gomez-Herrero, J.; Baro, A. M., WSXM: A software for scanning probe microscopy and a tool for nanotechnology. *Rev. Sci. Instrum.* **2007**, *78* (1).
192. Savio, A. K. P. D.; Starikov, D.; Bensaoula, A.; Pillai, R.; de la Torre García, L. L.; Robles Hernández, F. C., Tunable TiO<sub>2</sub> (anatase and rutile) materials manufactured by mechanical means. *Ceram. Int.* **2012**, *38* (5), 3529-3535.
193. Lee, M.-K.; Yen, C.-F., Low Leakage and High-k Liquid Phase Deposited TiO<sub>2</sub> and SiO<sub>2</sub>/TiO<sub>2</sub> Films on (NH<sub>4</sub>)<sub>2</sub>S-Treated GaAs. *Electrochem. Solid St.* **2010**, *13* (10), G87-G90.
194. Basame, S. B.; White, H. S., Scanning electrochemical microscopy of metal/metal oxide electrodes. Analysis of spatially localized electron-transfer reactions during oxide growth. *Anal. Chem.* **1999**, *71* (15), 3166-3170.
195. Boxley, C. J.; White, H. S.; Gardner, C. E.; Macpherson, J. V., Nanoscale imaging of the electronic conductivity of the native oxide film on titanium using conducting atomic force microscopy. *J. Phys. Chem. B* **2003**, *107* (36), 9677-9680.
196. Rao, C. N. R.; Subba Rao, G. V., Electrical conduction in metal oxides. *Phys. Status Solidi* **1970**, *1* (4), 597-652.
197. Emery, S. B.; Hubble, J. L.; Roy, D., Voltammetric and amperometric analyses of electrochemical nucleation: electrodeposition of copper on nickel and tantalum. *J. Electroanal. Chem.* **2004**, *568* (1-2), 121-133.
198. Oskam, G.; Searson, P. C., Electrochemical nucleation and growth of gold on silicon. *Surf. Sci.* **2000**, *446* (1-2), 103-111.
199. Casillas, N.; Charlebois, S.; Smyrl, W. H.; White, H. S., Pitting Corrosion of Titanium. *J. Electrochem. Soc.* **1994**, *141* (3), 636-642.
200. Scharifker, B.; Hills, G., Theoretical and experimental studies of multiple nucleation. *Electrochim. Acta* **1983**, *28* (7), 879-889.
201. Liu, R.; Oba, F.; Bohannan, E. W.; Ernst, F.; Switzer, J. A., Shape Control in Epitaxial Electrodeposition: Cu<sub>2</sub>O Nanocubes on InP(001). *Chem. Mater.* **2003**, *15* (26), 4882-4885.
202. Zhao, L.; Dong, W.; Zheng, F.; Fang, L.; Shen, M., Interrupted growth and photoelectrochemistry of Cu<sub>2</sub>O and Cu particles on TiO<sub>2</sub>. *Electrochim. Acta* **2012**, *80*, 354-361.
203. Wu, S.; Yin, Z.; He, Q.; Lu, G.; Zhou, X.; Zhang, H., Electrochemical deposition of Cl-doped n-type Cu<sub>2</sub>O on reduced graphene oxide electrodes. *J. Mater. Chem.* **2011**, *21* (10), 3467-3470.
204. Basu, M.; Sinha, A. K.; Pradhan, M.; Sarkar, S.; Negishi, Y.; Pal, T., Fabrication and Functionalization of CuO for Tuning Superhydrophobic Thin Film and Cotton Wool. *J. Phys. Chem. C* **2011**, *115* (43), 20953-20963.

205. Banus, M. D.; Reed, T. B.; Strauss, A. J., Electrical and Magnetic Properties of TiO and VO. *Phys. Rev. B* **1972**, *5* (8), 2775-2784.
206. Vandenberg, E. T.; Bertilsson, L.; Liedberg, B.; Uvdal, K.; Erlandsson, R.; Elwing, H.; Lundstrom, I., Structure of 3-aminopropyl triethoxy silane on silicon oxide. *J. Colloid Interface Sci.* **1991**, *147* (1), 103-118.
207. Laitinen, H. A.; Kolthoff, I. M., A Study of Diffusion Processes by Electrolysis with Microelectrodes. *J. Am. Chem. Soc.* **1939**, *61* (12), 3344-3349.
208. Bard, A. J.; Faulkner, L. R., *Electrochemical Methods, Fundamentals and Applications*. 2nd ed.; John Wiley & Sons: New York, 2001.
209. Fan, Y. W.; Goldsmith, B. R.; Collins, P. G., Identifying and counting point defects in carbon nanotubes. *Nat. Mater.* **2005**, *4* (12), 906-911.
210. Walter, E. C.; Murray, B. J.; Favier, F.; Kaltenpoth, G.; Grunze, M.; Penner, R. M., Noble and coinage metal nanowires by electrochemical step edge decoration. *J. Phys. Chem. B* **2002**, *106* (44), 11407-11411.
211. Dudin, P. V.; Snowden, M. E.; Macpherson, J. V.; Unwin, P. R., Electrochemistry at Nanoscale Electrodes: Individual Single-Walled Carbon Nanotubes (SWNTs) and SWNT-Templated Metal Nanowires. *Acs Nano* **2011**, *5* (12), 10017-10025.
212. Day, T. M.; Wilson, N. R.; Macpherson, J. V., Electrochemical and conductivity measurements of single-wall carbon nanotube network electrodes. *J. Am. Chem. Soc.* **2004**, *126* (51), 16724-16725.
213. Yang, Z.; Sun, Y.; Alemany, L. B.; Narayanan, T. N.; Billups, W. E., Birch Reduction of Graphite. Edge and Interior Functionalization by Hydrogen. *J. Am. Chem. Soc.* **2012**, *134* (45), 18689-18694.
214. Schwab, M. G.; Narita, A.; Hernandez, Y.; Balandina, T.; Mali, K. S.; De Feyter, S.; Feng, X.; Muellen, K., Structurally Defined Graphene Nanoribbons with High Lateral Extension. *J. Am. Chem. Soc.* **2012**, *134* (44), 18169-18172.
215. Balog, R.; Jorgensen, B.; Wells, J.; Laegsgaard, E.; Hofmann, P.; Besenbacher, F.; Hornekaer, L., Atomic Hydrogen Adsorbate Structures on Graphene. *J. Am. Chem. Soc.* **2009**, *131* (25), 8744-+.
216. Bockrath, M.; Liang, W. J.; Bozovic, D.; Hafner, J. H.; Lieber, C. M.; Tinkham, M.; Park, H. K., Resonant electron scattering by defects in single-walled carbon nanotubes. *Science* **2001**, *291* (5502), 283-285.